Berm and Dune Erosion during a Storm

by

Mitchell Buck, Nobuhisa Kobayashi,
Andres Payo and Bradley Johnson

RESEARCH REPORT NO. CACR-07-03
September, 2007

Center for Applied Coastal Research
Ocean Engineering Laboratory
University of Delaware
Newark, DE 19716

ACKNOWLEDGEMENTS

This study was supported by the U.S. Army Corps of Engineers under contract number W912BU-07-C-0013. The authors would like to thank Marcel van Gent for providing the dune erosion data used in this study. The third author was supported by the Spanish Postdoctoral Scholarship MEC/FULBRIGHT.

TABLE OF CONTENTS

LIST OF FIGURES . . . . . **vi**
LIST OF TABLES . . . . . **xii**
ABSTRACT . . . . . **xvii**

Chapter

1 INTRODUCTION **1**
2 SMALL SCALE EXPERIMENTAL METHODS **4**

2.1 Dune Erosion Experiments 4
2.2 Beach Profile Construction 5
2.3 Experimental Setup 6
2.4 Sediment Characteristics 8
2.5 Profile Measurements 10
2.6 Wave Gauges 12
2.7 Acoustic-Doppler Velocimeters 13
2.8 Fiber Optic Sediment Monitors (FOBS-7) 15
2.9 Data Collection 18
2.10 Incident and Reflected Waves 18

3 SMALL SCALE DATA ANALYSIS **21**

3.1 Profile Evolution 21
3.2 Free Surface 33
3.3 Velocity 38
3.4 Concentration 40

4 NUMERICAL MODEL DEVELOPMENT **43**

4.1 Combined Wave and Current Model 43
4.2 Sediment Transport Model 49

5 NUMERICAL MODEL COMPARISON WITH SMALL-SCALE EXPERIMENTS 54
6 NUMERICAL MODEL COMPARISON WITH LARGE-SCALE EXPERIMENTS 61
7 EFFECT OF INCIDENT WAVE ANGLE 67
8 CONCLUSIONS 79
REFERENCES 82

Appendix

A EXPERIMENT H 85
B EXPERIMENT L 118
C LARGE SCALE TESTS 151

LIST OF FIGURES

2.1 Cross-shore profile with wave gauge, ADV and FOBS setup. 5

2.2 Initial berm and dune geometries. 7

2.3 Sand grain size distribution. 10

2.4 Measured transect lines before smoothing and averaging. 11

2.5 Calibration curve for wave gauge 1 (left) and wave gauge 8 (right). 13

2.6 Long-shore wave gauge, ADV and FOBS Setup. 14

2.7 FOBS-7 setup and position relative to the local bed. 16

2.8 FOBS-7 calibration curve for sensor 1 (top) and sensor 2 (bottom). 17

2.9 Incident and reflected wave spectra for experiment H (top) and L (bottom). 20

3.1 Measured profile change from time t = 0-2 hr for tests HA and HB (top) and tests LA and LB (bottom). 22

3.2 Measured profile change from t = 2-3.67 hr for tests HC and HD (top) and LC and LD (bottom). 24

3.3 Measured profile change of berm and dune region recorded at times t = 0-3.67 hr for experiment H (top) and L (bottom). 25

3.4 Measured dune breach geometry for test HD from the front (top) and back (bottom). 27

3.5 Measured dune breach geometry for test LD from the front (top) and back (bottom). 28

3.6 Characteristics of the coarse sand from the swash zone. 29

3.7 Measured profile change from $t = 3.67$-6.11 hr for tests HE and HF (top) and tests LE and LF (bottom). 30

3.8 Measured profile change for berm and dune region recorded at times $t = 3.67$-6.11 hr for experiment H (top) and L (bottom). 31

3.9 Eroded Area, A_e (cm^2), plotted for each test of experiment H and L. 32

3.10 Time series for measured mean velocity, $\bar{U}$, and standard deviation of velocity, σ_U for experiment H (top) and L (bottom). 39

3.11 Time series for measured mean concentration, $\bar{C}$, standard deviation of concentration, σ_C, and correlation coefficient, γ_{UC}, for experiment H (top) and L (bottom). 42

5.1 **Experiment H:** measured vs. computed profiles at the end of 6 tests. 56

5.2 **Experiment L:** measured vs. computed profiles at the end of 6 tests. 57

5.3 Measured vs. computed eroded area, A_e, for experiments H (top) and L (bottom) 58

5.4 Cross-shore variations of measured vs. computed $(S + \bar{\eta})$, σ_η, $\bar{U}$ and σ_U for test HD (left) and test LD (right) 60

6.1 Initial profile for large-scale scale experiments T01, T02 and T03. . 62

6.2 Measured vs. computed profiles at the end of tests T01 (top), T02 (middle) and T03 (bottom). 63

6.3 Cross-shore variations of $\bar{\eta}$, σ_η, $\bar{U}$ and σ_U for tests T01, T02 and T03 on the initial profile z_b. 65

6.4 Cross-shore variations of $\bar{\eta}$, σ_η, $\bar{U}$ and σ_U at the end of T01, T02 and T03 66

7.1 Computed A_e/A_0 for $\theta = 10°$, $30°$ and $45°$ for experiments H and L. 68

7.2 Computed A_e/A_0 for three large-scale tests. 70

7.3 Cross-shore variations of $(S+\bar{\eta})$, σ_η, $\bar{U}$, σ_U, $\bar{V}$, $P_b = P_s$ and V_s for $\theta = 0^\circ$ and $\theta = 30^\circ$ for tests HD (left) and LD (right) 73

7.4 Cross-shore variations of $(S+\bar{\eta})$, σ_η, $\bar{U}$, σ_U, $\bar{V}$, $P_b = P_s$ and V_s for $\theta = 0^\circ$ and $\theta = 30^\circ$ for tests T01E (left) and T02E (right) 74

7.5 Cross-shore variations of $(S+\bar{\eta})$, σ_η, $\bar{U}$, σ_U, $\bar{V}$, $P_b = P_s$ and V_s for $\theta = 0^\circ$ and $\theta = 30^\circ$ for test T03E 75

7.6 Cross-shore variations of q_{bx}, q_{sx}, q_{by} and q_{sy} for $\theta = 0^\circ$ and $\theta = 30^\circ$ for tests HD (left) and LD (right). 76

7.7 Cross-shore variations of q_{bx}, q_{sx}, q_{by} and q_{sy} for $\theta = 0^\circ$ and $\theta = 30^\circ$ for tests T01E and T02E. 77

7.8 Cross-shore variations of q_{bx}, q_{sx}, q_{by} and q_{sy} for $\theta = 0^\circ$ and $\theta = 30^\circ$ for test T03E. 78

A.1 Cross-shore variations of measured vs. computed $(S+\bar{\eta})$, σ_η, $\bar{U}$ and σ_U for tests HA (left) and HB (right) 109

A.2 Cross-shore variations of measured vs. computed $(S+\bar{\eta})$, σ_η, $\bar{U}$ and σ_U for tests HC (left) and HD (right) 110

A.3 Cross-shore variations of measured vs. computed $(S+\bar{\eta})$, σ_η, $\bar{U}$ and σ_U for tests HE (left) and HF (right) 111

A.4 Cross-shore variations of $(S+\bar{\eta})$, σ_η, $\bar{U}$, σ_U, $\bar{V}$, $P_b = P_s$ and V_s for $\theta = 0^\circ$ and $\theta = 30^\circ$ for tests HA (left) and HB (right) 112

A.5 Cross-shore variations of $(S+\bar{\eta})$, σ_η, $\bar{U}$, σ_U, $\bar{V}$, $P_b = P_s$ and V_s for $\theta = 0^\circ$ and $\theta = 30^\circ$ for tests HC (left) and HD (right) 113

A.6 Cross-shore variations of $(S+\bar{\eta})$, σ_η, $\bar{U}$, σ_U, $\bar{V}$, $P_b = P_s$ and V_s for $\theta = 0^\circ$ and $\theta = 30^\circ$ for tests HE (left) and HF (right) 114

A.7 Cross-shore variations of q_{bx}, q_{sx}, q_{by} and q_{sy} for $\theta = 0^\circ$ and $\theta = 30^\circ$ in tests HA (left) and HB (right). 115

A.8 Cross-shore variations of q_{bx}, q_{sx}, q_{by} and q_{sy} for $\theta = 0°$ and $\theta = 30°$ in tests HC (left) and HD (right). 116

A.9 Cross-shore variations of q_{bx}, q_{sx}, q_{by} and q_{sy} for $\theta = 0°$ and $\theta = 30°$ in tests HE (left) and HF (right). 117

B.1 Cross-shore variations of measured vs. computed $(S + \bar{\eta})$, σ_η, $\bar{U}$ and σ_U for tests LA (left) and LB (right) 142

B.2 Cross-shore variations of measured vs. computed $(S + \bar{\eta})$, σ_η, $\bar{U}$ and σ_U for tests LC (left) and LD (right) 143

B.3 Cross-shore variations of measured vs. computed $(S + \bar{\eta})$, σ_η, $\bar{U}$ and σ_U for tests LE (left) and LF (right) 144

B.4 Cross-shore variations of $(S + \bar{\eta})$, σ_η, $\bar{U}$, σ_U, $\bar{V}$, $P_b = P_s$ and V_s for $\theta = 0°$ and $\theta = 30°$ for tests LA (left) and LB (right) 145

B.5 Cross-shore variations of $(S + \bar{\eta})$, σ_η, $\bar{U}$, σ_U, $\bar{V}$, $P_b = P_s$ and V_s for $\theta = 0°$ and $\theta = 30°$ for tests LC (left) and LD (right) 146

B.6 Cross-shore variations of $(S + \bar{\eta})$, σ_η, $\bar{U}$, σ_U, $\bar{V}$, $P_b = P_s$ and V_s for $\theta = 0°$ and $\theta = 30°$ for tests LE (left) and LF (right) 147

B.7 Cross-shore variations of q_{bx}, q_{sx}, q_{by} and q_{sy} for $\theta = 0°$ and $\theta = 30°$ in tests LA (left) and LB (right). 148

B.8 Cross-shore variations of q_{bx}, q_{sx}, q_{by} and q_{sy} for $\theta = 0°$ and $\theta = 30°$ in tests LC (left) and LD (right). 149

B.9 Cross-shore variations of q_{bx}, q_{sx}, q_{by} and q_{sy} for $\theta = 0°$ and $\theta = 30°$ in tests LE (left) and LF (right). 150

C.1 Cross-shore variations of computed $(S + \bar{\eta})$, σ_η, $\bar{U}$ and σ_U for T01I, T02I and T03I ($t = 0$ s). 152

C.2 Cross-shore variations of computed $(S + \bar{\eta})$, σ_η, $\bar{U}$ and σ_U for T01A, T02A and T03A (left) and T01B, T02B and T03B (right). 153

C.3 Cross-shore variations of computed $(S + \bar{\eta})$, σ_η, $\bar{U}$ and σ_U for T01C, T02C and T03C (left) and T01D, T02D and T03D (right). 154

C.4 Cross-shore variations of computed $(S + \bar{\eta})$, σ_η, $\bar{U}$ and σ_U for T01E, T02E and T03E. 155

C.5 Cross-shore variations of $(S + \bar{\eta})$, σ_η, $\bar{U}$, σ_U, $\bar{V}$, $P_b = P_s$ and V_s for θ = 0° and $\theta = 30°$ for tests T01A (left) and T01B (right) 156

C.6 Cross-shore variations of $(S + \bar{\eta})$, σ_η, $\bar{U}$, σ_U, $\bar{V}$, $P_b = P_s$ and V_s for θ = 0° and $\theta = 30°$ for tests T01C (left) and T01D (right) 157

C.7 Cross-shore variations of $(S + \bar{\eta})$, σ_η, $\bar{U}$, σ_U, $\bar{V}$, $P_b = P_s$ and V_s for θ = 0° and $\theta = 30°$ for test T01E 158

C.8 Cross-shore variations of q_{bx}, q_{sx}, q_{by} and q_{sy} for $\theta = 0°$ and $\theta = 30°$ in tests T01A (left) and T01B (right). 159

C.9 Cross-shore variations of q_{bx}, q_{sx}, q_{by} and q_{sy} for $\theta = 0°$ and $\theta = 30°$ in tests T01C (left) and T01D (right). 160

C.10 161

C.11 Cross-shore variations of q_{bx}, q_{sx}, q_{by} and q_{sy} for $\theta = 0°$ and $\theta = 30°$ in test T01E. 161

C.12 Cross-shore variations of $(S + \bar{\eta})$, σ_η, $\bar{U}$, σ_U, $\bar{V}$, $P_b = P_s$ and V_s for θ = 0° and $\theta = 30°$ for tests T02A (left) and T02B (right) 162

C.13 Cross-shore variations of $(S + \bar{\eta})$, σ_η, $\bar{U}$, σ_U, $\bar{V}$, $P_b = P_s$ and V_s for θ = 0° and $\theta = 30°$ for tests T02C (left) and T02D (right) 163

C.14 Cross-shore variations of $(S + \bar{\eta})$, σ_η, $\bar{U}$, σ_U, $\bar{V}$, $P_b = P_s$ and V_s for θ = 0° and $\theta = 30°$ for test T02E 164

C.15 Cross-shore variations of q_{bx}, q_{sx}, q_{by} and q_{sy} for $\theta = 0°$ and $\theta = 30°$ in tests T02A (left) and T02B (right). 165

C.16 Cross-shore variations of q_{bx}, q_{sx}, q_{by} and q_{sy} for $\theta = 0°$ and $\theta = 30°$ in tests T02C (left) and T02D (right). 166

C.17 Cross-shore variations of q_{bx}, q_{sx}, q_{by} and q_{sy} for $\theta = 0°$ and $\theta = 30°$ in tests T02E. 167

C.18 Cross-shore variations of $(S + \bar{\eta})$, σ_η, $\bar{U}$, σ_U, $\bar{V}$, $P_b = P_s$ and V_s for $\theta = 0^\circ$ and $\theta = 30^\circ$ for tests T03A (left) and T03B (right) 168

C.19 Cross-shore variations of $(S + \bar{\eta})$, σ_η, $\bar{U}$, σ_U, $\bar{V}$, $P_b = P_s$ and V_s for $\theta = 0^\circ$ and $\theta = 30^\circ$ for tests T03C (left) and T03D (right) 169

C.20 Cross-shore variations of $(S + \bar{\eta})$, σ_η, $\bar{U}$, σ_U, $\bar{V}$, $P_b = P_s$ and V_s for $\theta = 0^\circ$ and $\theta = 30^\circ$ for test T03E 170

C.21 Cross-shore variations of q_{bx}, q_{sx}, q_{by} and q_{sy} for $\theta = 0^\circ$ and $\theta = 30^\circ$ in tests T03A (left) and T03B (right). 171

C.22 Cross-shore variations of q_{bx}, q_{sx}, q_{by} and q_{sy} for $\theta = 0^\circ$ and $\theta = 30^\circ$ in tests T03C (left) and T03D (right). 172

C.23 Cross-shore variations of q_{bx}, q_{sx}, q_{by} and q_{sy} for $\theta = 0^\circ$ and $\theta = 30^\circ$ in test T03E. 173

LIST OF TABLES

2.1 Experimental Sequence. 8

2.2 Summary of sieve test. 9

2.3 Wave gauge placement. 12

2.4 Average incident and reflected spectral and time series parameters across each test within each experiment. 19

3.1 **Experiment H:** incident spectral and time series parameters. . . 34

3.2 **Experiment H:** incident spectral and time series parameters (continued). 35

3.3 **Experiment L:** incident spectral and time series parameters. . . 36

3.4 **Experiment L:** incident spectral and time series parameters (continued). 37

5.1 Incident and reflected spectral and time series parameters for each test. 55

5.2 Measured vs. computed eroded area, A_e, for the small scale experiments 57

6.1 **Large Scale Tests:** Wave conditions at $x = 0$ m. 62

6.2 Eroded area, A_e, for large-scale tests where the letters I, A, B, C, D and E are used to indicate time t later. 64

7.1 Computed A_e/A_0 for small-scale experiments H and L. 69

7.2 Computed A_e/A_0 for the three large-scale tests. 71

A.1 Free surface measurements for bursts HA1 to HA8 where NR = not reliable in this and subsequent tables. 86

A.2 Free surface measurements for burst HA9 and the average over all the bursts. 87

A.3 Free surface measurements for bursts HB1 to HB8. 88

A.4 Free surface measurements for burst HB9 and the average over all the bursts. 89

A.5 Free surface measurements for bursts HC1 to HC8. 90

A.6 Free surface measurements for burst HC9 and the average over all the bursts. 91

A.7 Free surface measurements for bursts HD1 to HD6, including the average over all the bursts. 92

A.8 Free surface measurements for bursts HE1 to HE8. 93

A.9 Free surface measurements for bursts HE9 to HE11, including the average over all the bursts. 94

A.10 Free surface measurements for bursts HF1 to HF8. 95

A.11 Free surface measurements for bursts HF9 to HF11, including the average over all the bursts. 96

A.12 Velocity measurements for bursts HA1 to HA9, including the average over all the bursts. 97

A.13 Velocity measurements for bursts HB1 to HB9, including the average over all the bursts. 98

A.14 Velocity measurements for bursts HC1 to HC9, including the average over all the bursts. 99

A.15 Velocity measurements for bursts HD1 to HD6, including the average over all the bursts. 100

A.16 Velocity measurements for bursts HE1 to HE11, including the average over all the bursts. 101

A.17 Velocity measurements for bursts HF1 to HF11, including the average over all the bursts. 102

A.18 Concentration measurements for bursts HA1 to HA9, including the average over all the bursts. 103

A.19 Concentration measurements for bursts HB1 to HB9, including the average over all the bursts. 104

A.20 Concentration measurements for bursts HC1 to HC9, including the average over all the bursts. 105

A.21 Concentration measurements for bursts HD1 to HD6, including the average over all the bursts. 106

A.22 Concentration measurements for bursts HE1 to HE11, including the average over all the bursts. 107

A.23 Concentration measurements for bursts HF1 to HF11, including the average over all the bursts. 108

B.1 Free surface measurements for bursts LA1 to LA8. 119

B.2 Free surface measurements for burst LA9 and the average over all the bursts. 120

B.3 Free surface measurements for bursts LB1 to LB8. 121

B.4 Free surface measurements for burst LB9 and the average over all the bursts. 122

B.5 Free surface measurements for bursts LC1 to LC8. 123

B.6 Free surface measurements for burst LC9 and the average over all the bursts. 124

B.7 Free surface measurements for bursts LD1 to LD6, including the average over all the bursts. 125

B.8 Free surface measurements for bursts LE1 to LE8. 126

B.9 Free surface measurements for bursts LE9 to LE11, including the average over all the bursts. 127

B.10 Free surface measurements for bursts LF1 to LF8. 128

B.11 Free surface measurements for bursts LF9 to LF11, including the average over all the bursts. 129

B.12 Velocity measurements for bursts LA1 to LA9, including the average over all the bursts. 130

B.13 Velocity measurements for bursts LB1 to LB9, including the average over all the bursts. 131

B.14 Velocity measurements for bursts LC1 to LC9, including the average over all the bursts. 132

B.15 Velocity measurements for bursts LD1 to LD6, including the average over all the bursts. 133

B.16 Velocity measurements for bursts LE1 to LE11, including the average over all the bursts. 134

B.17 Velocity measurements for bursts LF1 to LF11, including the average over all the bursts. 135

B.18 Concentration measurements for bursts LA1 to LA9, including the average over all the bursts. 136

B.19 Concentration measurements for bursts LB1 to LB9, including the average over all the bursts. 137

B.20 Concentration measurements for bursts LC1 to LC9, including the average over all the bursts. 138

B.21 Concentration measurements for bursts LD1 to LD6, including the average over all the bursts. 139

B.22 Concentration measurements for bursts LE1 to LE11, including the average over all the bursts. 140

B.23 Concentration measurements for bursts LF1 to LF11, including the average over all the bursts. 141

ABSTRACT

The prediction of berm and dune erosion during a storm is essential for storm damage assessment. Simple and transparent formulas for the cross-shore and longshore transport rates of suspended sediment and bedload on beaches are proposed and incorporated into a combined wave and current model to predict the berm and dune erosion under normally and obliquely incident irregular waves. Two small-scale experiments for two different berm profiles were conducted for the calibration of the developed numerical model. The calibrated numerical model is shown to predict the measured berm and dune erosion in these experiments as well as dune erosion measured in three large-scale tests with errors less than a factor of 2. The numerical model is used to examine the effects of the wave period and incident wave angle on the berm and dune erosion. These effects are computed to be within a factor of 2.

Chapter 1

INTRODUCTION

Beaches have a significant role in providing recreational and economic opportunities, ecological and environmental benefits and storm protection for the coastline. Erosion is a serious, recurring problem for many beaches that is only exacerbated during large storm events. As a result, beach maintenance, in the form of beach nourishment, is necessary to preserve this critical resource. In the U.S., a beach nourishment project typically includes the construction and maintenance of a wide berm and a high dune (Coastal Engineering Manual 2003). Accurate prediction of dune and berm erosion is critical in determining the scale and timing of such projects. Attempts have been made with empirical models to calculate the time-dependent beach and dune erosion during a storm using an equilibrium beach profile, however, the margin of error of these models is only within a factor of 2 when calibrated for the specific site (Kriebel and Dean 1985; Kobayashi 1987; Larson and Kraus 1989). Additionally, these models have not been validated for oblique waves or successive of storms, which would be useful in assessing a beach nourishment project for real world scenarios. Process-based numerical models relying on sediment transport processes have also been created (e.g., Nairn and Southgate 1993), but currently, these may not be more accurate.

This study was an extension of previous efforts to advance the prediction of sediment transport on beaches by synthesizing available data and formulas for suspended sand and bedload transport rates (Kobayashi et al. 2007a). Use was made

of the computationally improved combined wave and current model by Kobayashi et al. (2008), which was based on the time-averaged continuity, momentum and energy equations. This model provided hydrodynamic input to the proposed sediment model, which relied on simple formulas for the suspended sand and bedload transport rates on beaches. A sediment transport model developed with basic sediment dynamics should be able to predict the beach and dune erosion in both small-scale and large-scale experiments even if no accepted similitude exists.

Two separate laboratory experiments were analyzed with the numerical model in an effort to verify its performance. The first experiment was a set of small-scale tests, performed in this study, to evaluate the how berm and dune geometry affect beach erosion during a storm. Two different berm and dune geometries were experimented with, one consisting of a high and narrow berm and the other with a low and wide berm. A storm was simulated by creating a time-dependent storm tide, a combination of tide and storm surge, through changing the still water level of the tank above the original datum. A large-scale experiment performed by van Gent et al. (2006) complemented the first experiment. The initial beach geometry remained constant for all tests in this experiment, but it was compromised of a typical Dutch dune with a steep seaward slope lacking a berm. Three tests were conducted, each with a different peak period T_p. For both experiments, the agreement with the present numerical model was within a factor of 2 error with no calibration of the empirical parameters.

The verified model was then evaluated for obliquely incident waves for both the small-scale and large-scale experiments. For oblique waves, the onshore wave energy flux decreases as the incident wave angle increases, but a longshore current is generated that can amplify sediment mobility and suspension. Therefore, as the incident wave angle increases, the berm and dune erosion may not decrease proportionately as one might expect.

In the following chapters, the small-scale experiments are described first in Chapter 2 with the results discussed in Chapter 3. Chapter 4 presents background and coupling of the combined wave and current model with the sediment transport model. Immediately following this, the model is compared with the small and large-scale experiments in Chapter 5 and 6, respectively. The effect of obliquely incident wave angles on berm and dune erosion is evaluated in Chapter 7. Finally, a summary of the study results is offered in Chapter 8, which is followed by the appendices. It is noted that a summary of this study has been presented by Kobayashi, Buck, Payo and Johnson (2007).

Chapter 2

SMALL SCALE EXPERIMENTAL METHODS

2.1 Dune Erosion Experiments

The beach erosion experiments were performed in a wave tank located in the basement of DuPont Hall at the University of Delaware. The tank measured 30 m long, 2.4 m wide and 1.5 m deep. The tank was modified in order to minimize the amount of sand needed to construct a beach. First, a plywood beach with a slope of 1:30 was fitted to the tank, then the tank was partitioned along its centerline with a plywood wall. Sand was then deposited on the left side of the wall looking in a shoreward direction. A rock beach was constructed on the opposite side of the wall at the end of the tank to reduce wave reflection. Instrumentation included eight wave gauges, two acoustic-doppler velocimeters and two FOBS-7 as can be seen in Figure 2.1.

The characteristics of the sand included a median diameter, d_{50}, of 0.18 mm, a specific gravity, s, of 2.6 and fall velocity, w_f, of 2.0 cm/s. Unfortunately, the sand was not able to be scaled proportionately to the rest of tank, resulting in the sand acting as a coarse sediment. This potentially created difficulties for sediment transport similitude in the small-scale experiments. A piston type wave maker generated irregular waves in the tank. The irregular waves were based on a TMA spectrum with a constant spectral peak period, T_p, of 2.57 s and a spectral significant wave height, H_{mo}, ranging from 17.8 cm to 19.2 cm. Waves were run in 400 s bursts, which prevented seiching in the tank. A 10 minute rest period was

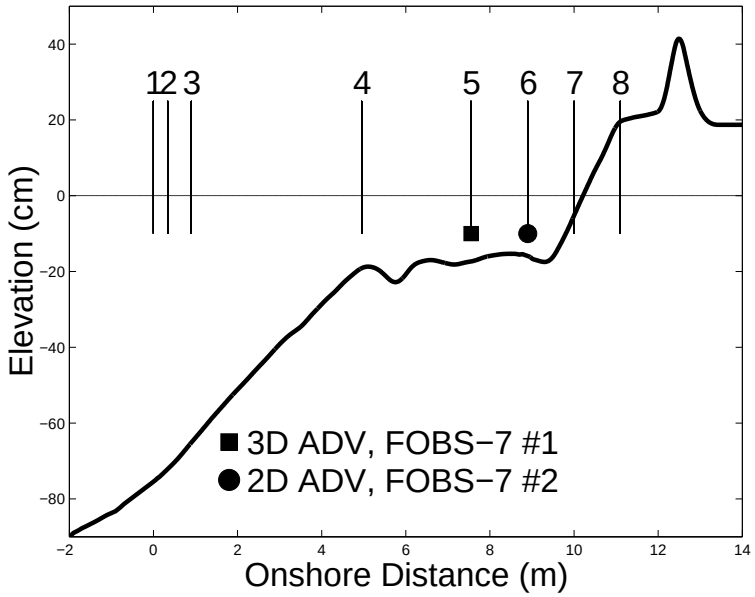

Figure 2.1: Cross-shore profile with wave gauge, ADV and FOBS setup.

instituted in between bursts to ensure that any low frequency waves had dissipated. A storm was simulated by creating a storm tide, a combination of storm surge and tide. Storm tide was created in the experiment by varying the still water level above the initial water depth of 90 cm at the wave maker.

2.2 Beach Profile Construction

The beach profile was a simple design consisting of a planar foreshore, horizontal berm and triangular dune, which is commonly found on the east coast of the U.S. The design and construction of the dune took place in several phases. The berm and dune configuration was based off previous dune erosion tests performed by Payo et al. (2006), while the profile offshore of the beach toe was very similar to the equilibrium beach profile measured by Schmied et al. (2006) in their experiments. Several dune heights and beach scales were experimented with. The beach profile was constructed with the aid of two cross-shore templates consisting of the initial

berm and dune geometry. The templates were cut out of plywood, and embedded at either wall of the tank. A vernier on a cart ensured that both templates were level with each other and the tank. The sand was then shaped to fit the template with a scraper, which consisted of a length of wood that spanned both templates. The final phase of construction required wetting the profile in an effort to compact it. This was done by simply raising the still water level of the tank until the entire profile, including the dune, was wet. Then the water level was dropped to the initial still water level of 90 cm. This wetting process exposed any undiscovered air pockets or soft spots. These imperfections were filled in and the profile was smoothed with a scraper one last time. Finally, the profile was ready for the experiments to begin.

The two dune erosion experiments that were performed were labeled experiment H and experiment L. While both experiments were subject to the same set of waves, each experiment consisted of a different beach profile configuration. For the first experiment, Experiment H, the berm height was high and the backshore width was narrow, while for the second experiment, Experiment L, the berm height was low and the backshore width was wide as apparent in Figure 2.2. The beach profiles were considered similar offshore of their intersection point at $x = 9.07$ m, referred to as x_* in these experiments. In either case, the volume of sand between this intersection point, x_*, and the dune crest was conserved. The height of the berm in Experiment L was 10 cm lower than in Experiment H and the backshore width was about 1 m wider. In addition, both experiments had identical instrumentation setups.

2.3 Experimental Setup

In each experiment, a storm was simulated by creating a time dependent storm tide, S, which was the sum storm surge and tide. This was accomplished by dividing each experiment into 6 tests, labeled in sequential order A-F. The first 4 tests were organized into the beach erosion tests, A-D, while the last two were beach

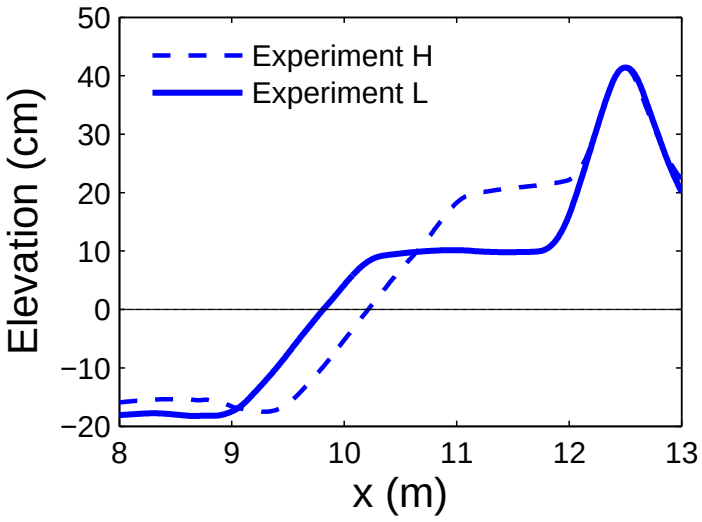

Figure 2.2: Initial berm and dune geometries.

recovery tests, E-F. In addition, each lettered test was composed of a number of 400 s wave bursts, denoted N_b. For the erosion tests, storm tide was created by raising the still water level of the tank in 5 cm increments for each successive test starting with no storm tide. The initial still water level was 90 cm above the bottom of the wave flume and this was considered the free surface datum, $z = 0$. The maximum storm tide of 15 cm occurred during test D. Initially, each lettered test lasted for 1 hr, until test D which was stopped after 6 bursts, or 0.67 hr, due to dune breaching. Previous testing by Schmied et al. (2006) showed that the recovery of the beach, i.e. accretion, was a slow and weak process in comparison to erosion. Therefore, the storm tide, S, needed to be lowered in a larger increment than it was raised at. The storm tide in E was reduced to 5 cm. Additional wave overwash may have occurred if the storm tide was not reduced sufficiently, and this was not desired since wave overwash is beyond the scope of this study. The duration was extended to 11 bursts, or 1.22 hr to accommodate the slow recovery process. For test F, the final test, storm tide was zero and the number of bursts, N_b, stayed the constant from

test E. A summary of this section is shown in Table 2.1 where T_e is the time that the test ended at.

Table 2.1: Experimental Sequence.

Test	S (cm)	N_b	T_e (hr)	Berm and Dune Evolution
A	0	9	1.00	Erosion of the steep seaward slope of the berm
B	5	9	2.00	Erosion of the berm and backshore
C	10	9	3.00	Scarping of the dune
D	15	6	3.67	Large dune erosion, minor overwash, breaching
E	5	11	4.89	Slow backshore accretion and foreshore erosion
F	0	11	6.11	Continued slow backshore accretion/foreshore erosion

2.4 Sediment Characteristics

The sand beach was built with approximately eight to nine tons of fine quarry sand. A sieve analysis was conducted with nine different sieve sizes to determine the sand size distribution as can be seen in Figure 2.3 and Table 2.2 (Lawrence and Kobayashi, 2003). A sand sample weight of 293.9 g was agitated for 20 minutes and a median diameter, d_{50}, of 0.18 mm was calculated. The density of the sand was found by placing a known mass of sand in a graduated cylinder containing a known volume of water. The amount water displaced by the sand was taken as the volume of sand. The sand had a specific gravity, $s = \rho_s/\rho_w$, of 2.6 where the ρ_s and ρ_w were the densities of the sand and fresh water, respectively. The porosity, n_p, of 0.4 for the sand was calculated from the measured dry sand mass, mixture volume and specific gravity. The measured moisture content was deemed insignificant at 0.44%. The fall velocity was determined by timing several grains of sand falling over a distance of one meter in a clear glass cylinder filled with fresh water. Sediment

Table 2.2: Summary of sieve test.

Sieve Size (mm)	Geometric Mean Diameter (mm)	Mass (g)	Percent of M_{total}	Percent Passing
2.0	-	0	0	100
0.850	1.300	2.3	0.77	99.2
0.425	0.601	0.8	0.27	99.0
0.250	0.326	6.5	2.20	96.8
0.212	0.230	10.1	3.44	93.3
0.150	0.178	132.6	45.12	48.2
0.125	0.137	65.7	22.34	25.9
0.106	0.115	48.3	16.42	9.4
0.075	0.089	26.8	9.13	0.3
Pan	-	0.9	0.30	0.0
Total		293.9	100	-

was taken from each of the nine size groups, with each test repeated ten times for each size group. Finally, the velocity was multiplied by a proportional weighting factor based on the percentage weight of a specific size group relative to the total mass, M_{total}. The calculated fall velocity was 2.0 cm/s.

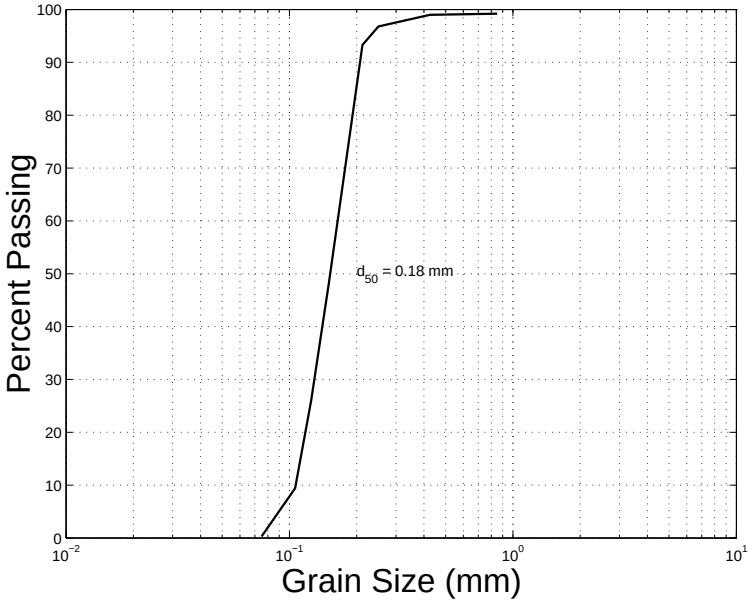

Figure 2.3: Sand grain size distribution.

2.5 Profile Measurements

Beach profiles were measured using three cross-shore transects. One transect was taken along the centerline of the tank, while the other two were taken at 30 cm on either side of the centerline. Both manual and electronic profiling were employed. Manual profiling with a vernier pointer was used from the lower swash zone to the end of the dry profile. Measurements were taken in 10 cm intervals, except in the immediate vicinity of the dune where this spacing was reduced to 2 cm in order to gain higher detail.

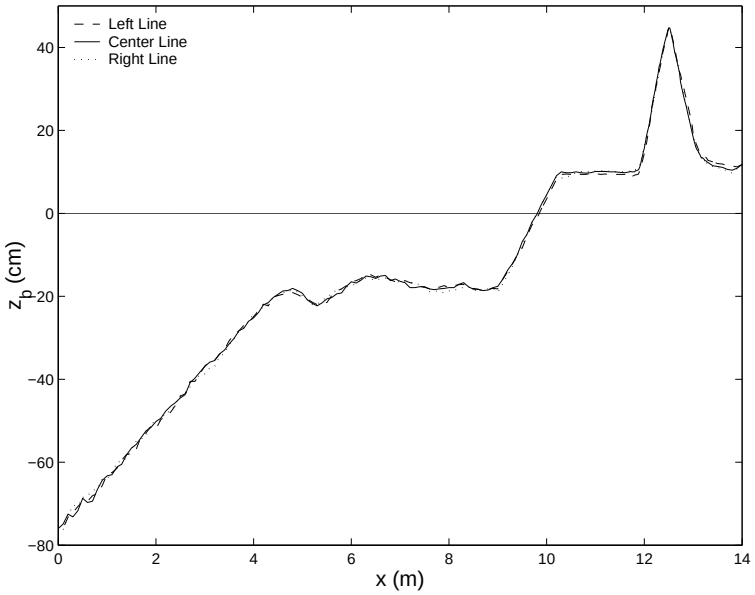

Figure 2.4: Measured transect lines before smoothing and averaging.

Electronic profiling was performed from the lower swash zone to the offshore region with a Panametrics 25MX ultrasonic precision thickness gauge, an MX-8 Multiplexer and three 1 MHz ultrasonic transducers. The 25MX thickness gauge logged the data from the transducers. The MX-8 Multiplexer bridged the transducers and the 25MX. The transducers were fixed to a transducer array that was mounted to a movable cart that allowed each transducer recorded along one of the specified cross-shore transect lines. This setup allowed for all three transect lines to be recorded at one time. Measurements were taken in 10 cm intervals along the length of the tank. There was a two point overlap in the lower swash zone between the manual and electronic profiling. All three transects were averaged into one profile, which was subsequentially smoothed using a five point running average. All three raw cross-shore transects can be seen in Figure 2.4.

2.6 Wave Gauges

Eight capacitance wave gauges were employed and their cross-shore configuration is shown in Figure 2.1. The cross shore coordinate system was such that wave gauge 1 was taken as $x = 0$ m, the offshore boundary of the numerical model. Each subsequent wave gauge was numbered in an increasing numeric order moving shoreward and their positions were noted in Table 2.3. Wave gauges 1, 2 and 3 were situated offshore in an effort to separate incident and reflected waves as well as monitor the repeatability of the experiments. Wave gauge 4 was placed over the crest of the initial bar to measure waves. The next set of wave gauges, 5 and 6, were set up in the breaking surf zone. They were located at the same cross-shore position as the ADV's and FOBS, and mounted 14.5 cm from the centerline of the cart as shown in Figure 2.6. The rest of the wave gauges were mounted along the centerline of the tank. Wave gauges 7 and 8 were buried in the bed and measured broken waves in the swash zone.

Table 2.3: Wave gauge placement.

Wave Gauge	1	2	3	4	5	6	7	8
x (m)	0.00	0.34	0.89	4.95	7.55	8.90	10.00	11.10

Before each test, the wave gauges were calibrated by constructing a calibration curve to ensure that the recordings were taken with highest degree of accuracy. Calibration was accomplished by raising the still water level of the tank to 15 cm above the mean still water level for a particular test. Then the tank was drained while the wave gauges were set to record for every 1 cm drop of the still water level. This calibration was stopped when the water level reached 10 cm below the still water level for a particular test. The calibration curve actually exhibited a linear relationship as can be seen in Figure 2.5 below. This linear relationship only failed for the buried wave gauges, 7 and 8, when the water level dropped below the level

of the bed as can be seen at the bottom of Figure 2.5. This issue was resolved by simply neglecting these points for the calibration.

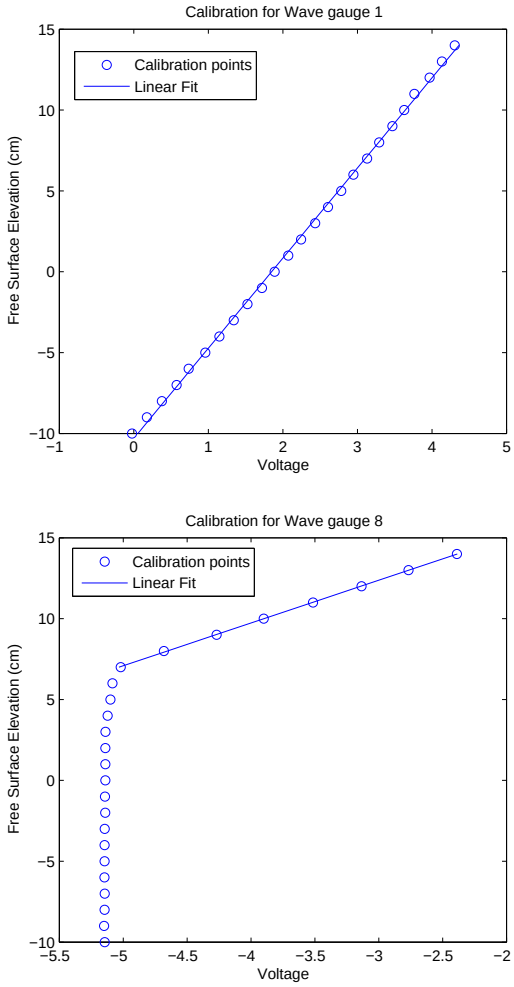

Figure 2.5: Calibration curve for wave gauge 1 (left) and wave gauge 8 (right).

2.7 Acoustic-Doppler Velocimeters

Two different Acoustic-Doppler Velocimeters, hereafter ADV's, recorded fluid velocities at a specified elevation in the water column. The 2D ADV had a side-looking probe that measured alongshore and cross-shore velocities at 5 cm from

the probe tip. The 3D ADV had a down-looking probe that recorded alongshore, cross-shore and vertical velocities at a distance of 5 cm below the probe tip. The cross-shore positions of the 2D and 3D ADVs remained constant. The ADVs were positioned on the opposite side of the cart from the wave gauges, which was 14.5 cm laterally from the centerline of the cart as can be seen in Figure 2.6.

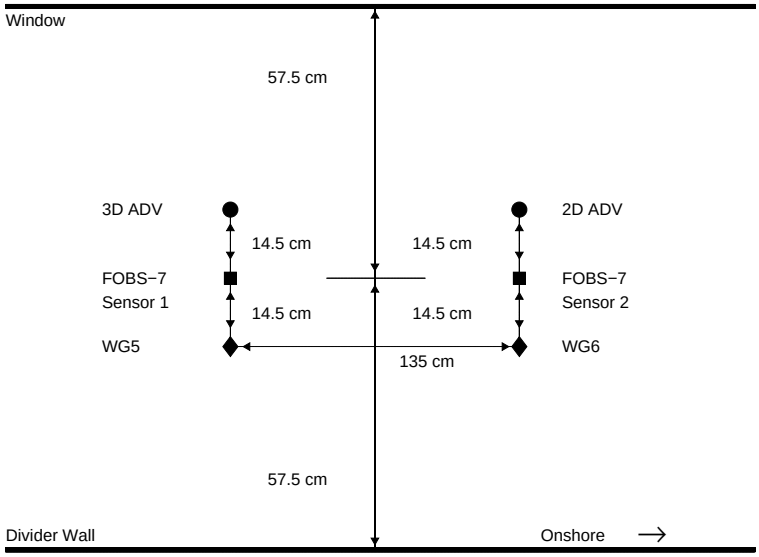

Figure 2.6: Long-shore wave gauge, ADV and FOBS Setup.

The 3D ADV was positioned at the same cross-shore location at Wave Gauge 5, x = 7.55 cm, while the 2D ADV was at the same cross-shore location as Wave Gauge 6, $x = 8.90$ cm. The 3D ADV requires at least 1-2 cm of water between its sampling point and the local bed to operate effectively. Therefore, a total of 6-7 cm of water between the tip and local bottom is required. In addition, the 3D probe needs enough water above the probe tip to eliminate any surface wave effects. Therefore, the 3D ADV could not be placed any more shoreward of its final location since it would have been too close to the free surface. The sampling volume was constant for both ADVs at 0.1 cm^3. Both ADVs were positioned at the elevation z_m of 2 cm

above the local bed to ensure that surface interactions along with a progressively accreting profile would not affect the ADV's reliability. The 3D ADV was positioned vertically above the bed using the manufacturers software, which had an accuracy of +/- 0.5 mm. The 2D ADV required manual positioning with a fine ruler to get the desired elevation z_m above the bed. The manufacturer's software automatically converted the ADV voltage values into velocities so no calibration was necessary.

2.8 Fiber Optic Sediment Monitors (FOBS-7)

Lastly, two Fiber Optic Sediment Monitors (FOBS-7), hereafter FOBS, were setup along the centerline of the tank to measure suspended sediment concentrations as shown Figure 2.1 and 2.6. The FOBS were affixed to the same cart that carried the ADVs and wave gauges 5 and 6 and their cross-shore positions remained constant. FOBS sensor 1 was located at $x = 7.55$ cm and FOBS sensor 2 was located at $x = 8.90$cm. They were set to record at an elevation of 2cm above the local bed, where the ADV's were positioned. The FOBS is the laboratory version of the optical backscatter sensor (OBS-3) used in field measurements. The FOBS measured sediment concentration by emitting infrared radiation (IR) and recording the amount of backscatter from the suspended particles in the water column. The FOBS recorded at a position 1 cm from the probe tip over a 10 mm^3 volume of water, which is shown in Figure 2.7. The FOBS were positioned by lowering them until they reached their maximum voltage of 2.6 V at the bed. Then they were slowly raised until the voltage dropped suddenly to 2.3 V to 2.1 V, which was then taken as zero coordinate for the elevation above the bed, z_m. The sensor was then raised to its final elevation of $z_m = 2$ cm above the local bed. The diameter of the sensor, D, was 1 cm.

The FOBS were calibrated before each test with the method previously described by Lawrence and Kobayashi (2003). Each FOBS was calibrated individually using a variable speed blender containing 1 l of water. The blender speed was set

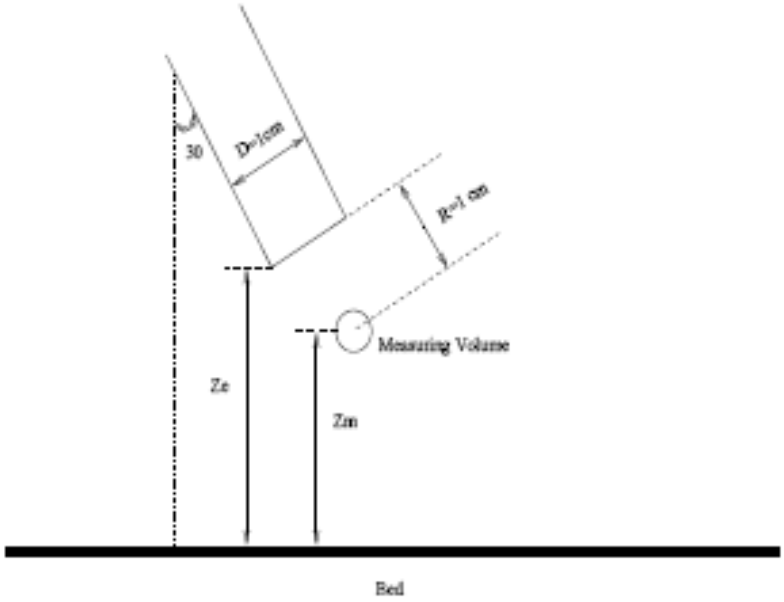

Figure 2.7: FOBS-7 setup and position relative to the local bed.

to the maximum speed without bubble formation, as the air bubbles would have interfered the with sensors. The initial measurement was recorded in clean water to get a zero for the calibration. Then 4 g of sand was placed in blender and the FOBS were set to record at 20 Hz over a one minute intervals. Recordings were taken at elevations of 5, 6 and 7 cm above the bottom of the blender, which ensured that the vertical mixing was uniform. Another 4 g of sand was added and the process was repeated. This was repeated a total of seven times for a final concentration of 28 g/l. A calibration curve was then constructed as seen in Figure 2.8.

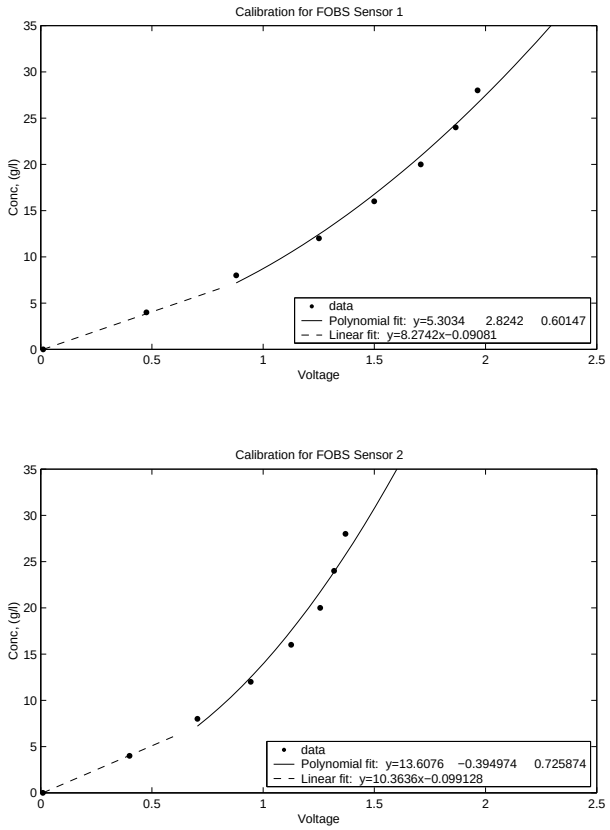

Figure 2.8: FOBS-7 calibration curve for sensor 1 (top) and sensor 2 (bottom).

2.9 Data Collection

A National Instruments 16 channel data acquisition board controlled both the wave maker and all the data logging simultaneously. This included all the data from the 8 wave gauges, 2 ADV's and 2 FOBS. The voltage signal was transmitted to the wave maker at a frequency of 20 Hz, which was also the frequency at which data was collected. For all statistical, time series and spectral analysis, the first 20 s seconds of the 400 s time series was eliminated.

2.10 Incident and Reflected Waves

Since the wave input signal was kept constant over both experiments H and L, It was necessary to check the repeatability of each set of 55 bursts by separating the incident and reflected waves. The separated incident and reflected wave spectra are plotted together in Figure 2.9. As can be seen, the incident spectra was reproduced well. The reflected spectra showed more variation due in part to the different beach profiles and storm tides present for each test. The reflected spectra was also much smaller than the incident spectra. Table 2.4 shows mean values of the incident wave spectra as well as the time series parameters where H_{mo} was spectral significant wave height and T_s and H_s were the significant period and wave height, respectively, based on the zero up-crossing method. The reflection coefficient, R, was determined by the method of Kobayashi et al. (1990) as $R = (H_{rms})_r/(H_{rms})_i$, where H_{rms} was the root-mean-square wave height and the subscripts r and i indicate the reflected and incident waves, respectively. The mean water level, $\bar{\eta}$, and standard deviation of the mean water level, σ_η, were the measured values at wave gauge 1. This will be discussed further in Chapter 3.

Table 2.4: Average incident and reflected spectral and time series parameters across each test within each experiment.

Test	$\overline{\eta}$ (cm) (WG1)	σ_η (cm) (WG1)	Incident Spectral		R	Inc.Times Series	
			H_{mo} (cm)	T_p (s)		H_s (cm)	T_s (s)
HA	-0.20	4.62	18.79	2.57	0.217	18.70	2.35
HB	-0.15	4.62	18.81	2.57	0.157	18.69	2.31
HC	-0.10	4.63	18.17	2.57	0.178	17.89	2.31
HD	-0.10	4.95	19.16	2.57	0.210	18.86	2.32
HE	-0.16	4.72	18.66	2.57	0.131	18.60	2.32
HF	-0.18	4.39	17.81	2.57	0.127	17.82	2.33
LA	-0.13	4.56	18.38	2.57	0.140	18.45	2.34
LB	-0.14	4.75	18.92	2.57	0.134	18.90	2.31
LC	-0.10	4.83	18.73	2.57	0.184	18.38	2.30
LD	-0.07	4.88	18.60	2.57	0.218	18.20	2.32
LE	-0.12	4.67	18.39	2.57	0.128	18.36	2.33
LF	-0.15	4.56	18.47	2.57	0.127	18.49	2.33

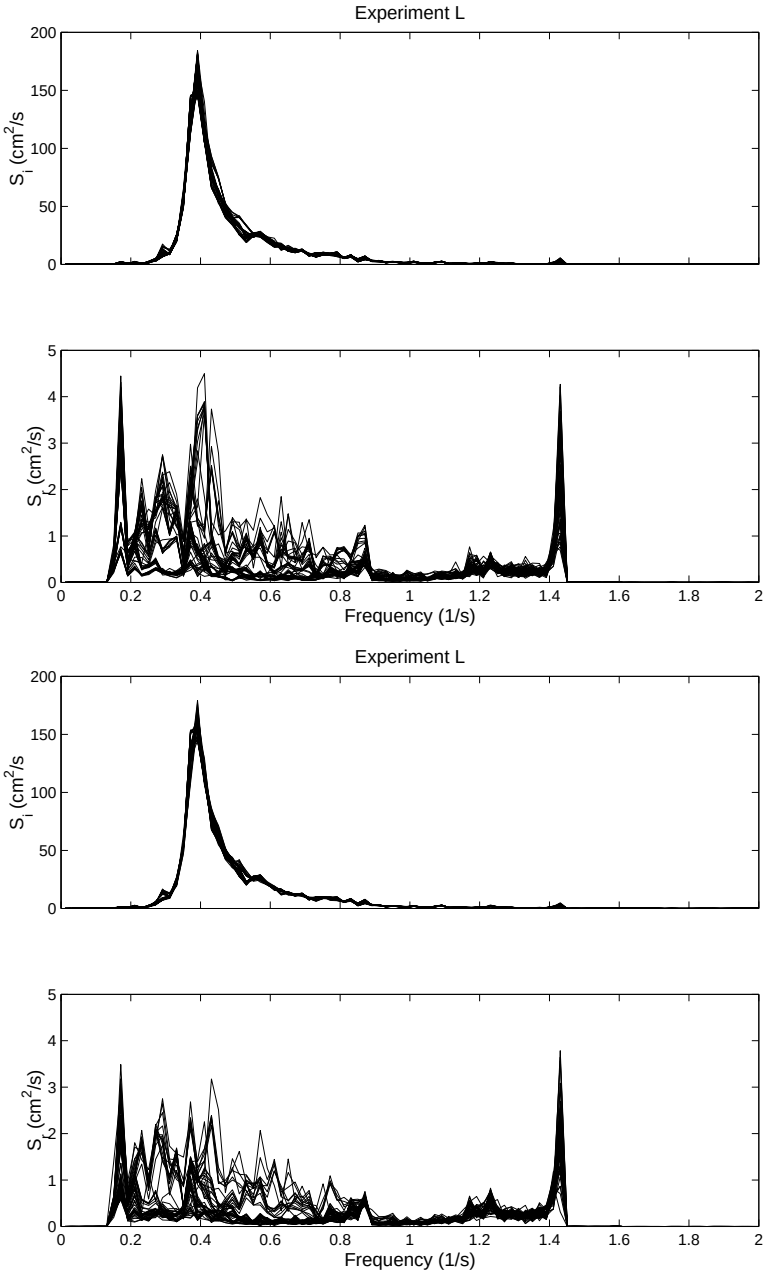

Figure 2.9: Incident and reflected wave spectra for experiment H (top) and L (bottom).

Chapter 3

SMALL SCALE DATA ANALYSIS

This chapter will discuss the data analysis for the small-scale dune erosion laboratory experiments described in Chapter 2. Please refer to Chapter 2 for the experimental setup and procedures.

3.1 Profile Evolution

As discussed in Chapter 2, the two dune erosion experiments, H and L, were divided into 6 tests each, labeled A-F. The corresponding experiment letter, H or L, was placed in front of each test letter to differentiate between similar tests in different experiments. For tests HA and LA, there was no storm tide $S = 0$, a still water level set to the datum $z = 0$, and an offshore depth of 90cm. The initial profiles in the surf zone were considered a quasi-equilibrium profile. This test simulated storm waves reaching the beach ahead of the storm tide. The erosion was limited essentially to the foreshore and berm, as can be seen in Figure 3.1, and the majority of the erosion took place during the first burst. There were nine bursts total for test A which totaled to one hour of waves. The amount of erosion rapidly and continually declined following the first burst (not shown). In addition, the profile change, $\Delta(z_b)$, for a test was calculated by subtracting the initial profile from the test profile and then plotted below the measured profiles. The profile in test LA eroded much more than the profile in test HA due to the lower and wider berm. In both tests, the berm crest eroded to about the same cross-shore coordinate. For test HA, there was little to no overwash over the berm crest, while berm overwash

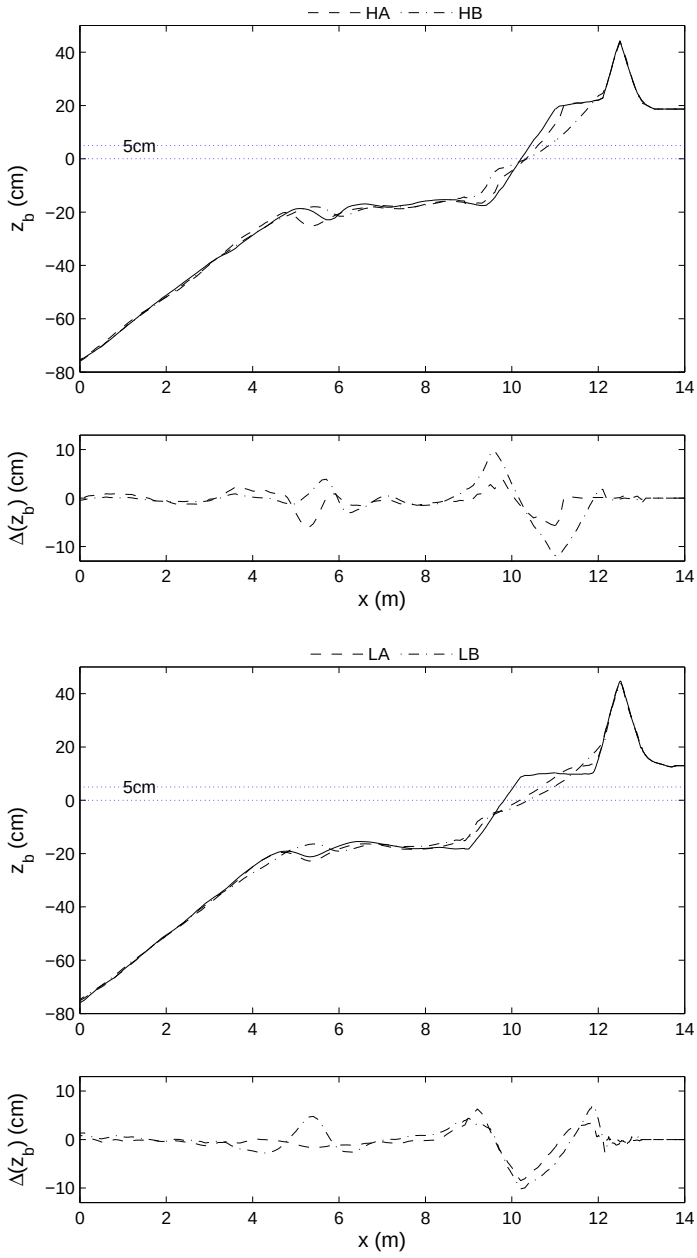

Figure 3.1: Measured profile change from time t = 0-2 hr for tests HA and HB (top) and tests LA and LB (bottom).

was frequent in test LA. Suspended fine particles in the tank were removed by draining the tank. This was repeated after each test until test D.

For tests HB and LB, a storm tide of $S = 5$ cm was introduced for a still water depth of 95 cm above the flume bottom. The profile in test HB evolved differently from that in HA. The berm eroded almost completely to the dune leaving a gentle foreshore slope at the end of HA. The rate of erosion was much slower in LB than in the preceding test, LA. As in tests HA and LA, most of the erosion took place in the first burst of the nine total bursts. HB did not erode quite as much as LB though, possibly due to the higher initial berm profile. Runup frequently reached the dune in LB, but with little effect on the dune itself. Following test B, both profiles eroded to about the same cross shore position in front of the dune toe as evident in Figure 3.1.

The storm tide was raised to $S = 10$ cm for tests HC and LC. The erosion was very slow and steady as runup reached far up the dune face. Any remaining berm was destroyed during this test while scarping became apparent on the dune face as seen in Figure 3.2. Once scarping became pronounced, further erosion of the dune was limited since the wave energy was reflected back offshore. The reflected waves actually collided with the incident waves in the swash zone. Following test C, any major differences between H and L disappeared and the profiles looked nearly identical. The foreshore slope became gentler. A total of nine bursts, or an hour of waves, was generated again.

Tests HD and LD corresponded to the full force of the storm with $S = 15$ cm. In either test, scarping of the dune continued in the first burst until the dune became severely undercut. In the second burst, the undercut face of the dune slumped, reducing the original dune width by half.

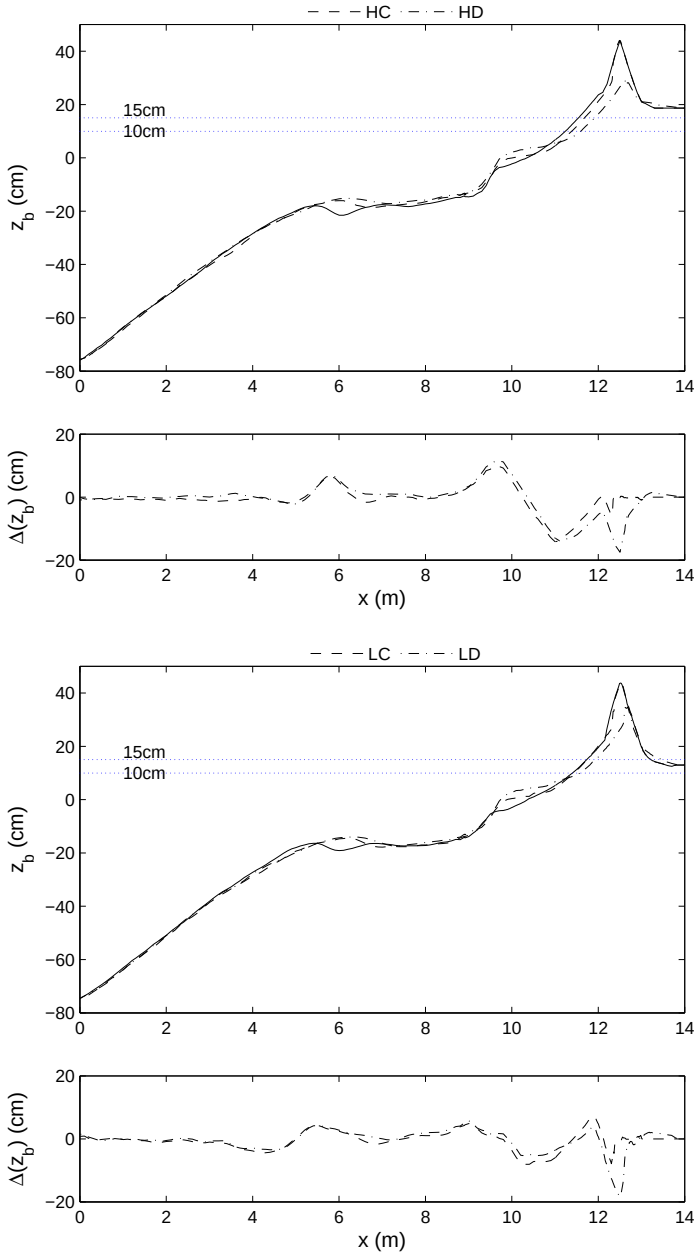

Figure 3.2: Measured profile change from t = 2-3.67 hr for tests HC and HD (top) and LC and LD (bottom).

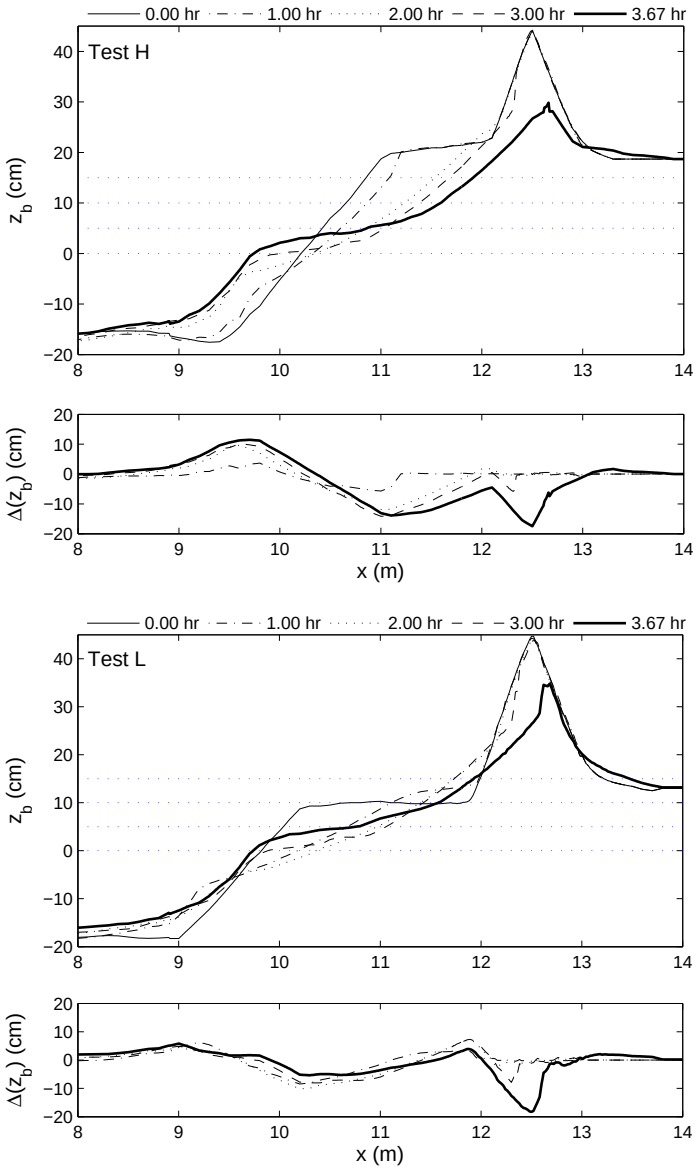

Figure 3.3: Measured profile change of berm and dune region recorded at times t = 0-3.67 hr for experiment H (top) and L (bottom).

The waves mobilized the slumped material and began to erode the new dune face. Some overwash occurred in the first two bursts, but it was not until the third burst that major overwash events occurred, leaving pooling water behind the dune. Overwash frequency and severity increased in the fourth and fifth burst along with the dune crest erosion due to overwash. There was an extremely large amount of water pooling behind the dune at this point.

A breach in the dune occurred in burst 6 for both tests HD and LD. It started as a steady seepage flow from an isolated location on the landward face of the dune. As a result, sand eroded from this area creating a weak spot on the backside of the dune. A breach was formed when a large runup event overtook the weak point. Overtopping water then spilled through the breach accompanied by a return flow that carved a channel into the dune. The location of breakthrough was not the same in HD and LD. For HD, a large breach formed off the centerline of the dune as shown in Figure 3.4. This caused problems for profile measurements since the center cross-shore transect line crossed the dune breach, while the remaining two cross-shore transect lines were unaffected. Test LD did not have this problem since the breach occurred along the left wall (looking shoreward), which did not cross any of the 3 measured cross-shore transect lines as shown in Figure 3.5. This variation in final dune geometry can be seen in Figure 3.2 with better resolution in Figure 3.3. In addition, the breach in LD was smaller since it took slightly longer to breach. Overwash became more frequent following breaching resulting in complete inundation of the area behind the dune. If another burst had been performed in either test, it is likely the breach would have become very extensive. It was unclear why LD and HD varied in their breaching, but it was likely a combination of initial small alongshore variability and slight alongshore variations in the dune erosion. Some overwash deposits were measured on the landward side of the dune.

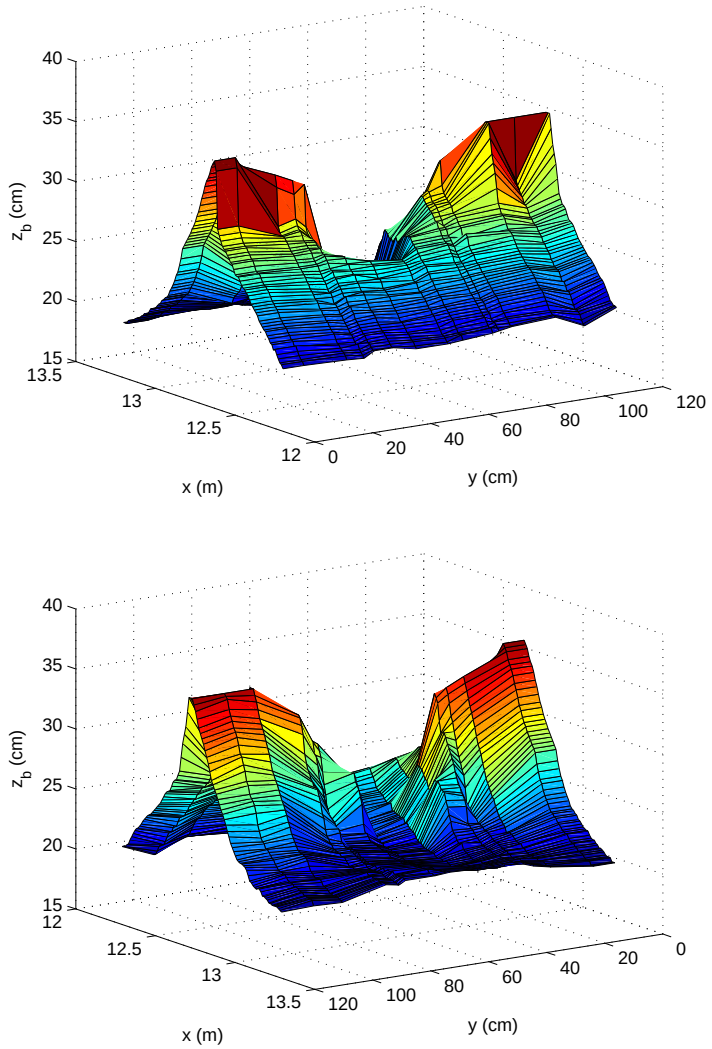

Figure 3.4: Measured dune breach geometry for test HD from the front (top) and back (bottom).

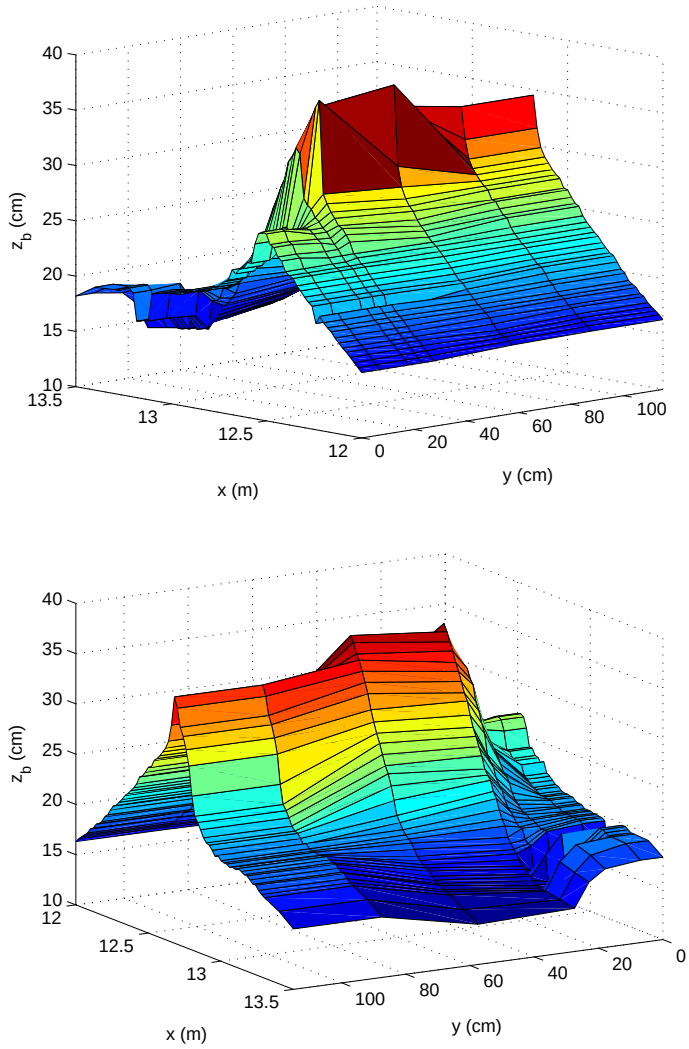

Figure 3.5: Measured dune breach geometry for test LD from the front (top) and back (bottom).

The recovery portion of the experiments followed the erosion tests and corresponded to the reduced storm tide. Tests HE and LE saw measurable accretion on the backshore and erosion on the foreshore, as shown in Figure 3.7 and 3.8. The runup fell just short of the dune, which was not eroded further. For the final tests, HF and LF, the storm tide was reduced back to zero. These tests continued the trend seen in tests HE and LE where additional minor accretion was recorded on the backshore and erosion was measured on the foreshore. The beach became a gentle, featureless slope through tests E and F. In addition, both experiments saw a significant amount of coarse sand deposited on the surface of the swash zone in the vicinity of wave gauge 7. A sediment sieve analysis yielded a d_{50} of 1.3 mm, as shown in Figure 3.6, in comparison to the d_{50} of 0.18 mm for the tank sand. This material was removed after each test.

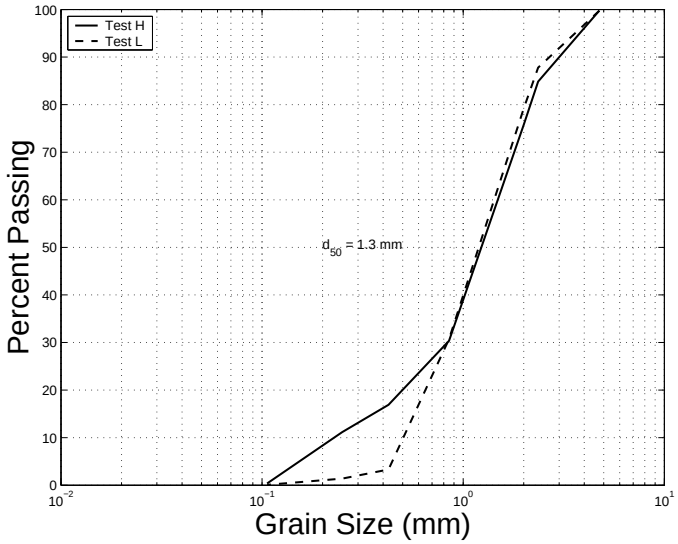

Figure 3.6: Characteristics of the coarse sand from the swash zone.

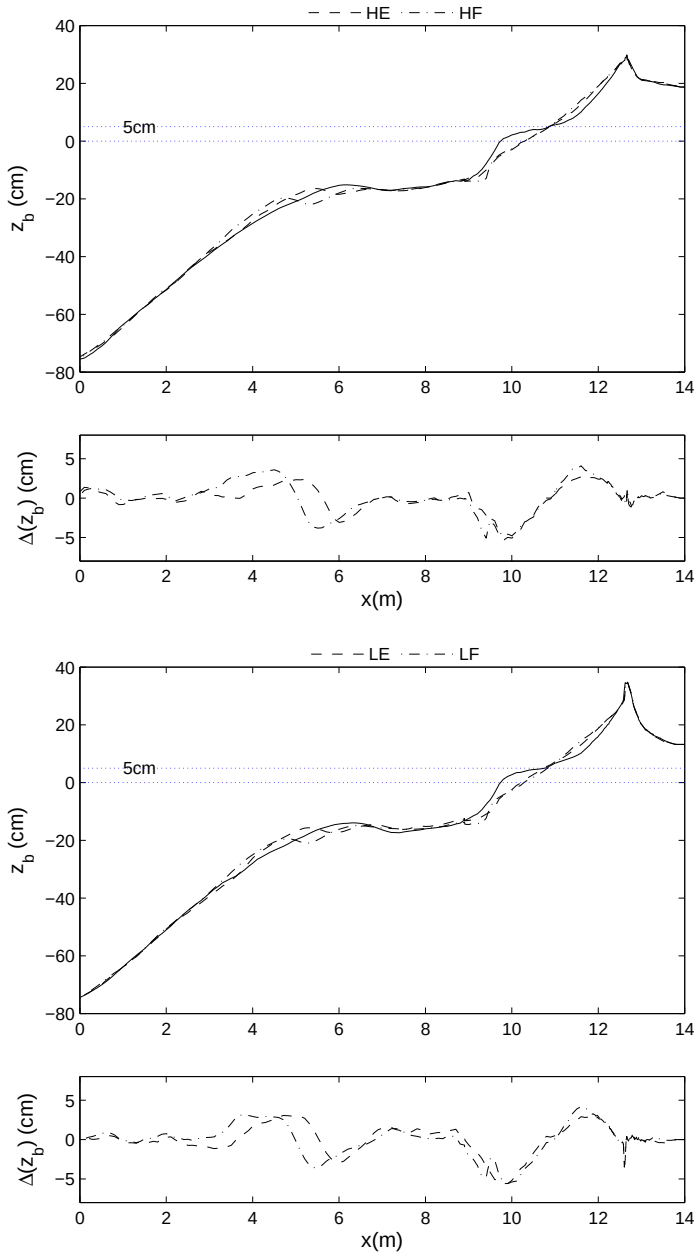

Figure 3.7: Measured profile change from t = 3.67-6.11 hr for tests HE and HF (top) and tests LE and LF (bottom).

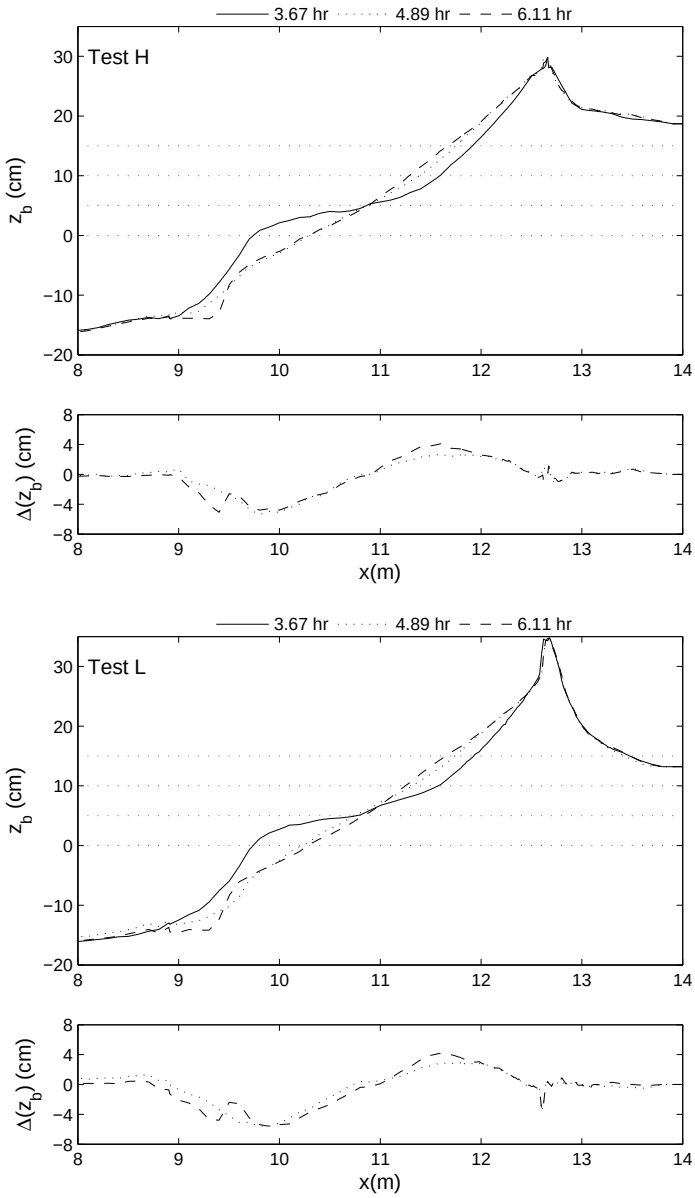

Figure 3.8: Measured profile change for berm and dune region recorded at times t = 3.67-6.11 hr for experiment H (top) and L (bottom).

The offshore profile did not remain constant through each experiment. The offshore bar in the initial profile was characterized by a narrow crest and a trough landward of this crest as shown in Figure 3.7. The waves broke on the bar at the landward edge of the terrace. Raising the still water level reduced the bar in height and widened the bar crest. In addition the bar migrated shoreward slightly. This is due to the waves breaking in a shallower depth since the waves remained constant throughout all tests. The bar became indistinguishable by tests HD and LD upon visual inspection as can be seen in Figure 3.2. But the bar returned offshore after the storm tide was reduced in Figure 3.7. Two and three dimensional ripples were present throughout both experiments from the offshore region through the edge of the swash zone. The ripples were about 0.7 cm in height and 8 cm in length.

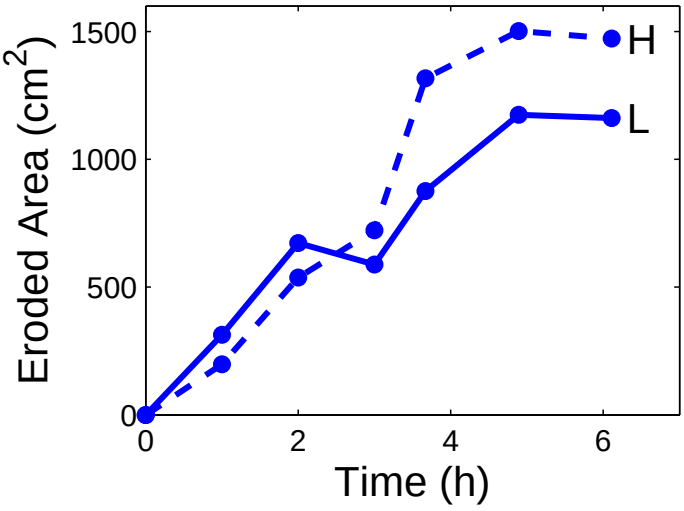

Figure 3.9: Eroded Area, A_e (cm^2), plotted for each test of experiment H and L.

The dune and berm erosion was quantified by calculating the eroded area, A_e, landward of the intersection point of the original beach profiles, $x_* = 9.07$ m, in Figure 2.2. Eroded area was essentially the net profile change between x_* and landward toe of the dune. The total eroded area was larger for experiment H than in

experiment L as can be seen in Figure 3.9. It is interesting to note that the eroded area continued to increase even when the storm tide, S, was first lowered in test E. Eventually A_e decreased slightly in test F.

3.2 Free Surface

The wave gauges measured the wave data including the mean water level, $\overline{\eta}$, spectral significant wave height, H_{mo}, peak period, T_p, and the reflection coefficient, R. These values are listed in Tables 3.1 through 3.4, where the summary of these tables has been presented in Table 2.4. The results for all eight wave gauges are found in Appendix A and B. The mean water level above the datum $z = 0$ was calculated by adding the storm tide, S, to the recorded mean water level above the still water level, $\bar{\eta}$, and represented as simply $(\bar{\eta}+S)$. Overall, $\overline{\eta}$ and σ_η did not vary much except for the two onshore buried wave gauges, 7 and 8, which were affected largely by the change in beach profile elevation. The peak period remained constant throughout both experiments at 2.57 s, which was very close to the value of 2.6 s used in the wave input file. The H_{mo} was calculated as $H_{mo} = 4\sigma_\eta$ and varied by about 1 cm throughout the experiment H. The highest H_{mo} was recorded in test HD at 19.16 cm, which coincides with the highest storm tide, $S = 15$ cm. Conversely, in experiment L the wave height varied by about 0.5 cm with the maximum height of 18.92 cm occurring during test LB instead of LD. The reflection coefficient, R, was maximum for test D and a minimum for tests E and F. The reflection coefficient for HA was actually larger than that for HD slightly, which can be attributed to the steep initial foreshore. Wave gauge 4 was placed at the edge of the initial position of the bar crest in experiment H. Large plunging breakers broke over the bar at the edge of the terrace and transformed into bores through wave gauges 5 and 6 before re-breaking on the steep foreshore at the position of gauges 7 and 8. The waves broke closer to shore as the storm tide increased, allowing more wave energy to reach the shore. The bottom elevation z_b at wave gauge 1 increased by about

Table 3.1: Experiment H: incident spectral and time series parameters.

Test	$\overline{\eta}$ (cm) (WG1)	σ_η (cm) (WG1)	Incident Spectral		R	Inc.Times Series	
			H_{mo} (cm)	T_p (s)		H_s (cm)	T_s (s)
HA1	-0.25	4.71	18.97	2.57	0.229	18.85	2.34
HA2	-0.19	4.65	18.84	2.57	0.218	18.60	2.37
HA3	-0.24	4.62	18.78	2.57	0.215	18.60	2.35
HA4	-0.19	4.61	18.80	2.57	0.218	18.83	2.36
HA5	-0.19	4.60	18.75	2.57	0.215	18.63	2.37
HA6	-0.18	4.61	18.78	2.57	0.217	18.70	2.37
HA7	-0.18	4.59	18.75	2.57	0.217	18.71	2.34
HA8	-0.19	4.57	18.69	2.57	0.213	18.62	2.34
HA9	-0.18	4.59	18.74	2.57	0.214	18.74	2.34
Avg	-0.20	4.62	18.79	2.57	0.217	18.70	2.35
HB1	-0.17	4.71	18.77	2.57	0.209	18.66	2.32
HB2	-0.12	4.65	18.95	2.57	0.161	18.91	2.32
HB3	-0.13	4.62	18.87	2.57	0.149	18.77	2.30
HB4	-0.12	4.61	18.83	2.57	0.156	18.96	2.32
HB5	-0.12	4.60	18.79	2.57	0.148	18.65	2.31
HB6	-0.18	4.61	18.78	2.57	0.148	18.57	2.30
HB7	-0.18	4.59	18.78	2.57	0.149	18.56	2.32
HB8	-0.19	4.57	18.77	2.57	0.148	18.61	2.32
HB9	-0.18	4.59	18.76	2.57	0.144	18.53	2.30
Avg	-0.15	4.62	18.81	2.57	0.157	18.69	2.31
HC1	-0.15	4.63	18.27	2.57	0.169	18.00	2.30
HC2	-0.13	4.65	18.29	2.57	0.177	18.02	2.31
HC3	-0.09	4.64	18.22	2.57	0.177	17.80	2.32
HC4	-0.09	4.64	18.20	2.57	0.181	17.92	2.30
HC5	-0.08	4.63	18.15	2.57	0.180	17.88	2.33
HC6	-0.12	4.64	18.14	2.57	0.179	17.89	2.31
HC7	-0.09	4.62	18.11	2.57	0.179	17.85	2.31
HC8	-0.07	4.62	18.09	2.57	0.181	17.85	2.29
HC9	-0.09	4.62	18.07	2.57	0.176	17.78	2.32
Avg	-0.10	4.63	18.17	2.57	0.178	17.89	2.31
HD1	-0.14	5.04	19.32	2.57	0.224	19.02	2.33
HD2	-0.08	4.98	19.27	2.57	0.216	19.03	2.35
HD3	-0.08	4.95	19.17	2.57	0.209	18.93	2.32
HD4	-0.06	4.92	19.04	2.57	0.206	18.73	2.31
HD5	-0.06	4.90	19.00	2.57	0.203	18.70	2.31
HD6	-0.19	4.93	19.14	2.57	0.202	18.74	2.30
Avg	-0.10	4.95	19.16	2.57	0.210	18.86	2.32

Table 3.2: Experiment H: incident spectral and time series parameters (continued).

Test	$\overline{\eta}$ (cm) (WG1)	σ_η (cm) (WG1)	Incident Spectral		R	Inc.Times Series	
			H_{mo} (cm)	T_p (s)		H_s (cm)	T_s (s)
HE1	-0.30	4.69	18.48	2.57	0.141	18.41	2.34
HE2	-0.18	4.74	18.76	2.57	0.124	18.63	2.33
HE3	-0.16	4.73	18.75	2.57	0.130	18.64	2.33
HE4	-0.16	4.73	18.71	2.57	0.131	18.57	2.29
HE5	-0.15	4.71	18.67	2.57	0.136	18.63	2.30
HE6	-0.15	4.72	18.66	2.57	0.132	18.57	2.30
HE7	-0.13	4.71	18.63	2.57	0.137	18.63	2.32
HE8	-0.14	4.71	18.59	2.57	0.129	18.42	2.32
HE9	-0.14	4.72	18.70	2.57	0.130	18.67	2.28
HE10	-0.14	4.71	18.66	2.57	0.125	18.69	2.32
HE11	-0.14	4.70	18.63	2.57	0.126	18.70	2.34
Avg	-0.16	4.72	18.66	2.57	0.131	18.60	2.32
HF1	-0.28	4.46	17.98	2.57	0.117	17.78	2.30
HF2	-0.21	4.44	17.94	2.57	0.122	17.89	2.33
HF3	-0.20	4.40	17.86	2.57	0.125	17.84	2.37
HF4	-0.18	4.38	17.77	2.57	0.123	17.84	2.33
HF5	-0.17	4.37	17.74	2.57	0.130	17.81	2.33
HF6	-0.17	4.38	17.81	2.57	0.133	17.85	2.32
HF7	-0.16	4.38	17.83	2.57	0.135	17.89	2.33
HF8	-0.17	4.40	17.90	2.57	0.128	17.92	2.33
HF9	-0.16	4.38	17.79	2.57	0.128	17.79	2.33
HF10	-0.16	4.35	17.69	2.57	0.134	17.73	2.34
HF11	-0.15	4.33	17.60	2.57	0.127	17.67	2.34
Avg	-0.18	4.39	17.81	2.57	0.127	17.82	2.33

Table 3.3: Experiment L: incident spectral and time series parameters.

Test	$\overline{\eta}$ (cm) (WG1)	σ_η (cm) (WG1)	Incident Spectral		R	Inc.Times Series	
			H_{mo} (cm)	T_p (s)		H_s (cm)	T_s (s)
LA1	-0.17	4.63	18.53	2.57	0.183	18.42	2.38
LA2	-0.15	4.59	18.49	2.57	0.139	18.38	2.36
LA3	-0.12	4.56	18.38	2.57	0.130	18.43	2.36
LA4	-0.12	4.56	18.38	2.57	0.132	18.46	2.35
LA5	-0.12	4.54	18.36	2.57	0.138	18.56	2.32
LA6	-0.13	4.53	18.32	2.57	0.132	18.49	2.32
LA7	-0.12	4.54	18.32	2.57	0.133	18.46	2.32
LA8	-0.11	4.53	18.35	2.57	0.141	18.56	2.33
LA9	-0.11	4.52	18.27	2.57	0.136	18.33	2.31
Avg	-0.13	4.56	18.38	2.57	0.140	18.45	2.34
LB1	-0.20	4.69	18.83	2.57	0.125	18.74	2.29
LB2	-0.15	4.73	18.96	2.57	0.126	18.92	2.28
LB3	-0.14	4.74	18.95	2.57	0.135	19.20	2.36
LB4	-0.13	4.76	18.96	2.57	0.130	19.02	2.29
LB5	-0.14	4.77	18.96	2.57	0.135	18.93	2.30
LB6	-0.13	4.77	18.92	2.57	0.137	18.84	2.32
LB7	-0.12	4.79	18.94	2.57	0.139	18.95	2.33
LB8	-0.14	4.77	18.88	2.57	0.139	18.81	2.31
LB9	-0.12	4.77	18.86	2.57	0.137	18.72	2.30
Avg	-0.14	4.75	18.92	2.57	0.134	18.90	2.31
LC1	-0.15	4.84	18.91	2.57	0.170	18.52	2.27
LC2	-0.11	4.84	18.86	2.57	0.174	18.47	2.30
LC3	-0.10	4.84	18.82	2.57	0.180	18.51	2.32
LC4	-0.11	4.84	18.78	2.57	0.186	18.39	2.29
LC5	-0.09	4.80	18.56	2.57	0.190	18.20	2.33
LC6	-0.09	4.84	18.67	2.57	0.188	18.37	2.31
LC7	-0.10	4.82	18.66	2.57	0.187	18.35	2.29
LC8	-0.10	4.83	18.68	2.57	0.189	18.33	2.27
LC9	-0.09	4.83	18.65	2.57	0.191	18.33	2.30
Avg	-0.10	4.83	18.73	2.57	0.184	18.38	2.30
LD1	-0.09	4.85	18.38	2.57	0.228	17.98	2.34
LD2	-0.05	4.92	18.73	2.57	0.223	18.23	2.31
LD3	-0.04	4.94	18.84	2.57	0.215	18.52	2.31
LD4	-0.06	4.82	18.33	2.57	0.217	17.97	2.33
LD5	-0.05	4.80	18.33	2.57	0.217	17.97	2.33
LD6	-0.14	4.92	19.00	2.57	0.208	18.55	2.33
Avg	-0.07	4.88	18.60	2.57	0.218	18.20	2.32

Table 3.4: Experiment L: incident spectral and time series parameters (continued).

Test	$\overline{\eta}$ (cm) (WG1)	σ_η (cm) (WG1)	Incident Spectral		R	Inc.Times Series	
			H_{mo} (cm)	T_p (s)		H_s (cm)	T_s (s)
LE1	-0.16	4.63	18.14	2.57	0.133	18.06	2.34
LE2	-0.14	4.68	18.39	2.57	0.122	18.36	2.31
LE3	-0.11	4.70	18.47	2.57	0.129	18.41	2.31
LE4	-0.11	4.70	18.47	2.57	0.124	18.38	2.33
LE5	-0.11	4.67	18.37	2.57	0.129	18.36	2.33
LE6	-0.11	4.68	18.40	2.57	0.128	18.31	2.35
LE7	-0.11	4.68	18.42	2.57	0.130	18.41	2.34
LE8	-0.10	4.67	18.40	2.57	0.129	18.46	2.33
LE9	-0.10	4.67	18.40	2.57	0.125	18.37	2.35
LE10	-0.11	4.66	18.38	2.57	0.124	18.33	2.34
LE11	-0.11	4.67	18.41	2.57	0.132	18.46	2.34
Avg	-0.12	4.67	18.39	2.57	0.128	18.36	2.33
LF1	-0.18	4.56	18.32	2.57	0.121	18.17	2.35
LF2	-0.17	4.57	18.42	2.57	0.121	18.31	2.32
LF3	-0.15	4.58	18.55	2.57	0.124	18.47	2.31
LF4	-0.15	4.57	18.52	2.57	0.126	18.67	2.34
LF5	-0.13	4.57	18.59	2.57	0.131	18.65	2.32
LF6	-0.14	4.57	18.55	2.57	0.131	18.60	2.32
LF7	-0.14	4.56	18.48	2.57	0.128	18.60	2.33
LF8	-0.14	4.56	18.49	2.57	0.128	18.50	2.34
LF9	-0.14	4.55	18.42	2.57	0.131	18.55	2.33
LF10	-0.13	4.55	18.39	2.57	0.128	18.40	2.34
LF11	-0.13	4.55	18.43	2.57	0.132	18.48	2.36
Avg	-0.15	4.56	18.47	2.57	0.127	18.49	2.33

1 cm over the course of both experiments indicating negligible profile change well outside of the surf zone.The buried wave gauges, 7 and 8, required some extra finesse to obtain the mean water level, $\bar{\eta}$, above the still water level. When no waves were present, wave gauges 7 and 8 were not submerged for tests A, B, E, and F, but they were submerged for tests C and D. When the elevation of the beach, z_b, at these gauges was higher than the still water level, the emerged gauges measured the mean depth, $\bar{h}$, and the sum of $(z_b + \bar{h})$ corresponded to the mean water level above the datum $z = 0$. On the other hand, if the still water level, was higher than the elevation of the bottom, z_b, the submerged gauge measured the mean water level $\bar{\eta}$ above the still water level and the mean water level above $z = 0$ cm was given by $(S + \bar{\eta})$ in the same way as for wave gauges 1-6. In addition, the elevation of the local bed at wave gauges 7 and 8 was recorded before and after each burst to judge whether these gauges were submerged or not.

3.3 Velocity

The time series of the mean cross-shore horizontal velocity were averaged to obtain the mean velocity, $\overline{U}$, which was always negative signifying an offshore return current. The velocities were recorded at two different cross-shore locations. For both sensors, the mean velocity, $\overline{U}$, and its corresponding standard deviation, σ_U, were within the same range as those recorded by Schmied et al. (2006) at an elevation z_m of 2 cm above the bed. For both experiments, $\bar{U}$ ranged from -7.14 cm/s to -2.86 cm/s for the 2D ADV and from -8.77 cm/s to -4.20 cm/s for the 3D ADV. For full results see the tables in Appendix A and B. The standard deviation of the velocity, σ_U, for both sensors ranged from 14.36 cm/s to 21.51 cm/s with the largest measurements coming during the highest still water level. The mean velocity, $\overline{U}$, followed the same trend for both experiments as seen in Figure 3.10.

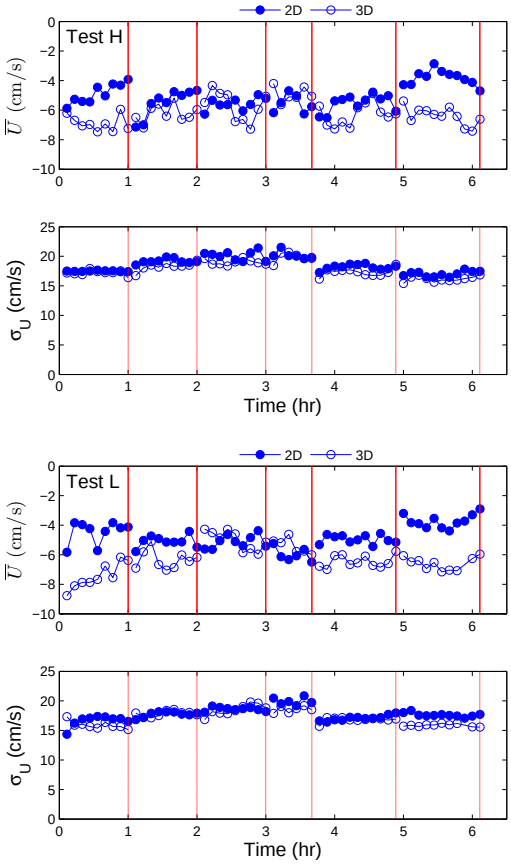

Figure 3.10: Time series for measured mean velocity, $\bar{U}$, and standard deviation of velocity, σ_U for experiment H (top) and L (bottom).

The $\overline{U}$ for the 2D ADV was largest when $S = 0$ cm for tests A and F, but decreased with increasing storm tide, S. The 3D ADV followed the opposite trend as the largest measurements coincided with the larger values of S. In addition, σ_U increased with S as well. This trend may be attributed to the 2D ADVs proximity to the swash zone compared with the 3D ADV. Following test LA, the 2D sensor was perched right on the edge of the submerged beach profile and there was actually some scour of the sand underneath the probe tip. As the storm tide increased, the the swash zone migrated shoreward, creating more similar wave conditions for both ADV's. Since there were no net alongshore currents, the measured mean longshore velocities, $\bar{V}$, were nearly zero. Only the 3D ADV had the capability to measure the vertical velocity, W, which was considered negligibly small.

3.4 Concentration

The two FOBS sensors recorded the concentration measurements. The FOBS sensors (see Figure 2.6) were referred to as C1 for sensor 1 and C2 for sensor 2. The measured volumetric concentrations were calculated by dividing the concentration, in (g/l), by 2600, since sand had a specific gravity of 2.6 and freshwater had a density of 1000 g/l. The mean concentration, $\overline{C}$, and the standard deviation, σ_C, were computed from the time series of both sensors and varied from 0.0007 to 0.0047 and from 0.0002 to 0.0024, respectively. Please see Appendix A and B for more detailed concentration data. The FOBS recorded the same mean concentration, $\bar{C}$, even though they were at different cross-shore locations, although the standard deviation did vary somewhat. As stated earlier, the water containing the suspended fine particles was drained and replaced with fresh water after each erosion test. For experiment H, the concentration tended to increase slowly throughout the experiment and reached a maximum for the test HD. This makes sense since a lot of material was eroded and suspended from the erosion and breaching of the dune. While LD recorded high concentration values as well, the maximum value occurred for test

LA, which may be influenced by the presence of fine particles. In the final two tests, E and F, very little sand was mobilized on the beach, and most of the sediment suspension was taking place over the bar due to intense wave breaking at the edge of the terrace. The concentration time series were also marked by periodic spikes in concentration, due to intermittent wave breaking and suspension. The correlation coefficient, γ_{UC}, was calculated by Equation (3.1) below and ranged from 0.001 to 0.287 with a typical value of 0.1.

$$\gamma_{UC} = \frac{\overline{(C - \overline{C})(U - \overline{U})}}{\sigma_C \sigma_U} \tag{3.1}$$

The mean and standard deviation of the sand concentration measured 2 cm above the local bottom were similar to those in the equilibrium profile experiments performed by Schmied et al. (2006) who measured the concentrations of the same sand at several elevations. Unfortunately, the suspended sand volume V_s could not be estimated from the mean concentration measured at a single elevation, nevertheless, the FOBS provided a picture of the relative amount of suspended sand between tests.

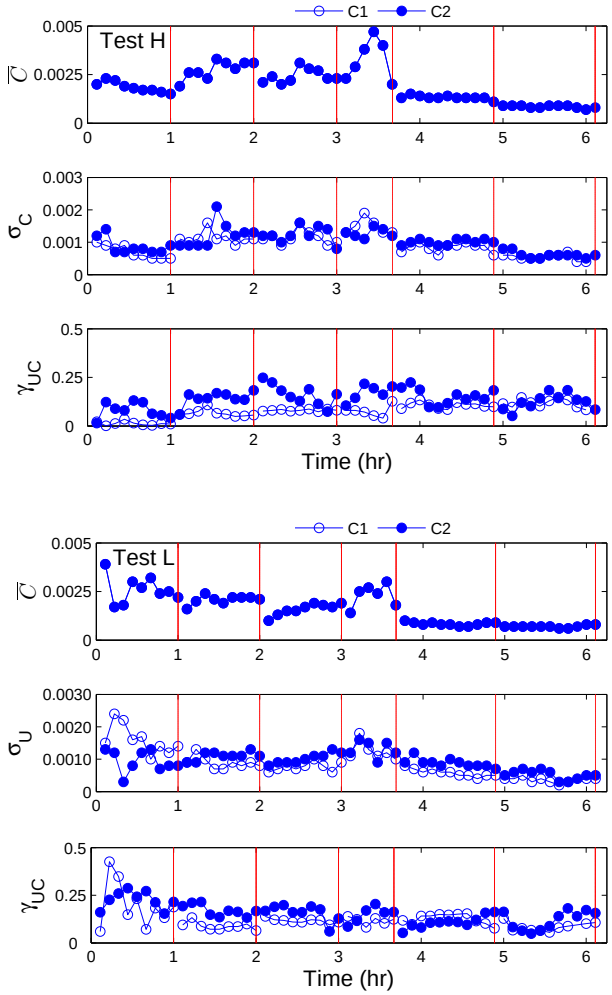

Figure 3.11: Time series for measured mean concentration, $\bar{C}$, standard deviation of concentration, σ_C, and correlation coefficient, γ_{UC}, for experiment H (top) and L (bottom).

Chapter 4

NUMERICAL MODEL DEVELOPMENT

4.1 Combined Wave and Current Model

The combined wave and current model developed by Kobayashi et al. (2007b), is an extension of the Dutch models by Reniers and Battjes (1997) and Ruessink et al. (2001). The coordinate system is defined such that the cross-shore coordinate x is positive onshore and the longshore coordinate y is positive in the down wave direction. Cross-shore and longshore velocities are depth-averaged and denoted by U and V, respectively. Incident waves are assumed to be unidirectional with $\theta =$ incident angle relative to the shore normal and uniform in the longshore direction. Incident waves propagate landward since the range of the wave angle, θ, is assumed to be within $\mid \theta \mid < 90°$. This model has the ability to include the effect of wind on the sea surface, but no wind was not present in the laboratory experiment. The model boundaries extend from the furthest offshore wave gauge, located at x = 0 m, to the landward limit in the lower swash zone.

Time averaging of the governing equations with the assumption of alongshore uniformity are taken over a number of waves. The beach is assumed to be impermeable for this study. The depth-integrated continuity equation of water requires that the cross-shore volume flux is zero in the absence of wave overtopping. The requirement of zero cross-shore volume flux is expressed as

$$\bar{h}\,\bar{U} + \frac{g\sigma_\eta^2}{C_p}\cos\theta + q_r\cos\theta = 0 \tag{4.1}$$

where $\bar{h}$ = mean water depth given by $\bar{h} = (\bar{\eta} + S - z_b)$ with $\bar{\eta}$ = mean free surface elevation above the still water level; S = storm tide above z = 0; and z_b = bottom elevation relative to z = 0; $\bar{U}$ = mean cross-shore velocity that is negative and offshore because $\cos\theta > 0$; g = gravitational acceleration; σ_η = standard deviation of the free surface elevation η; C_p = linear wave phase velocity in the mean water depth $\bar{h}$ corresponding to the spectral peak period T_p; and q_r = volume flux of a roller on the front of a breaking wave. The second term on the left hand side of Equation (4.1) is the onshore volume flux due to linear waves propagating in the direction of θ (e.g., Dean and Dalrymple 1984) where the representative period of irregular waves is chosen as the peak period T_p specified at the seaward boundary $x = 0$.

Wave direction, θ, is calculated using Snell's law

$$\sin\theta/C_p = \text{ constant} \tag{4.2}$$

where the constant value at $x = 0$ is obtained from the values of θ, $\bar{h}$ and T_p; reflected waves are neglected in this model.

The cross-shore and longshore momentum equations are written as

$$\frac{dS_{xx}}{dx} = -\rho g \bar{h} \frac{d\bar{\eta}}{dx} - \tau_{bx} \tag{4.3}$$

$$\frac{dS_{xy}}{dx} = -\tau_{by} \tag{4.4}$$

where S_{xx} = cross-shore radiation stress; ρ = water density; τ_{bx} = cross-shore bottom stress; S_{xy} = shear component of the radiation stress; τ_{by} = longshore bottom stress.

Linear wave theory for progressive waves is used to estimate S_{xx} and S_{xy}

$$S_{xx} = (nE + M_r)\cos^2\theta + E(n - \frac{1}{2}) \; ; \; S_{xy} = (nE + M_r)\cos\theta\sin\theta \tag{4.5}$$

with

$$n = C_g/C_p \; ; \qquad E = \rho g \sigma_\eta^2 \; ; \qquad M_r = \rho C_p q_r \tag{4.6}$$

where C_g = linear wave group velocity based on $\bar{h}$ and T_p; E = specific wave energy with the root-mean-square wave height defined as $H_{rms} = \sqrt{8}\ \sigma_\eta$; and M_r = momentum flux of a roller propagating with the phase velocity C_p.

The time-averaged bottom shear stresses are written as

$$\tau_{bx} = \frac{1}{2}\rho f_b \overline{U U_a} \; ; \quad \tau_{by} = \frac{1}{2}\rho f_b \overline{V U_a} \; ; \quad U_a = (U^2 + V^2)^{0.5} \tag{4.7}$$

where f_b = bottom friction factor and the overbar indicates time averaging. The bottom friction factor f_b is taken as 0.015 as before (Kobayashi et al. 2005).

The depth-averaged cross-shore and longshore velocities U and V which are expressed as

$$U = \bar{U} + r\sigma_T \cos\theta \qquad ; \qquad V = \bar{V} + r\sigma_T \sin\theta \tag{4.8}$$

where r = Gaussian variable whose mean and standard deviation are zero and unity, respectively; and σ_T = standard deviation of the depth-averaged velocity of the irregular waves propagating in the direction of θ. Linear progressive wave theory is used to obtain

$$\sigma_T = C_p \sigma_\eta / \bar{h} \tag{4.9}$$

C_p = linear wave phase velocity in the mean water depth $\bar{h}$ corresponding to the spectral peak period T_p. The standard deviations of U and V are given by

$$\sigma_U = \sigma_T \cos\theta \quad ; \quad \sigma_V = \sigma_T \mid \sin\theta \mid \tag{4.10}$$

where $\cos\theta > 0$ but $\sin\theta$ can be negative. Using equations (4.7) and (4.8), the bottom shear stresses τ_{bx} and τ_{by} are expressed as

$$\tau_{bx} = \frac{1}{2}\rho f_b \sigma_T^2 G_{bx} \quad ; \quad \tau_{by} = \frac{1}{2}\rho f_b \sigma_T^2 G_{by} \tag{4.11}$$

where approximate expressions of G_{bx} and G_{by} are given later.

The wave energy equation is written as

$$\frac{dF_x}{dx} = -D_B - D_f \quad ; \quad F_x = EC_g \cos\theta \tag{4.12}$$

where F_x = cross-shore energy flux derived from linear progressive wave theory; and D_B and D_f = energy dissipation rates due to wave breaking and bottom friction, respectively. The energy dissipation rate D_B due to wave breaking in Equation (4.12) is estimated using the formula by Battjes and Stive (1985), which was modified by Kobayashi et al. (2005) to account for the local bottom slope and to extend the computation to the lower swash zone. The breaker ratio parameter γ in this formula is typically in the range of $\gamma = 0.5$ – 1.0 (Kobayashi et al. 2007b) but should be calibrated to obtain a good agreement with the measured cross-shore variation of σ_η if such data is available. The energy dissipation rate D_f due to bottom friction is expressed as

$$D_f = \frac{1}{2}\rho f_b \sigma_T^3 G_f \tag{4.13}$$

where an approximate expression of G_f is given later.

The energy equation for the roller represented by its volume flux q_r may be expressed as (Ruessink et al. 2001)

$$\frac{d}{dx}\left(\rho C_p^2 q_r \cos\theta\right) = D_B - D_r \qquad ; \qquad D_r = \rho g \beta_r q_r \tag{4.14}$$

where the roller dissipation rate D_r is assumed to equal the rate of work to maintain the roller on the wave-front slope β_r of the order of 0.1. Use is made of the empirical formula for β_r proposed by Kobayashi et al. (2005) who included the local bottom slope effect. If the roller is neglected, $q_r = 0$ and Equation (4.14) yields $D_r = D_B$. The roller effect is included in the subsequent computation to improve the agreement for the longshore current (Kobayashi et al. 2007b).

Equations (4.1)-(4.14) are the same as those used by Kobayashi et al. (2007b) who used linear shallow-water wave theory with $C_p = (g\bar{h})^{0.5}$. Using Equations (4.9) and (4.10), Equation (4.1) can be rewritten as

$$\bar{U} = -\frac{g\bar{h}}{C_p^2}\sigma_U \sigma_* \left(1 + \frac{C_p q_r}{g\sigma_\eta^2}\right) \qquad ; \qquad \sigma_* = \sigma_\eta / \bar{h} \tag{4.15}$$

which reduces to the equation used by Kobayashi et al. (2007b) in shallow water. The landward-marching computation starting from $x = 0$ outside the surf zone is the same as before. Approximate analytical equations of G_{bx}, G_{by} and G_f have been obtained by Kobayashi et al. (2008) to reduce the computation time and improve the numerical stability. The appropriate expressions of G_{bx}, G_{by} and G_f are as follows:

$$G_{bx} = \sqrt{\frac{2}{\pi}}\ (U_* - r_m \cos\theta) + U_* \mid F_m \mid \tag{4.16}$$

$$G_{by} = \sqrt{\frac{2}{\pi}} \; (V_* - r_m \sin\theta) + V_* \mid F_m \mid \tag{4.17}$$

$$G_f = 2\sqrt{\frac{2}{\pi}} + \left(1 + U_*^2 + V_*^2\right) \mid F_m \mid + \sqrt{\frac{2}{\pi}} \; \left(U_*^2 + V_*^2 + 2r_m^2\right) \tag{4.18}$$

where $U_* = \bar{U}/\sigma_T$; $V_* = \bar{V}/\sigma_T$; $r_m = -(U_* \cos\theta + V_* \sin\theta)$; and $F_m = (V_* \cos\theta - U_* \sin\theta)$.

For the case of normally incident waves, $\sin\theta = 0$ and $V_* = 0$. Equations (4.16) - (4.18) yield $G_{bx} = 1.6\ U_*$, $G_{by} = 0$, and $G_f = (1.6 + 2.4\ U_*^2)$. For this case, Equation (4.4) requires $\tau_{by} = 0$ and Equation (4.11) yields $G_{by} = 0$. As a result, Equation (4.17) is exact. For $\sin\theta = 0$ and $V_* = 0$, G_{bx} and G_f can be integrated analytically as presented by Kobayashi et al. (2007a) who approximated the analytical expressions of G_{bx} and G_f as $G_{bx} = 1.64\ U_*$ and $G_f = (1.6 + 2.6\ U_*^2)$. These approximate equations are very similar to the above equations obtained from Equations (4.16) and (4.18).

For the case of $\mid \sin\theta \mid \ll 1$ and $\mid U_* \mid \ll \mid V_* \mid$, Equation (4.17) can be approximated as $G_{by} = V_*(0.8 + \mid V_* \mid)$. Using field data and probabilistic analyses, Feddersen et al. (2000) obtained $G_{by} = V_*(1.16^2 + V_*^2)^{0.5}$. The difference between these two approximate equations for G_{by} is less than 20% for $\mid V_* \mid < 1.4$, which is typically satisfied. Consequently, Equations (4.16)-(4.18) are adopted here for computational efficiency and stability. It is noted that the longshore momentum equation (4.4) is solved numerically to obtain τ_{by} and G_{by} by use of Equation (4.11). Equation (4.17) is solved analytically to obtain the longshore current $\bar{V}$ for the computed G_{by}. This implicit numerical procedure improves the numerical stability of the computation marching in x (similar to time).

4.2 Sediment Transport Model

A time-dependent sediment transport model such as that by Kobayashi and Johnson (2001) is physically appealing because it predicts intense but intermittent sand suspension due to breaking waves. The berm and dune erosion observed in the present experiments were slow, however, indicating that a time-averaged model is appropriate in predicting the profile evolution due to a small net cross-shore sediment transport rate. However, the small net transport rate is difficult to predict accurately. The combined wave and current model predicts the cross-shore variations of the hydrodynamic variables used in the following sediment transport model for given beach profile, water level and seaward wave conditions at $x = 0$. The bottom sediment is assumed to be uniform and characterized by d_{50} = median diameter; w_f = sediment fall velocity; and s = sediment specific gravity; n_p = porosity of bottom sediment.

First, the cross-shore variation of the degree of sediment movement is estimated using the critical Shields parameter ψ_c (Madsen and Grant 1976) which is taken as $\psi_c = 0.05$. The instantaneous bottom shear stress τ_b' is assumed to be given by $\tau_b' = 0.5\ \rho f_b(U^2 + V^2)$ where ρ = water density; and f_b = bottom friction factor taken as $f_b = 0.015$ (Kobayashi et al. 2005). The sediment movement is assumed to occur when $\mid \tau_b' \mid$ exceeds the critical shear stress, $\rho g(s-1)d_{50}\psi_c$ where g = gravitational acceleration. The probability P_b of sediment movement can be shown to be the same as the probability of $(r - r_m)^2 > F_b^2 = (R_b^2 - F_m^2)$ where $R_b = [2g(s-1)d_{50}\psi_c f_b^{-1}]^{0.5}/\sigma_T$.

$$P_b = \frac{1}{2} erfc\left(\frac{F_b - r_m}{\sqrt{2}}\right) + \frac{1}{2} erfc\left(\frac{F_b + r_m}{\sqrt{2}}\right) \qquad \text{for} \qquad F_b^2 > 0 \tag{4.19}$$

and $P_b = 1$ for $F_b^2 \leq 0$ where $erfc$ is the complementary error function.

Second, the cross-shore variation of the degree of sediment suspension is estimated using the experimental finding of Kobayashi et al. (2005) who showed

that the turbulent velocities measured in the vicinity of the bottom were related to the energy dissipation rate due to bottom friction. Representing the magnitude of the instantaneous turbulent velocity by $(D'_f/\rho)^{1/3}$ with $D'_f = 0.5\rho f_b(U^2+V^2)^{1.5}$, the probability P_s of sediment suspension is assumed to be the same as the probability of $(D'_f/\rho)^{1/3}$ exceeding the sediment fall velocity w_f. The probability P_s is then equal to the probability of $(r - r_m)^2 > F_s^2 = (R_s^2 - F_m^2)$ with $R_s = [(2/f_b)^{1/3} w_f/\sigma_T]$ and is given by

$$P_s = \frac{1}{2} erfc\left(\frac{F_s - r_m}{\sqrt{2}}\right) + \frac{1}{2} erfc\left(\frac{F_s + r_m}{\sqrt{2}}\right) \qquad \text{for} \qquad F_s^2 > 0 \tag{4.20}$$

and $P_s = 1$ for $F_s^2 \leq 0$. If $P_s > P_b$, use is made of $P_s = P_b$ assuming that sediment suspension occurs only when sediment movement occurs.

Third, the suspended sediment volume V_s per unit horizontal bottom area is estimated by modifying the sediment suspension model by Kobayashi and Johnson (2001)

$$V_s = P_s \frac{e_B D_r + e_f D_f}{\rho g(s-1) w_f} (1 + S_b^2)^{0.5} \quad ; \quad S_b = \frac{\partial z_b}{\partial x} \tag{4.21}$$

where S_b = cross-shore bottom slope; and e_B and e_f = suspension efficiencies for the energy dissipation rates D_r and D_f due to wave breaking and bottom friction, respectively. The rates D_r and D_f involved in the roller and wave energy equations are computed by the combined wave and current model. Use is made of their calibrated values of $e_B = 0.005$ and $e_f = 0.01$. The sediment suspension probability P_s is added in Equation (4.21) to ensure $V_s = 0$ if $P_s = 0$. The term $(1 + S_b^2)^{0.5}$ is the actual bottom area per unit horizontal area and essentially unity except for very steep slopes. The cross-shore and longshore suspended sediment transport rates q_{sx} and q_{sy} are expressed as

$$q_{sx} = a\bar{U}V_s \qquad ; \qquad q_{sy} = \bar{V}V_s \tag{4.22}$$

where a = empirical suspended load parameter. The parameter a accounts for the onshore suspended sediment transport due to the positive correlation between the

time-varying cross-shore velocity and suspended sediment concentration. The value of a increases to unity as the positive correlation decreases to zero. For the three small-scale equilibrium profile experiments conducted by Kobayashi et al. (2005), a was of the order of 0.2. The longshore suspended sediment transport rate q_{sy} in Equation (4.22) neglects the correlation between the time-varying longshore velocity and suspended sediment concentration, which appears to be very small if the longshore current $\bar{V}$ is sufficiently large.

Fourth, the formulas for the cross-shore and longshore bedload transport rates q_{bx} and q_{by} are devised somewhat intuitively because bedload in the surf zone has never been measured. The bedload formulas proposed by Kobayashi et al. (2008) are written as

$$q_{bx} = \frac{bP_b}{g(s-1)}\,\sigma_T^3\left(1 + U_* V_*^2 + 2F_m \sin\theta\right) G_s \tag{4.23}$$

$$q_{by} = \frac{bP_b}{g(s-1)}\,\sigma_T^3\left[V_*(1 + U_*^2 + V_*^2) - 2r_m \sin\theta\right] \tag{4.24}$$

where b = empirical bedload parameter; and G_s = bottom slope function. The sediment movement probability P_b given in Equation (4.19) accounts for the initiation of sediment movement. For normally incident waves with $\theta = 0$ and $\bar{V} = 0$, Equations (4.23) and (4.24) yield $q_{bx} = bP_b\sigma_T^3 G_s/[g(s-1)]$ and $q_{by} = 0$. Kobayashi et al. (2007a) calibrated $b = 0.002$ using the 20 water tunnel tests of Ribberink and Al-Salem (1994) and the 4 large-scale wave flume tests of Dohmen-Janssen and Hanes (2002). However, these tests were conducted for nonbreaking waves and the assumed value of $b = 0.002$ is uncertain in surf and swash zones.

The bottom slope function G_s was introduced by Kobayashi et al. (2007a) to account for the effect of the steep cross-shore slope S_b on the bedload transport rate and is expressed as

$$G_s = \tan\phi/(\tan\phi + S_b) \qquad \text{for} \qquad -\tan\phi < S_b < 0 \tag{4.25}$$

$$G_s = (\tan\phi - 2S_b)/(\tan\phi - S_b) \qquad \text{for} \qquad 0 < S_b < \tan\phi \tag{4.26}$$

where ϕ is the angle of internal friction of the sediment and $\tan\phi \simeq 0.63$ for sand (Bailard 1981). For $S_b = 0$, $G_s = 1$. Equation (4.25) corresponds to the functional form of G_s used by Bagnold (1966) for steady stream flow on a downward slope with $S_b < 0$ where the downward slope increases q_{bx}. Equation (4.26) ensures that G_s approaches negative infinity as the upward slope S_b approaches $\tan\phi$ and that Equations (4.25) and (4.26) reduce to $G_s \simeq (1 - S_b/\tan\phi)$ for $\mid S_b \mid \ll \tan\phi$. Equation (4.23) with G_s given by Equations (4.25) and (4.26) implies that the bedload transport rate q_{bx} is positive (onshore) for $S_b < (\tan\phi)/2$ and negative (offshore) for $S_b > (\tan\phi)/2$. Use is made of $\mid G_s \mid < G_m = 10$ to avoid an infinite value in the computation. The computed profile change is not very sensitive to the assumed value of G_m because the beach profile changes in such a way to reduce a very steep slope except in the region of scarping.

The landward marching computation of the present time-averaged model ends at the cross-shore location $x = x_m$ where the mean water depth $\bar{h}$ is less than about 1 cm. The following simple procedure for scarping is adopted to deal with the zone with the bottom slope $S_b > \tan\phi$. The cross-shore total sediment transport rate $q_x = (q_{sx} + q_{bx})$ at $x = x_m$ is denoted by q_{xm}. If q_{xm} is negative (offshore), q_x is extrapolated linearly to estimate q_x on the scarped face with $S_b > \tan\phi$

$$q_x = q_{xm}(x_e - x)/(x_e - x_m) \qquad \text{for} \qquad x_m < x < x_e \tag{4.27}$$

where x_e = landward limit of the scarped face whose slope is larger than $\tan\phi$. The extrapolated q_x is in the range of $q_{xm} \leq q_x \leq 0$ and the scarping zone is eroded due to the offshore sediment transport. This simple procedure does not allow onshore sediment transport due to wave overwash (Kobayashi et al. 1996).

Finally, the cross-shore beach profile change is computed using the continuity equation of bottom sediment for the case of alongshore uniformity

$$(1 - n_p)\frac{\partial z_b}{\partial t} + \frac{\partial q_x}{\partial x} = 0 \tag{4.28}$$

where t = slow morphological time for the change of the bottom elevation z_b. Equation (4.28) is solved using an explicit Lax-Wendroff numerical scheme (e.g., Nairn and Southgate 1993) to obtain the bottom elevation at the next time level. This computation procedure is repeated starting from the initial bottom profile until the end of a profile evolution test. The computation time is of the order of 10^{-3} of the test duration.

In the following three Chapters, this model is compared with the experimental data for both small-scale and large-scale experiments for normally incident waves. Lastly, the numerical model is used for both experiments to compute berm and dune erosion under obliquely incident waves.

Chapter 5

NUMERICAL MODEL COMPARISON WITH SMALL-SCALE EXPERIMENTS

This chapter compares the beach profile evolution model with the small scale experiments, H and L, under normally incident waves, $\theta = 0°$. The input specified for the model required several measured experimental variables including the initial measured profile at $t = 0$ s, sand characteristics and offshore wave conditions. The characteristics of the sand were the measured values of $d_{50} = 0.18$ mm, $w_f = 2.0$ cm/s, $s = 2.6$ and $n_p = 0.4$. The model was closed on the seaward boundary, $x = 0$, using the measured experimental values of S, T_p, $H_{mo} = 4\sigma_\eta$ and $\bar{\eta}$ at $x = 0$ m as shown in Table 5.1 below. Beyond the experimental parameters, several empirical parameters inherent to the model were set as explained in Chapter 4. The breaker ratio parameter, γ, was one of these empirical parameters as it influences the energy dissipation rate due to breaking waves. It was previously calibrated as $\gamma = 0.8$ by Kobayashi et al. (2005) for equilibrium beach profile experiments without a berm or dune based upon a similar profile below the datum $z = 0$. The measured cross-shore variation of σ_η showed good agreement with this value for γ. A constant nodal spacing of $\Delta x = 1$ cm was sufficient for the landward marching computation of the wave and current model by Kobayashi et al. (2007b).

Only the suspended load parameter, a, in Equation (5.1) was calibrated for the present comparisons. The correlation coefficient, γ_{uc}, between the simultaneously measured horizontal velocity, U, and sand concentration, C, was of the order

Table 5.1: Incident and reflected spectral and time series parameters for each test.

Test	S	N_b	T_e	T_p	$\bar{\eta}$	H_{mo}	R	
	(cm)		(hr)	(s)	(cm)	(cm)	Meas.	Comp.
HA	0	9	1.00	2.57	-0.20	18.48	0.22	0.18
HB	5	9	2.00	2.57	-0.15	18.48	0.16	0.18
HC	10	9	3.00	2.57	-0.10	18.53	0.18	0.18
HD	15	6	3.67	2.57	-0.10	19.80	0.21	0.18
HE	5	11	4.89	2.57	-0.16	18.88	0.13	0.15
HF	0	11	6.11	2.57	-0.18	17.56	0.13	0.14
LA	0	9	1.00	2.57	-0.13	18.24	0.14	0.18
LB	5	9	2.00	2.57	-0.14	19.01	0.13	0.16
LC	10	9	3.00	2.57	-0.10	19.32	0.18	0.17
LD	15	6	3.67	2.57	-0.07	19.52	0.22	0.18
LE	5	11	4.89	2.57	-0.12	18.68	0.13	0.15
LF	0	11	6.11	2.57	-0.15	18.24	0.13	0.13

of 0.1, not unlike that of the previous equilibrium profile experiments by Kobayashi et al. (2005) that yielded $a = 0.2$. Unfortunately, offshore suspended sediment transport was not sufficient with $a = 0.2$, as the erosion of the berm and dune was underpredicted. There were two possible factors affecting this. The correlation between the horizontal velocity and the sand concentration may have been reduced by the relatively steep slopes of the berm and dune. Horizontal velocity and sand concentration could not be measured in the extremely shallow water since the ADV and FOBS-7 could not operate in that region. The reduced correlation increases the value of a as explained in relation to Equation (4.22) with the value of a empirically adjusted as

$$a = 0.2 + (S_b/\tan\phi)^{0.5} \qquad \text{for} \quad S_b > 0 \tag{5.1}$$

where S_b = local bottom slope and $\tan\phi$ = limiting sand slope of 0.63 as explained in Equations (4.25) and (4.26). Equation (5.1) was applicable only for the upward slope in the onshore direction and $a = 0.2$ for $S_b \leq 0$.

A comparison of the measured and computed beach profiles for experiment

H from time $t = 1.00$ hr to $t = 6.11$ hr, corresponding to the end of tests A through F, respectively, are shown in Figure 5.1. The mean water level, $\bar{\eta} + S$, of each test is indicated in each panel. Overall, the numerical model resolves the berm and dune erosion satisfactorily but fails to account for measured profile undulations including the locally steep slope below the datum, $z = 0$. This is evident as the computed beach toe extends further offshore than it does in the measured profile. As stated in Chapter 4, the numerical model does not perform overwash computations and therefore cannot predict the minor overwash events during tests HD and LD and their associated overwash deposits. In addition, the model cannot compute dune breaching that occurred as well. This accounted for some of the measured and computed dune profile discrepancy from HD to HF.

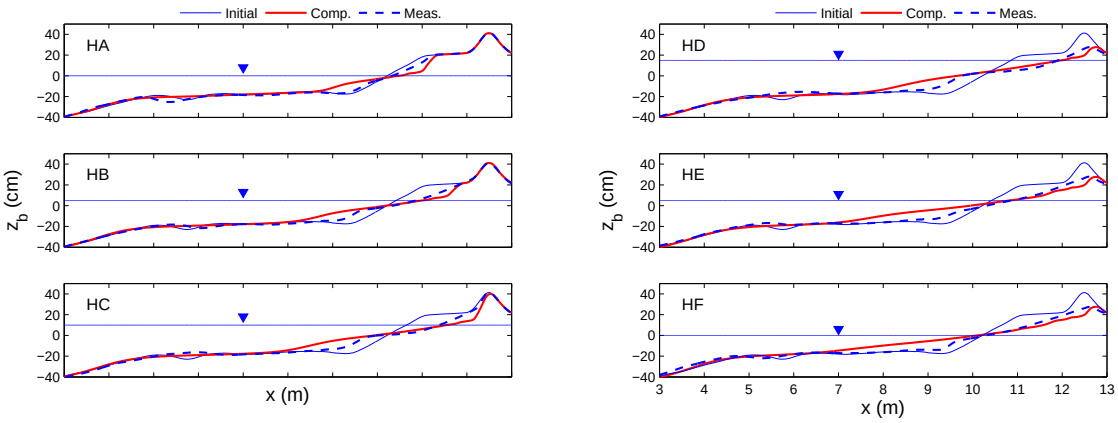

Figure 5.1: Experiment H: measured vs. computed profiles at the end of 6 tests.

Similar results were obtained for experiment L, as can be seen in Figure 5.2, except that dune erosion was overpredicted as a result of the empirical adjustment of a given by Equation (5.1). Since dune breaching occurred along the wall in this experiment, it did not affect the measured profile transects nearly as much as in experiment H. Several modifications of various parameters were explored, but agreement could not be further improved for both experiments.

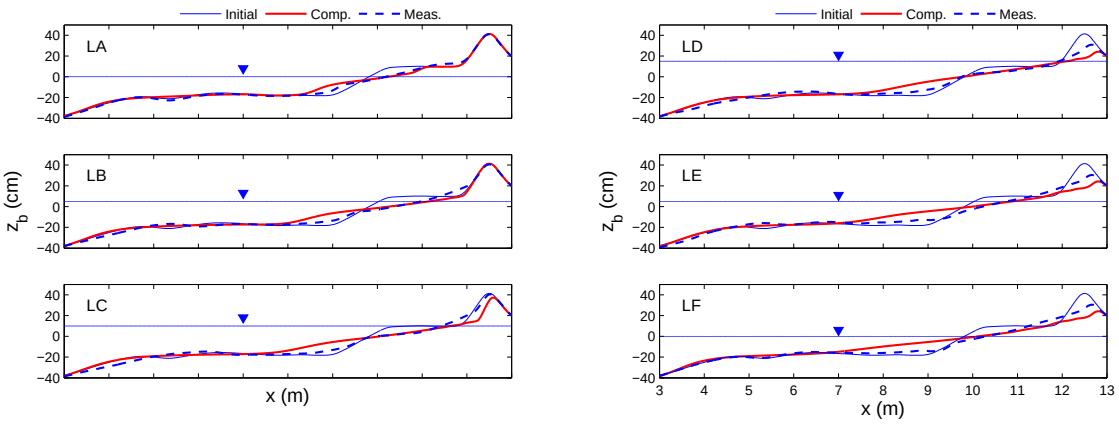

Figure 5.2: Experiment L: measured vs. computed profiles at the end of 6 tests.

The profile data also yielded the measured and computed temporal variations of the eroded area, A_e, landward of $x_* = 9.07$ m as discussed in Chapter 3 and the results are displayed in Figure 5.3 and Table 5.2. The computed results were within a factor of 2 error of the measured eroded area, A_e.

Table 5.2: Measured vs. computed eroded area, A_e, for the small scale experiments

Time	Exp. H: $A_e(cm)^2$		Exp. L: $A_e(cm)^2$	
(hr)	Meas.	Comp.	Meas.	Comp.
0.00	0	0	0	0
1.00	198	128	313	470
2.00	537	455	672	801
3.00	722	727	588	1029
3.67	1317	876	876	1127
4.89	1502	1359	1174	1515
6.11	1472	1537	1161	1682

A comparison of the computed and measured cross-shore variations of $(S+\bar{\eta})$, σ_η, $\bar{U}$ and σ_U for tests HD and LD are shown in Figure 5.4. The comparisons for the other tests presented in Appendix A and B are similar. The measured values

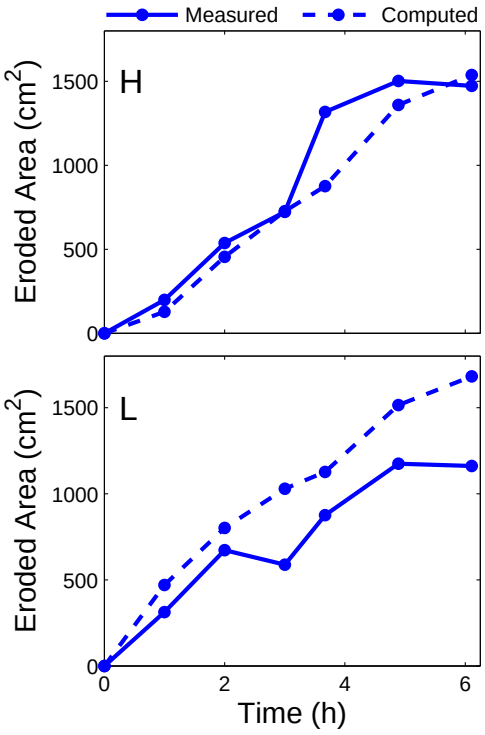

Figure 5.3: Measured vs. computed eroded area, A_e, for experiments H (top) and L (bottom)

were taken from each of the 6 bursts in these tests with little variation between the 6 bursts. The solid line refers to the computed results at the end of these tests, $t = 3.67$ h. The comparison between the measured and computed values was reasonable from about x = 8 m and seaward. Between x = 8 m and the landward limit, some discrepancy was obvious and partly attributed to the differences between the measured and predicted profiles. The model predicted the mean water level, $(S + \bar{\eta})$, to rise rapidly landward of wave gauge 8 ($x = 11.1$ m) above the berm. The wave height H_{mo}, calculated as $4\sigma_\eta$, increased slightly due to wave shoaling on the seaward slope of the terrace, while it decreased in the shoreward region due to wave breaking. The model calculates the depth averaged velocities for $\bar{U}$ and σ_U, but the measured velocities are point measurements taken at $z_m = 2$ cm above the local bed. The computed σ_U of the model was smaller than the measured σ_U as was expected. Unfortunately, velocity cannot be measured in very shallow water at present so there was no way to verify the computed values near the landward limit. Such measurements would be useful since the model predicts $\bar{U}$ to be extremely large and close to the value of σ_U in the region above the eroded berm. The wave reflection coefficient, R, was estimated from the cross-shore wave energy flux at the still water shoreline (Kobayashi et al. 2005) and was within an error of 30% as listed in Table 5.1. As stated earlier, suspended sediment transport rates could not be accurately measured in experiments H and L since measurements were taken at only one elevation above the bed.

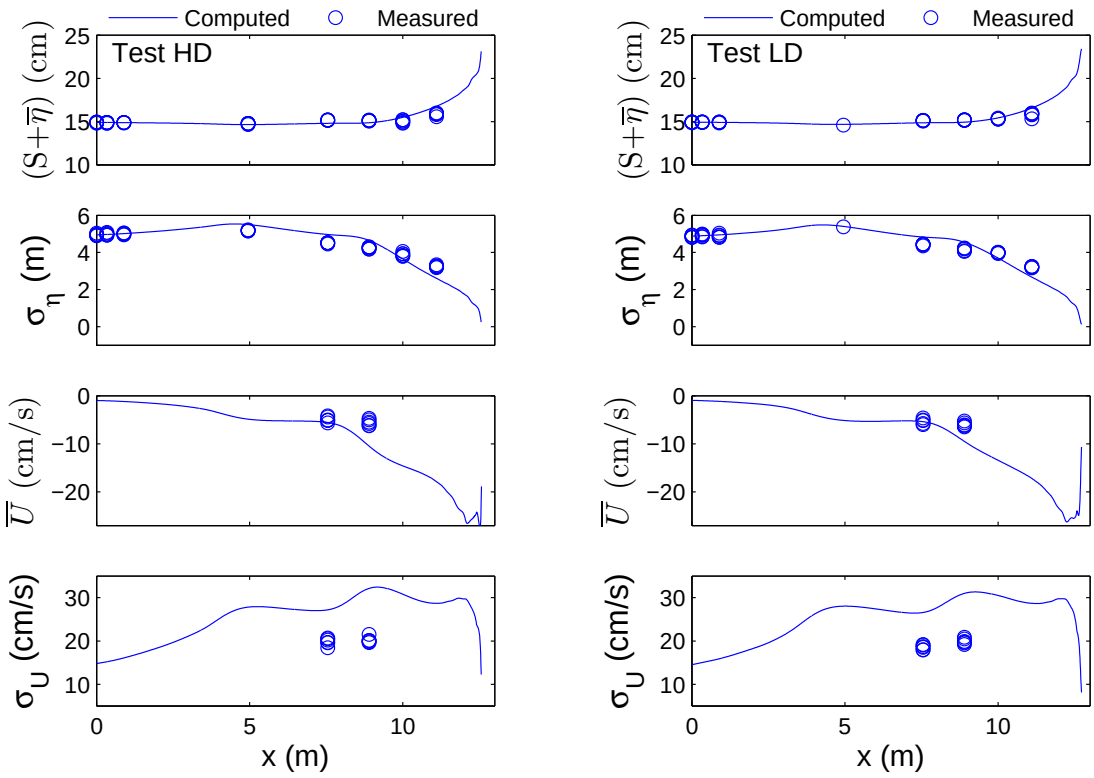

Figure 5.4: Cross-shore variations of measured vs. computed $(S + \bar{\eta})$, σ_η, $\bar{U}$ and σ_U for test HD (left) and test LD (right)

Chapter 6

NUMERICAL MODEL COMPARISON WITH LARGE-SCALE EXPERIMENTS

In a separate experiment, van Gent et al. (2006) performed large scale dune erosion tests in the Delta Flume at Delft Hydraulics Laboratory which measures 225 m long, 5 m wide and 7 m high. The fine sand was characterized by $d_{50} = 0.20$ mm, $w_f = 2.5$ cm/s, $s = 2.65$ and $n_p = 0.4$, which is similar to the sand used in the small scale experiments. The constructed profile was simpler than the small scale experiments as shown in Figure 6.1. The dune was modeled after a typical Dutch dune with no berm. The dune was composed of a steep seaward slope of 2/3 rising to a flat top located 1.67 m above the datum, $z = 0$. The still water level remained constant, indicating that storm tide, S, was zero for these tests. The maximum still water depth of 4.5 m occurred at the wave maker, where the irregular waves were generated for this experiment. The first wave gauge was placed in a depth of 3.5 m, and provided the offshore wave conditions for the model. This point was taken as the seaward boundary for the model, $x = 0$.

Three separate tests, T01, T02 and T03, were conducted with the peak periods of $T_p = 4.9$, 6.1 and 7.3 s, respectively, for the same initial dune and beach profile. The corresponding significant wave height, H_{mo}, increased slightly with period as can be seen in Table 6.1. The wave setup or set-down $\bar{\eta}$ at $x = 0$ m was not reported and $\bar{\eta} = 0$ at $x = 0$ is used for the computations.

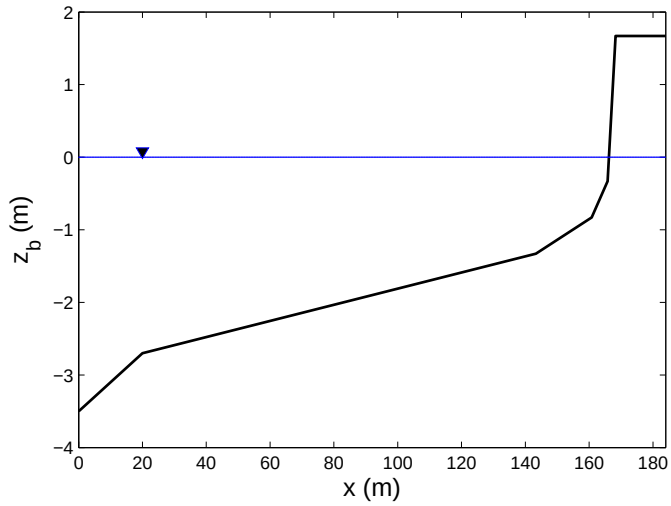

Figure 6.1: Initial profile for large-scale scale experiments T01, T02 and T03.

Table 6.1: Large Scale Tests: Wave conditions at $x = 0$ m.

Test	T_p (s)	H_{mo} (m)
T01	4.9	1.41
T02	6.1	1.49
T03	7.3	1.52

Profiles were measured at the time levels $t = 0.0$, 0.1, 0.3, 1.0, 2.04 and 6.0 hr. The empirical parameters were kept constant from the small scale experiments with $\gamma = 0.8$ and a given by Equation (5.1). The nodal spacing was increased to $\Delta x = 5$ cm since the length scale was much larger than the small-scale experiments. This nodal spacing was sufficient to resolve the steep slope of the dune face. Numerical model computations were performed for normally incident waves, $\theta = 0°$.

For all three tests, the computed profiles underpredicted the amount of dune erosion as can be seen in Figure 6.2, which only shows the region of noticeable

profile change at the end ($t = 6$ hr) of the tests. This was in contrast to the small-scale in which dune erosion was overpredicted, especially for experiment L. The offshore movement of the foreshore toe was underpredicted because of conservation of sediment volume and insufficient erosion from the dune. There was little measurable difference between the measured and computed profiles in the offshore region for all tests, which contrasts the small-scale comparisons. The model tended to produce slightly better agreement with increasing wave period.

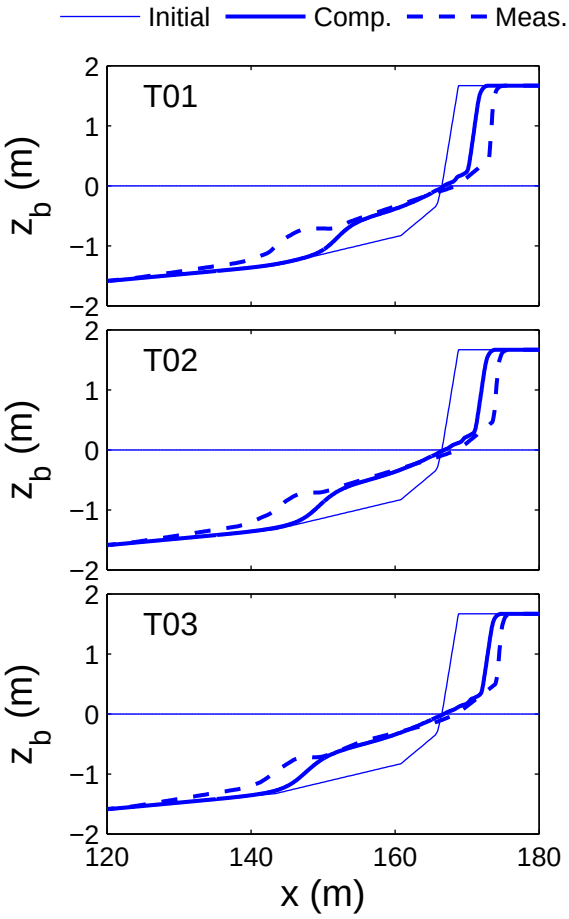

Figure 6.2: Measured vs. computed profiles at the end of tests T01 (top), T02 (middle) and T03 (bottom).

Since the dune erosion was underpredicted, it was not surprising that the eroded area, A_e, was underpredicted as well. But, A_e takes on a different definition here as it was calculated as the area eroded above the datum $z = 0$. This definition was used by van Gent et al. (2006) since dune erosion was largely confined to the region above the still water level. The eroded area, A_e, was listed in Table 6.2 for t = 0.1, 0.3, 1.0, 2.04 and 6.0 hr. It was interesting to note that at first A_e was overpredicted, but A_e was underpredicted by t = 2.04 hr. The model predicted an increase in A_e with an increase in wave period as van Gent et al. (2006) measured.

Table 6.2: Eroded area, A_e, for large-scale tests where the letters I, A, B, C, D and E are used to indicate time t later.

Letter	Time	T01: $A_e(m)^2$		T02: $A_e(m)^2$		T03: $A_e(m)^2$	
	(hr)	Meas.	Comp.	Meas.	Comp.	Meas.	Comp.
I	0.00	0.00	0.00	0.00	0.00	0.00	0.00
A	0.10	0.90	1.07	1.01	1.30	1.15	1.48
B	0.30	2.13	1.97	2.29	2.40	2.48	2.73
C	1.00	4.23	3.49	4.58	4.30	5.31	4.94
D	2.04	5.88	4.54	6.32	5.66	7.10	6.60
E	6.00	8.60	5.66	9.57	7.05	9.85	8.27

Comparison of $\bar{\eta}$, σ_η, $\bar{U}$ and σ_U above the initial profile z_b at $t = 0$ are provided in Figure 6.3. In addition, Figure 6.4 shows how the comparisons change for the final test E. All the comparisons are presented Appendix C. As with the small scale experiments, the model predicts the mean water level $(S + \bar{\eta})$ to rise rapidly near the landward limit and with the peak period T_p, although the latter may not be discernible in the first panel in these figures. The slight increase in σ_η, $(-\bar{U})$ and σ_U with period can be seen in these figures. The measurements of $\sigma_\eta = H_{mo}/4$ based on the average value of H_{mo} presented by van Gent et al. (2006) are shown in the second panel to indicate that the numerical model predicts the trend of the wave height decay.

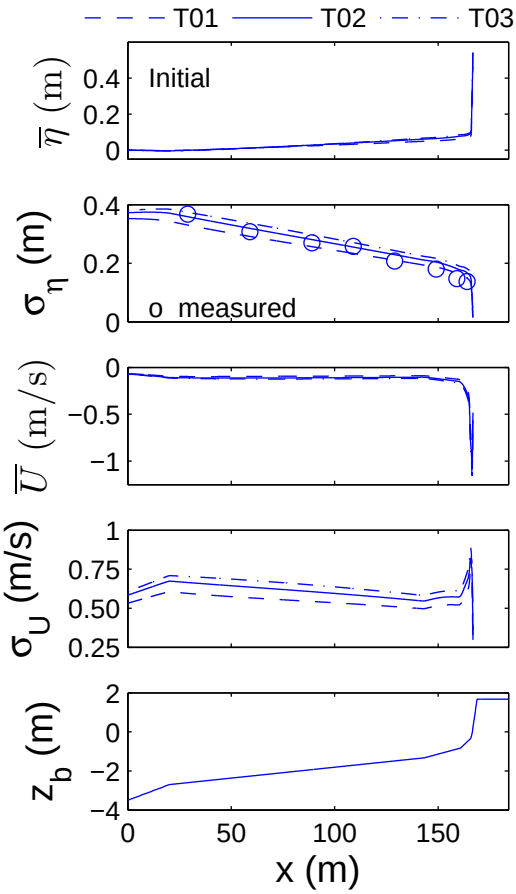

Figure 6.3: Cross-shore variations of $\bar{\eta}$, σ_η, $\bar{U}$ and σ_U for tests T01, T02 and T03 on the initial profile z_b.

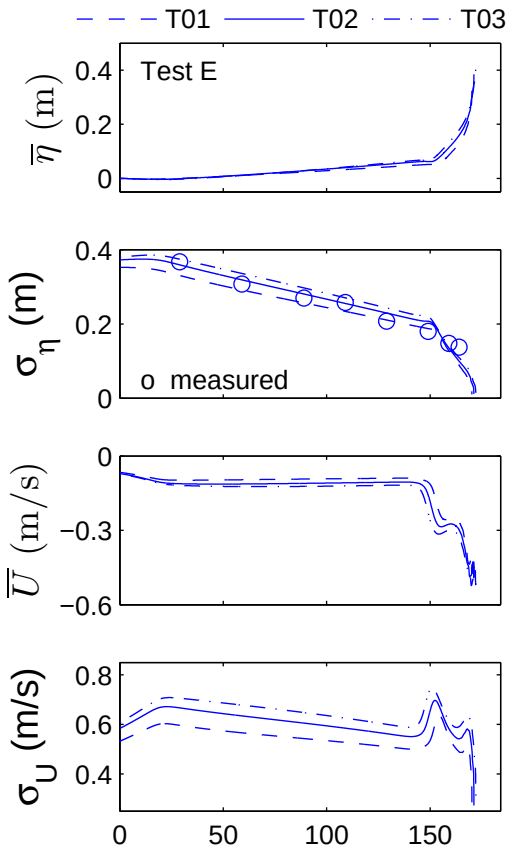

Figure 6.4: Cross-shore variations of $\bar{\eta}$, σ_η, $\bar{U}$ and σ_U at the end of T01, T02 and T03

Chapter 7

EFFECT OF INCIDENT WAVE ANGLE

In the previous two chapters, the numerical model computations for dune and berm erosion were discussed in comparison with the small and large-scale experiments under normally incident waves, $\theta = 0°$. In reality, waves approach a beach from various angles. Therefore, it is worthwhile to analyze the effects of waves arriving at an oblique incident angle to the shoreline. In this chapter, both the small and large-scale experiments were investigated for the incident wave angles of $\theta = 15°$, $30°$ and $45°$ at $x = 0$. In the laboratory, this experiment could be conducted only in a wave basin. But, in a wave basin it can be challenging to prevent alongshore variations in dune and berm erosion as experienced by Payo et al. (2006).

The eroded area, A_e, for the obliquely incident waves in the small-scale experiments was calculated as it was for normally incident waves. The eroded area for obliquely incident waves was normalized by the eroded area for normally incident waves at the same time level, denoted A_0, and represented as a ratio of A_e/A_0 in the Figure 7.1 and Table 7.1. For both experiments H and L, the computed A_e was larger than A_0 for $\theta = 15°$ and $30°$ and smaller than A_0 for $\theta = 45°$. This trend remains constant throughout all time levels. It was apparent that berm geometry affected the ratio A_e/A_0 as experiment H showed a noticeable deviation from unity over experiment L for $\theta = 15°$ and $\theta = 45°$. The berm geometry influenced the irregular breaking wave transformation and wave-induced longshore current. In addition, this deviation between experiment H and L was maximum for time $t = 1$ hr and diminished toward the end of the experiment, $t = 6.11$ hr, as the beach

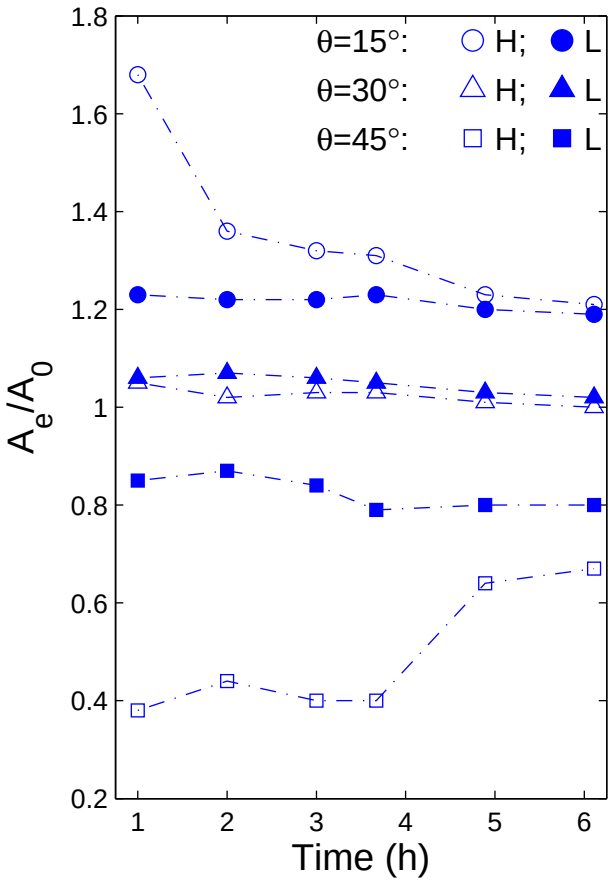

Figure 7.1: Computed A_e/A_0 for $\theta = 10°$, $30°$ and $45°$ for experiments H and L.

Table 7.1: Computed A_e/A_0 for small-scale experiments H and L.

Experiment	t	A_e/A_0			
	(hr)	$\theta = 0°$	$\theta = 15°$	$\theta = 30°$	$\theta = 45°$
Test H	1.00	1.00	1.68	1.05	0.38
	2.00	1.00	1.36	1.02	0.44
	3.00	1.00	1.32	1.03	0.40
	3.67	1.00	1.31	1.03	0.40
	4.89	1.00	1.23	1.01	0.64
	6.11	1.00	1.21	1.00	0.67
Test L	1.00	1.00	1.23	1.06	0.85
	2.00	1.00	1.22	1.07	0.87
	3.00	1.00	1.22	1.06	0.84
	3.67	1.00	1.23	1.05	0.79
	4.89	1.00	1.20	1.03	0.80
	6.11	1.00	1.19	1.02	0.80

profiles became similar.

The ratio A_e/A_0 was calculated for the large-scale experiments as shown in Figure 7.2 and Table 7.2 for times $t = 0.1$ hr to 6 hr. The results for A_e/A_0 remained very similar in all three tests for each incident wave angle. This indicated that there was little coupling between period and incident wave angle effects for these tests. The ratio A_e/A_0 increased as the angle of the incident waves decreased, with the maximum erosion occurring for $\theta = 0°$. The ratio A_e/A_0 was less than unity for all three tests, but decreased as θ increased. In all three tests, the ratio approached a constant as the steepness of the beach slope decreased.

The computed hydrodynamic variables offered insight into the computed eroded area ratio, A_e/A_0. A comparison of the computed variables between $\theta = 0°$ and $\theta = 30°$ are given for each test in the Appendix A, B and C, but only the small-scale tests LD and HD and large-scale tests, T01E, T02E, T03E are shown here for the sake of brevity in Figure 7.3, 7.4 and 7.5. Tests LD and HD corresponded

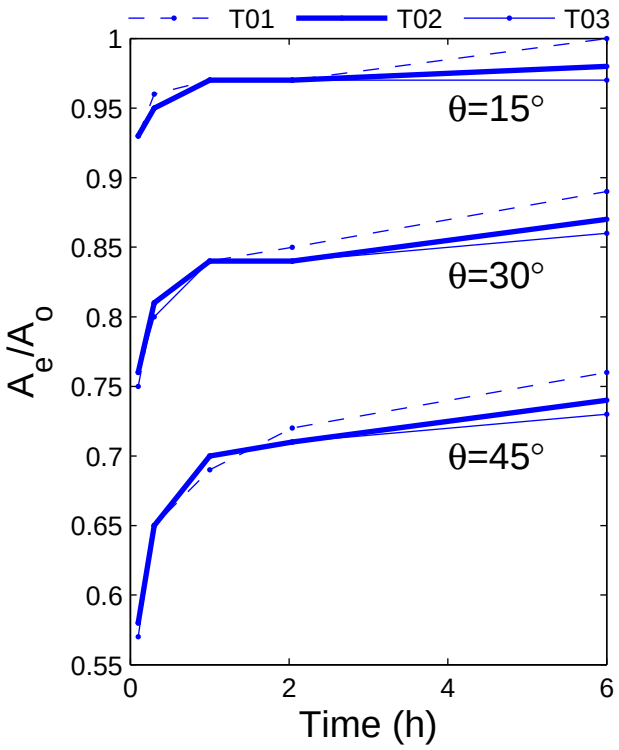

Figure 7.2: Computed A_e/A_0 for three large-scale tests.

Table 7.2: Computed A_e/A_0 for the three large-scale tests.

Test	t	A_e/A_0			
	(hr)	$\theta = 0°$	$\theta = 15°$	$\theta = 30°$	$\theta = 45°$
T01	0.10	1.00	0.93	0.75	0.57
	0.30	1.00	0.96	0.81	0.65
	1.00	1.00	0.97	0.84	0.69
	2.04	1.00	0.97	0.85	0.72
	6.00	1.00	1.00	0.89	0.76
‘ T02	0.10	1.00	0.93	0.76	0.58
	0.30	1.00	0.95	0.81	0.65
	1.00	1.00	0.97	0.84	0.70
	2.04	1.00	0.97	0.84	0.71
	6.00	1.00	0.98	0.87	0.74
T03	0.10	1.00	0.93	0.76	0.58
	0.30	1.00	0.95	0.80	0.65
	1.00	1.00	0.97	0.84	0.70
	2.04	1.00	0.97	0.84	0.71
	6.00	1.00	0.97	0.86	0.73

to the end of the peak storm tide, whereas the large-scale test results came from the end of these tests (E corresponds to t = 6 hr as defined in Table 6.2). It was interesting to note that all of the compared results exhibited similar trends. The only major difference was that the computed values for the large-scale tests T01, T02 and T03 were a larger order of magnitude than for the small-scale experiments H and L. The mean water level, $(S + \bar{\eta})$, the wave height, σ_η, the offshore current, $\bar{U}$, and its corresponding standard deviation, σ_U, all increased with decreasing incident wave angle θ. The longshore current $\bar{V}$ for $\theta = 30^\circ$ was significant on the eroded berm or beach, while it remained zero ($\bar{V} = 0$) for $\theta = 0^\circ$. The probability P_b of sediment movement and the probability P_s of sand suspension turned out to be the same for the fine sand used in all experiments. These probabilities given by Equations (4.19) and (4.20) include the effect of the longshore current and were larger for $\theta = 30^\circ$ than the normally incident waves, $\theta = 0^\circ$. The suspended sediment volume V_s per unit horizontal bottom area given by Equation (4.21) also includes the effect of the longshore current through P_s and the energy dissipation rate D_f due to bottom friction. The computed V_s was larger for $\theta = 30^\circ$ than for the normally incident waves, $\theta = 0^\circ$.

The sediment transport rates were computed using Equations (4.22), (4.23) and (4.24) for tests LD and HD with $\theta = 0^\circ$ and 30° shown in Figure 7.6. The cross-shore bedload transport rate q_{bx} was positive (onshore) while the cross-shore suspended sediment transport rate q_{sx} was negative (offshore). In addition, the cross-shore variation of q_{sx} and q_{bx} was similar for $\theta = 0^\circ$ and $\theta = 30^\circ$. An interesting feature was that q_{bx} for $\theta = 30^\circ$ spikes just before its landward limit while q_{bx} for $\theta = 0^\circ$ approaches zero; this may be attributed to the longshore current $\bar{V}$ for $\theta = 30^\circ$. The net cross-shore sediment transport rate q_x was calculated as the sum of q_{bx} and q_{sx} and was dominated by q_{sx}. Cross-shore sediment transport rates were similar between $\theta = 0^\circ$ and 30° for both experiments. This explains $A_e/A_0 = 1.05$

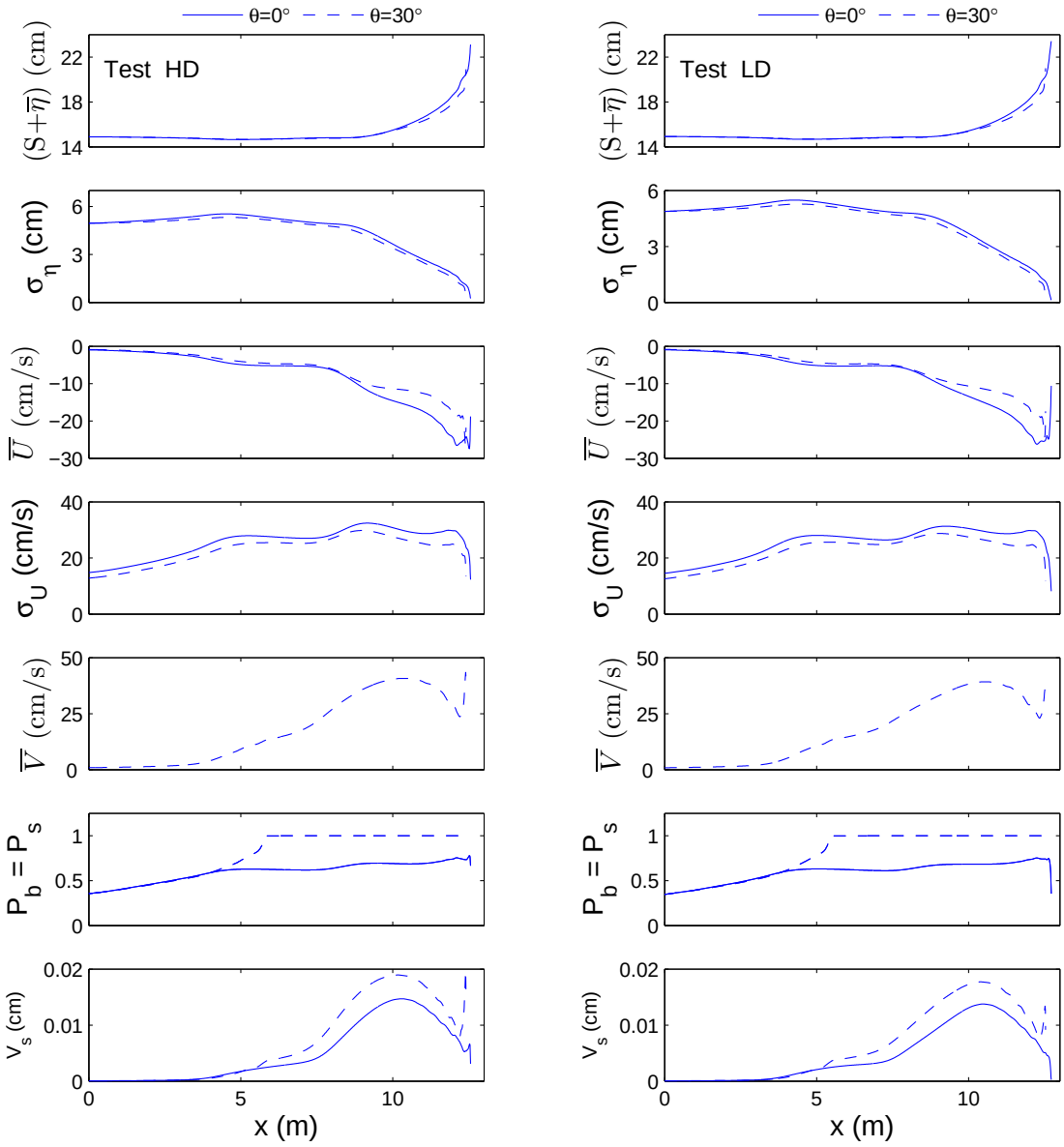

Figure 7.3: Cross-shore variations of $(S + \bar{\eta})$, σ_η, $\bar{U}$, σ_U, $\bar{V}$, $P_b = P_s$ and V_s for $\theta = 0°$ and $\theta = 30°$ for tests HD (left) and LD (right)

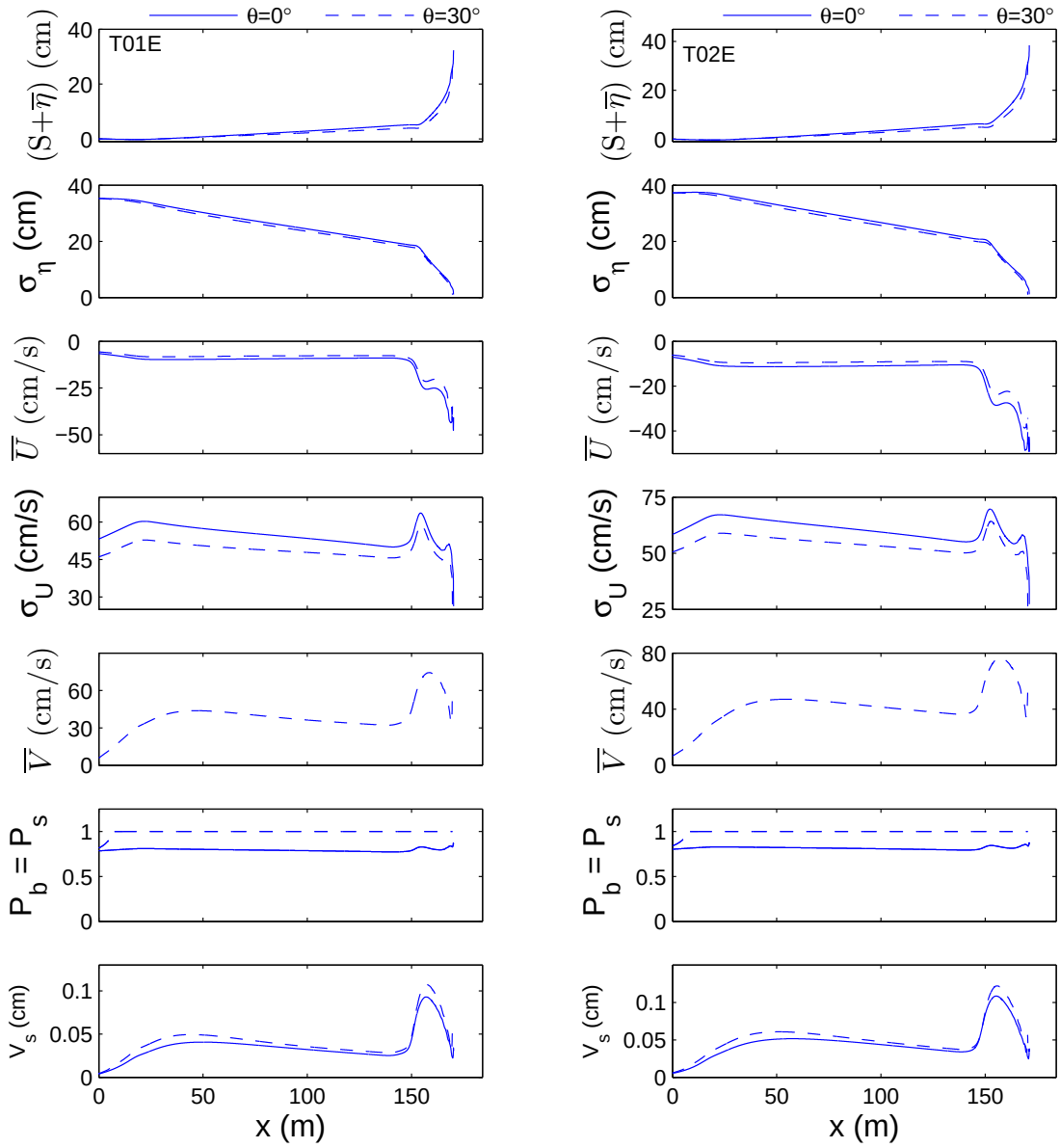

Figure 7.4: Cross-shore variations of $(S + \bar{\eta})$, σ_η, $\bar{U}$, σ_U, $\bar{V}$, $P_b = P_s$ and V_s for $\theta = 0°$ and $\theta = 30°$ for tests T01E (left) and T02E (right)

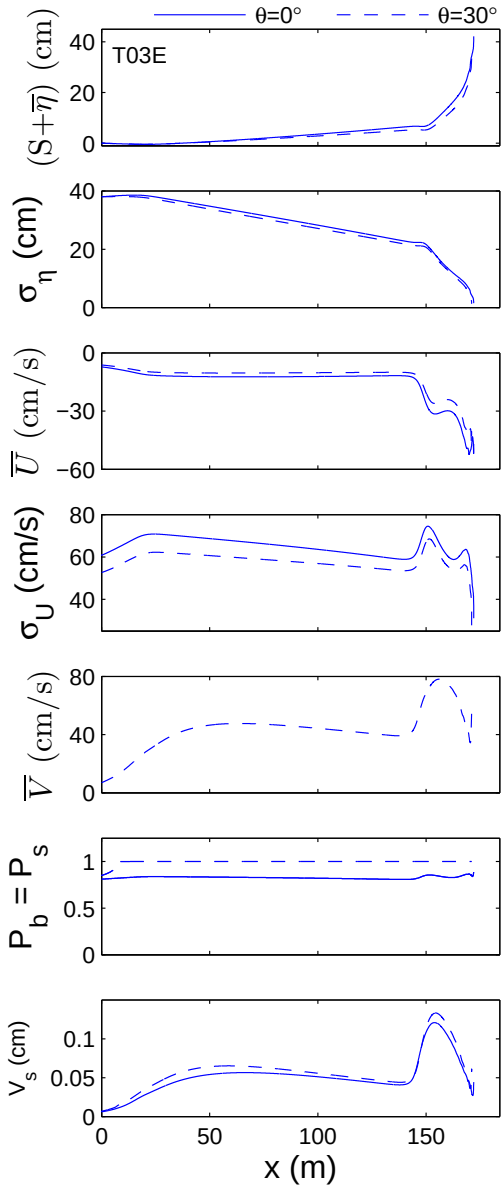

Figure 7.5: Cross-shore variations of $(S + \bar{\eta})$, σ_η, $\bar{U}$, σ_U, $\bar{V}$, $P_b = P_s$ and V_s for $\theta = 0°$ and $\theta = 30°$ for test T03E

for test LD (t = 3.67 hr) and A_e/A_0 = 1.03 for test HD (t = 3.67 hr) for $\theta = 30°$ in Table 7.1. The longshore sediment transport rates, q_{by} and q_{sy}, were of the order of 0.1 and 0.5 cm^2/s, respectively, for $\theta = 30°$. It must be noted that the longshore bedload transport rate, q_{by}, and the longshore suspended sediment transport rate, q_{sy}, were zero for $\theta = 0°$. Interestingly, the longshore sediment transport rate, q_y, was much larger than the cross-shore transport rate, q_x.

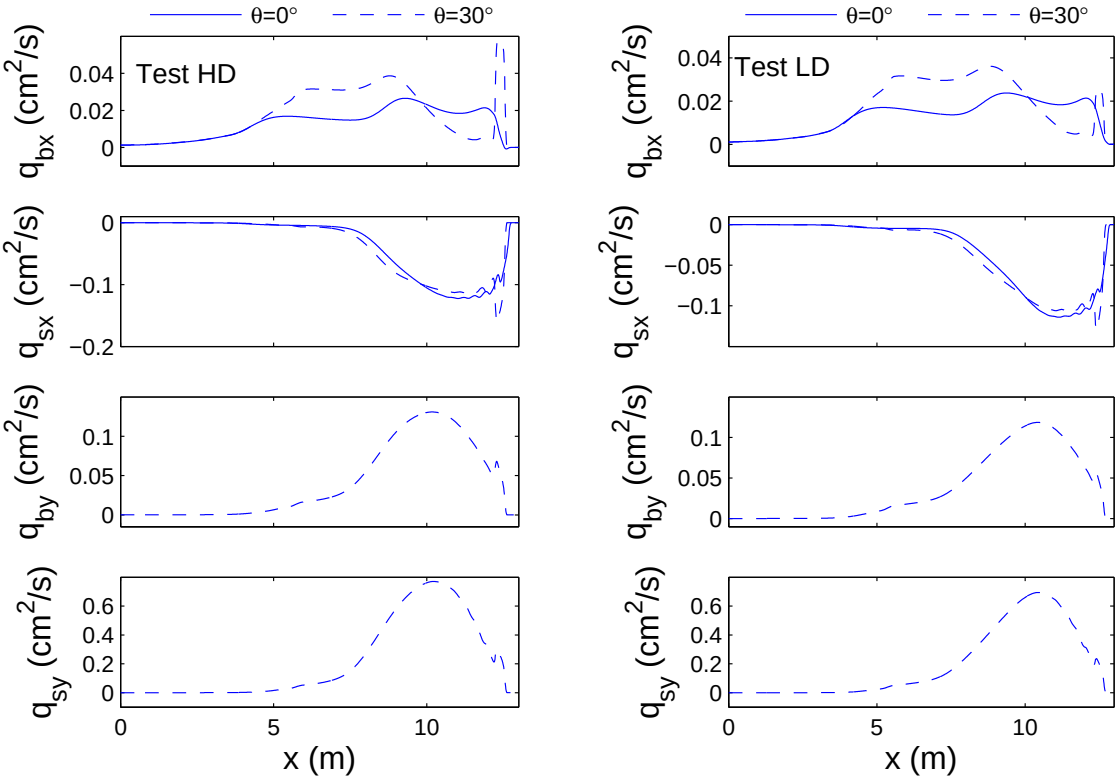

Figure 7.6: Cross-shore variations of q_{bx}, q_{sx}, q_{by} and q_{sy} for $\theta = 0°$ and $\theta = 30°$ for tests HD (left) and LD (right).

For the large-scale tests T01, T02 and T03 the probabilities of sediment movement and suspension and were almost unity as shown in Figures 7.7 and 7.8. For these three tests, the offshore suspended sediment transport rate q_{sx} on the

beach in front of the eroding dune was computed to be larger for $\theta = 0°$, which explained $(A_e/A_0) < 1$ in Table 7.2. The combined cross-shore sediment transport rate, q_x=$(q_{bx} + q_{sx})$, and combined longshore sediment transport rate, q_y=$(q_{by} + q_{sy})$, was dominated by the suspended load term, q_{sx} and q_{sy}, respectively. The total longshore sediment transport, q_y, was significantly larger than the total cross-shore sediment transport rate, q_x. In short, the computed results were consistent regardless of the scale of the experiment. It is noted that the current version of the numerical model may not not have predicted the fairly subtle effect of the incident wave angle accurately.

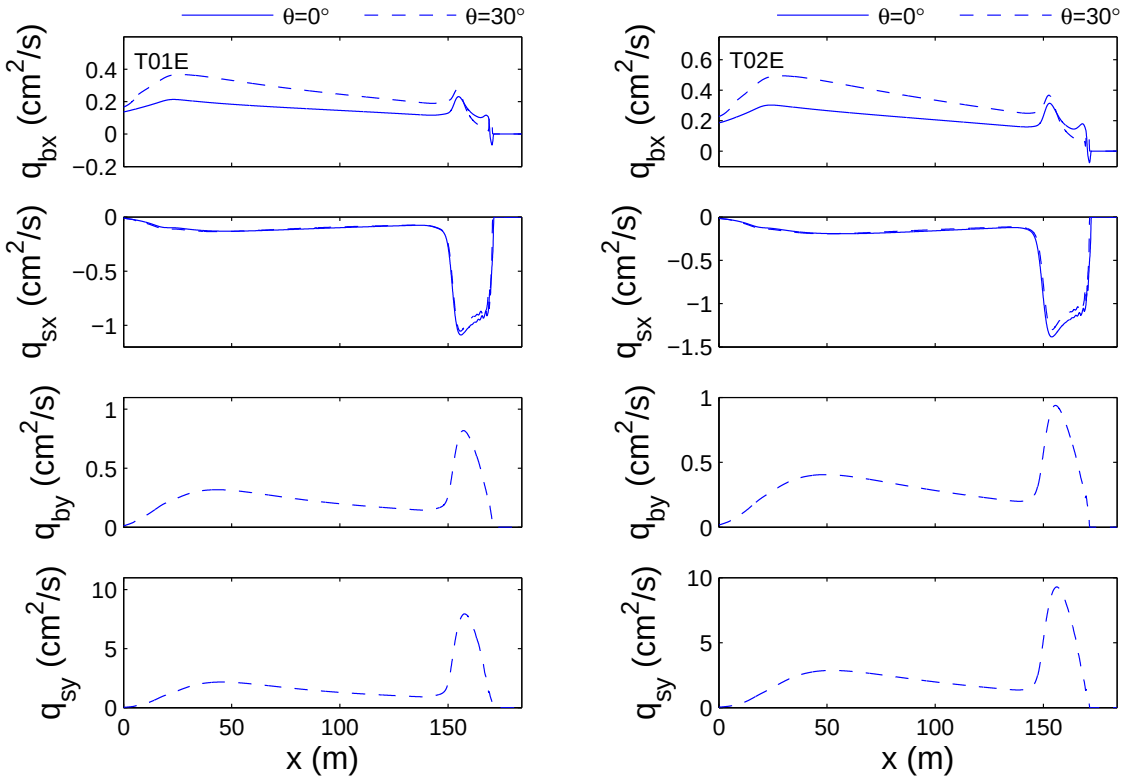

Figure 7.7: Cross-shore variations of q_{bx}, q_{sx}, q_{by} and q_{sy} for $\theta = 0°$ and $\theta = 30°$ for tests T01E and T02E.

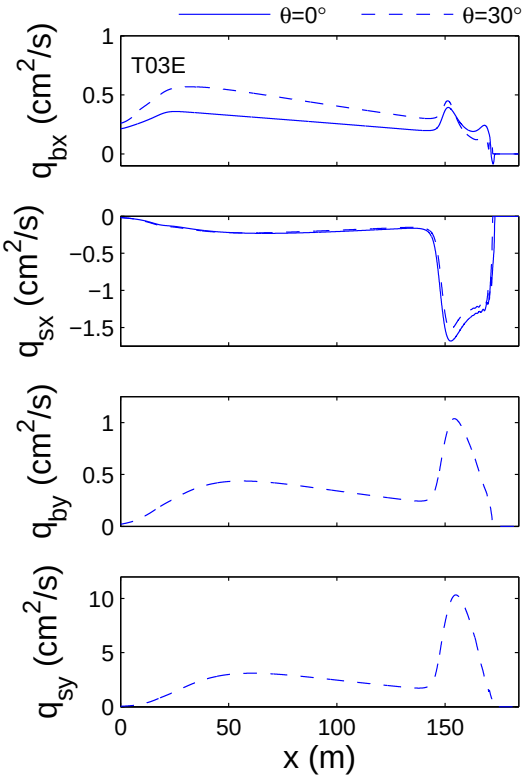

Figure 7.8: Cross-shore variations of q_{bx}, q_{sx}, q_{by} and q_{sy} for $\theta = 0°$ and $\theta = 30°$ for test T03E.

Chapter 8

CONCLUSIONS

This study was performed to investigate how berm and dune geometry influences their subsequent time-dependent erosion during a storm. A storm was simulated by raising the still water level incrementally to simulate storm tide, S, above the datum, $z = 0$, until dune breaching was initiated. Beach recovery was induced by lowering the still water level incrementally until it reached the original datum with no storm tide. Some accretion did occur in backshore region for the recovery phase, though erosion continued on the foreshore. The berm geometry was important for the initial erosion, but the berm had completely eroded by test HC and LC leaving two very similar profiles. The dune breaching occurred at seemingly random locations for the different berm geometries, indicating that slight alongshore variations may have influenced the breaching.

The combined wave and current model by Kobayashi et al. (2007b) was successfully coupled with the proposed sediment transport model. The experimental data was then used to evaluate the hydrodynamic and sediment transport variables predicted by the numerical model. The simple sediment transport formulas produced acceptable agreement (a factor of 2 error margin) with the experiments. This was achieved empirically by calibrating the suspended load parameter, a, as $a = [0.2 + (S_b/\tan\phi)^{0.5}]$ for $S_b > 0$ and $a = 0.2$ for $S_b < 0$ since better agreement was reached in the beach region of relatively steep slope S_b for values of a greater than 0.2. However, the model overpredicted dune erosion in the small-scale experiments

and overpredicted the corresponding accretion below the datum, $z = 0$. The model behaved somewhat differently for the large-scale experiments conducted by van Gent et al. (2006), as dune erosion and accretion below the datum $z = 0$ was underpredicted. This difference may be due to a combination of scale difference and dune geometry. It was noted in Chapter 2 that the sand could not be scaled down enough to preserve sediment similitude for the small-scale experiments, therefore the sand acted more as a coarse grain. However, the present numerical model accounts for the different sediment characteristics under different wave characteristics. The numerical model also helped verify the the relationship between increasing dune erosion with increasing wave period as van Gent et al. (2006) measured.

Computations were performed with the verified model for obliquely incident waves of $\theta = 15°$, $30°$ and $45°$. For the small-scale experiments, the eroded area was greater for $\theta = 15°$ and $30°$ than for normally incident waves, $\theta = 0°$. Conversely, the large scale experiments indicated that the eroded area decreased with increasing angle of incidence, θ. Beach and dune geometry played a role in this difference. In addition, the probability P_b of sediment movement and the probability P_s of sand suspension were identical, meaning that all the mobilized sand was being suspended. For the fine sands used in these experiments the cross-shore sediment transport rate was dominated by the suspended load term, q_{sx}. In addition, the long-shore sediment rate, q_y, dominated the cross-shore sediment transport rate, q_x, in all experiments. Also, it was shown that the effects of the wave period and incident angle were independent of each other for the large scale dune erosion tests.

The numerical model proved to be useful for analyzing the relationship among berm and dune geometry, incident angle, wave period, and erosion, but more data sets are required to verify the model results. Both the large and small-scale data sets used here were conducted with a fine and uniform sand, $d_{50} = 0.18$ and 0.20 mm, and additional data with coarse sand would be helpful. Data for large-scale berm

and dune erosion under oblique waves is also necessary to validate the proposed sediment transport formulas. In addition, dune overwash and breaching are two critical processes found in the field that need to be incorporated into the model (Donnelly et al. 2006).

REFERENCES

Bagnold, R.A. (1966). "An approach to the sediment transport problem from general physics." U.S. Geol. Surv., Prof. Paper, 422-I.

Bailard, J.A. (1981). "An energetics total load sediment transport model for a plane sloping beach." *J. Geophys. Res.*, 86(C11), 10,938-10,954.

Battjes, J.A., and Stive, M.J.F. (1985). "Calibration and verification of a dissipation model for random breaking waves." *J. Geophys. Res.*, 90(C5), 9159-9167.

Coastal Engineering Manual. (2003). Part V, U.S. Army Engineer Research and Development Center, Vicksburg, Miss.

Dean, R.G., and Dalrymple, R.A. (1984). *Water Wave Mechanics for Engineers and Scientists*. World Scientific, Singapore.

Dohmen-Janssen, C.M., and Hanes, D.H. (2002). "Sheet flow dynamics under monochromatic nonbreaking waves." *J. Geophys. Res.*, 107(C10), 3149.

Donnelly, C., Kraus, N., and Larson, M. (2006). "State of knowledge on measurement and modeling of coastal overwash." *J. Coastal Res.*, 22(4), 965-991.

Feddersen, F., Guza, R.T., Elgar, S., and Herbers, T.H.C. (2000). "Velocity moments in alongshore bottom stress parameterization." *J. Geophys. Res.*, 105(C4), 8673-8686.

Kobayashi, N. (1987). "Analytical solution for dune erosion by storms." *J. Waterway, Port, Coastal, Ocean Eng.*, 113(4), 401-418.

Kobayashi, N., Agarwal, A., and Johnson, B.D. (2007b). "Longshore current and sediment transport on beaches." *J. Waterway, Port, Coastal, Ocean Eng.*, 133(4), 296-306.

Kobayashi, N., Buck, M., Payo, A., and Johnson, B.D. (2007). "Berm and dune erosion during a storm." *J. Waterway, Port, Coastal, Ocean Eng.*, (submitted).

Kobayashi, N., Cox, D. T., and Wurjanto, A. (1990). "Irregular wave reflection and run-up on rough impermeable slopes." *J. Waterway Port Coastal Ocean Eng.*, 128, 238-248.

Kobayashi, N., and Johnson, B.D. (2001). "Sand suspension, storage, advection, and settling in surf and swash zones." *J. Geophys. Res.*, 106(C5), 9363-9376.

Kobayashi, N., Payo, A., and Johnson, B.D. (2008). "Suspended sand and bedload transport on beaches." Handbook of Coastal and Ocean Engineering, World Scientific, Singapore (will be published).

Kobayashi, N., Payo, A., and Schmied, L.D. (2007a). "Cross-shore suspended sand and bedload transport on beaches." *J. Geophys. Res.*, (submitted).

Kobayashi, N., Tega, Y., and Hancock, M.W. (1996). "Wave reflection and overwash of dunes." *J. Waterway, Port, Coastal, Ocean Eng.*, 122(3), 150-153.

Kobayashi, N., Zhao, H., and Tega, Y. (2005). "Suspended sand transport in surf zones." *J. Geophys. Res.*, 110, C12009.

Kriebel, D.L., and Dean, R.G. (1985). "Numerical simulation of time-dependent beach and dune erosion," Coastal Eng., 9, 221-245.

Larson, M., and Kraus, N. (1989). "SBEACH: Numerical model for simulating storm-induced beach change. Report 1 - Empirical foundation and model development." Technical Rep. CACR-89-9, U.S. Army Engineer Research and Development Center, Vicksburg, Miss.

Lawrence, A. and Kobayashi, N. (2003). "Experiments on cross-shore sediment transport under positive and negative solitary waves." Technical Report *Res. Rep.* CACR-03-03, Cent. for Appl. Coastal Res., Univ. of Delaware, Newark, Del.

Madsen, O.S., and Grant, W.D. (1976). "Quantitative description of sediment transport by waves." Coastal Engineering 1976, Proc. 15th Coastal Engineering Conf., ASCE, Reston, Va., 1093-1112.

Nairn, R.B., and Southgate, H.N. (1993). "Deterministic profile modelling of nearshore processes. Part 2. Sediment transport and beach profile development." Coastal Eng., 19, 57-96.

Payo, A., Kobayashi, N., and Kim, K. (2006). "Beach renourishment strategies." Coastal Engineering 2006, Proc. 30th Coastal Engineering Conf., World Scientific, Singapore, 4129-4140.

Reniers, A.J.H.M., and Battjes, J.A. (1997). "A laboratory study of longshore currents over barred and non-barred beaches." *Coastal Eng.*, 30, 1-21.

Ribberink, J.S., and Al-Salem, A.A. (1994). "Sediment transport in oscillatory boundary layers in cases of rippled beds and sheet flow." *J. Geophys. Res.*, 99(C6), 12,707-12,727.

Ruessink, B.G., Miles, J.R., Feddersen, F., Guza, R.T., and Elgar, S. (2001). "Modeling the alongshore current on barred beaches." *J. Geophys. Res.*, 106(C10), 22,451-22,463.

Schmied, L., Kobayashi, N., Puleo, J., and Payo, A. (2006). "Cross-shore suspended sand transport on beaches." Coastal Engineering 2006, Proc. 30th Coastal Engineering Conf., World Scientific, Singapore, 2511-2523.

van Gent, M.R.A., Coeveld, E.M., Walstra, D.J.R., van de Graaff, J., Steetzel, H.J., and Boers, M. (2006). "Dune erosion tests to study the influence of wave periods." Coastal Engineering 2006, Proc. 30th Coastal Engineering Conf., World Scientific, Singapore, 2779-2791.

Appendix A

EXPERIMENT H

Table A.1: Free surface measurements for bursts HA1 to HA8 where NR = not reliable in this and subsequent tables.

Test	x (m)	z_b (cm)	$\overline{\eta}+S$ (cm)	σ_η (cm)
	0.00	-75.50	-0.25	4.71
	0.34	-72.13	-0.21	4.77
	0.89	-65.15	-0.23	4.88
HA1	4.95	-19.09	-0.43	4.65
	7.55	-17.37	0.70	3.33
	8.90	-15.84	0.71	3.47
	10.00	-5.20	0.83	2.89
	11.10	19.80	NR	NR
	0.00	-75.50	-0.19	4.65
	0.34	-72.06	-0.20	4.68
	0.89	-65.05	-0.20	4.84
HA2	4.95	-19.37	-0.33	4.46
	7.55	-17.53	0.63	3.34
	8.90	-15.90	0.70	3.34
	10.00	-5.11	0.86	2.76
	11.10	19.25	NR	NR
	0.00	-75.50	-0.24	4.62
	0.34	-71.98	-0.22	4.67
	0.89	-64.96	-0.20	4.84
HA3	4.95	-19.66	-0.12	4.32
	7.55	-17.69	0.61	3.31
	8.90	-15.97	0.73	3.33
	10.00	-5.03	0.83	2.74
	11.10	18.70	NR	NR
	0.00	-75.50	-0.19	4.61
	0.34	-71.91	-0.20	4.66
	0.89	-64.87	-0.20	4.85
HA4	4.95	-19.94	-0.25	4.31
	7.55	-17.86	0.60	3.34
	8.90	-16.04	0.56	3.32
	10.00	-4.94	0.80	2.75
	11.10	18.15	NR	NR

Test	x (m)	z_b (cm)	$\overline{\eta}+S$ (cm)	σ_η (cm)
	0.00	-75.50	-0.19	4.60
	0.34	-71.83	-0.19	4.66
	0.89	-64.77	-0.20	4.84
HA5	4.95	-20.23	-0.19	4.29
	7.55	-18.02	0.63	3.32
	8.90	-16.11	0.71	3.33
	10.00	-4.85	0.83	2.73
	11.10	17.60	17.60	0.65
	0.00	-75.50	-0.18	4.61
	0.34	-71.75	-0.20	4.66
	0.89	-64.68	-0.19	4.85
HA6	4.95	-20.52	-0.11	4.25
	7.55	-18.19	0.59	3.33
	8.90	-16.18	0.68	3.31
	10.00	-4.76	0.81	2.74
	11.10	17.05	17.05	0.64
	0.00	-75.50	-0.18	4.59
	0.34	-71.68	-0.19	4.64
	0.89	-64.58	-0.19	4.85
HA7	4.95	-20.80	-0.15	4.19
	7.55	-18.35	0.62	3.29
	8.90	-16.25	0.67	3.32
	10.00	-4.68	0.82	2.69
	11.10	16.50	16.50	0.56
	0.00	-75.50	-0.19	4.57
	0.34	-71.60	-0.19	4.63
	0.89	-64.49	-0.20	4.84
HA8	4.95	-21.09	-0.19	4.17
	7.55	-18.52	0.62	3.30
	8.90	-16.32	0.67	3.31
	10.00	-4.59	0.82	2.68
	11.10	15.95	15.95	0.56

Table A.2: Free surface measurements for burst HA9 and the average over all the bursts.

Test	x (m)	z_b (cm)	$\overline{\eta}+S$ (cm)	σ_η (cm)
	0.00	-75.50	-0.18	4.59
	0.34	-71.53	-0.18	4.65
	0.89	-64.40	-0.18	4.85
HA9	4.95	-21.37	-0.08	4.17
	7.55	-18.68	0.62	3.28
	8.90	-16.39	0.65	3.32
	10.00	-4.50	0.84	2.69
	11.10	15.40	15.40	0.53

Test	x (m)	z_b (cm)	$\overline{\eta}+S$ (cm)	σ_η (cm)
	0.00	-75.50	-0.20	4.62
	0.34	-71.83	-0.20	4.67
	0.89	-64.77	-0.20	4.85
Avg.	4.95	-20.23	-0.21	4.31
	7.55	-18.02	0.62	3.32
	8.90	-16.11	0.67	3.34
	10.00	-4.85	0.83	2.74
	11.10	17.60	16.50	0.59

Table A.3: Free surface measurements for bursts HB1 to HB8.

Test	x (m)	z_b (cm)	$\overline{\eta}+S$ (cm)	σ_η (cm)
HB1	0.00	-75.50	4.83	4.67
	0.34	-71.53	4.81	4.72
	0.89	-64.40	4.81	4.93
	4.95	-21.37	4.64	4.67
	7.55	-18.68	5.38	3.79
	8.90	-16.39	NR	NR
	10.00	-4.50	NR	NR
	11.10	15.40	NR	NR
HB2	0.00	-75.56	4.88	4.72
	0.34	-71.60	4.86	4.71
	0.89	-64.49	4.84	4.91
	4.95	-21.24	4.64	4.75
	7.55	-18.63	5.40	3.69
	8.90	-16.13	NR	NR
	10.00	-4.23	5.54	3.06
	11.10	14.48	14.98	1.29
HB3	0.00	-75.62	4.87	4.70
	0.34	-71.67	4.86	4.69
	0.89	-64.58	4.85	4.85
	4.95	-21.11	4.64	4.81
	7.55	-18.59	5.38	3.67
	8.90	-15.87	NR	NR
	10.00	-3.95	5.66	3.05
	11.10	13.55	14.41	1.42
HB4	0.00	-75.67	4.88	4.71
	0.34	-71.75	4.86	4.69
	0.89	-64.67	4.84	4.81
	4.95	-20.98	4.66	4.90
	7.55	-18.54	5.36	3.65
	8.90	-15.61	NR	NR
	10.00	-3.68	5.74	3.02
	11.10	12.63	13.73	1.57

Test	x (m)	z_b (cm)	$\overline{\eta}+S$ (cm)	σ_η (cm)
HB5	0.00	-75.73	4.88	4.70
	0.34	-71.82	4.85	4.68
	0.89	-64.76	4.85	4.79
	4.95	-20.84	4.63	4.93
	7.55	-18.49	5.37	3.66
	8.90	-15.35	NR	NR
	10.00	-3.40	5.65	3.00
	11.10	11.70	13.42	1.61
HB6	0.00	-75.79	4.89	4.71
	0.34	-71.89	4.87	4.69
	0.89	-64.85	4.85	4.78
	4.95	-20.71	4.61	4.97
	7.55	-18.45	5.36	3.61
	8.90	-15.09	NR	NR
	10.00	-3.13	5.68	2.99
	11.10	10.78	12.54	1.66
HB7	0.00	-75.85	4.88	4.71
	0.34	-71.96	4.87	4.69
	0.89	-64.94	4.85	4.78
	4.95	-20.58	4.65	4.96
	7.55	-18.40	5.34	3.61
	8.90	-14.83	NR	NR
	10.00	-2.85	5.79	3.01
	11.10	9.85	11.65	1.69
HB8	0.00	-75.90	4.88	4.72
	0.34	-72.04	4.87	4.69
	0.89	-65.04	4.86	4.77
	4.95	-20.45	4.64	5.00
	7.55	-18.36	5.36	3.62
	8.90	-14.57	NR	NR
	10.00	-2.58	5.81	2.98
	11.10	8.93	10.73	1.69

Table A.4: Free surface measurements for burst HB9 and the average over all the bursts.

Test	x (m)	z_b (cm)	$\overline{\eta} + S$ (cm)	σ_η (cm)
HB9	0.00	-75.96	4.88	4.71
	0.34	-72.11	4.87	4.69
	0.89	-65.13	4.83	4.77
	4.95	-20.32	4.61	4.99
	7.55	-18.31	5.36	3.64
	8.90	-14.31	NR	NR
	10.00	-2.30	5.79	2.99
	11.10	8.00	9.74	1.69

Test	x (m)	z_b (cm)	$\overline{\eta} + S$ (cm)	σ_η (cm)
Avg.	0.00	-75.73	4.87	4.71
	0.34	-71.82	4.86	4.69
	0.89	-64.76	4.84	4.82
	4.95	-20.84	4.64	4.89
	7.55	-18.49	5.37	3.66
	8.90	-15.35	NR	NR
	10.00	-3.40	5.71	3.01
	11.10	11.70	12.65	1.58

Table A.5: Free surface measurements for bursts HC1 to HC8.

Test	x (m)	z_b (cm)	$\overline{\eta}+S$ (cm)	σ_η (cm)
HC1	0.00	-75.96	9.85	4.63
	0.34	-72.11	9.85	4.66
	0.89	-65.13	9.84	4.72
	4.95	-20.32	9.72	5.03
	7.55	-18.31	10.14	3.95
	8.90	-14.31	NR	NR
	10.00	-2.30	10.16	3.52
	11.10	8.00	11.49	2.54
HC2	0.00	-76.02	9.87	4.65
	0.34	-72.18	9.86	4.67
	0.89	-65.22	9.87	4.72
	4.95	-20.36	9.76	5.02
	7.55	-18.19	10.16	3.98
	8.90	-14.18	NR	NR
	10.00	-2.02	10.08	3.45
	11.10	7.50	11.34	2.58
HC3	0.00	-76.08	9.91	4.64
	0.34	-72.25	9.89	4.66
	0.89	-65.31	9.88	4.71
	4.95	-20.41	9.79	5.02
	7.55	-18.08	10.14	3.94
	8.90	-14.05	NR	NR
	10.00	-1.74	10.40	3.41
	11.10	7.00	11.18	2.65
HC4	0.00	-76.13	9.91	4.64
	0.34	-72.33	9.89	4.66
	0.89	-65.40	9.88	4.71
	4.95	-20.45	9.78	5.02
	7.55	-17.96	10.15	3.99
	8.90	-13.93	NR	NR
	10.00	-1.46	10.47	3.40
	11.10	6.50	11.13	2.66

Test	x (m)	z_b (cm)	$\overline{\eta}+S$ (cm)	σ_η (cm)
HC5	0.00	-76.19	9.92	4.63
	0.34	-72.40	9.89	4.65
	0.89	-65.49	9.89	4.70
	4.95	-20.50	9.77	5.00
	7.55	-17.84	10.14	4.00
	8.90	-13.80	NR	NR
	10.00	-1.19	10.58	3.42
	11.10	6.00	11.15	2.66
HC6	0.00	-76.25	9.88	4.64
	0.34	-72.47	9.90	4.65
	0.89	-65.58	9.89	4.70
	4.95	-20.54	9.80	5.00
	7.55	-17.73	10.15	3.95
	8.90	-13.68	NR	NR
	10.00	-0.91	10.61	3.38
	11.10	5.83	11.10	2.66
HC7	0.00	-76.31	9.91	4.62
	0.34	-72.54	9.90	4.65
	0.89	-65.67	9.89	4.69
	4.95	-20.59	9.79	4.98
	7.55	-17.61	10.14	3.96
	8.90	-13.55	NR	NR
	10.00	-0.63	10.73	3.37
	11.10	5.83	11.10	2.67
HC8	0.00	-76.36	9.93	4.62
	0.34	-72.62	9.89	4.64
	0.89	-65.76	9.89	4.69
	4.95	-20.63	9.79	4.97
	7.55	-17.49	10.15	3.93
	8.90	-13.43	NR	NR
	10.00	-0.35	10.71	3.39
	11.10	5.83	11.11	2.68

Table A.6: Free surface measurements for burst HC9 and the average over all the bursts.

Test	x (m)	z_b (cm)	$\overline{\eta} + S$ (cm)	σ_η (cm)
HC9	0.00	-76.42	9.91	4.62
	0.34	-72.69	9.90	4.64
	0.89	-65.86	9.89	4.69
	4.95	-20.68	9.77	4.96
	7.55	-17.38	10.14	3.93
	8.90	-13.30	NR	NR
	10.00	-0.07	10.86	3.40
	11.10	5.83	11.00	2.65

Test	x (m)	z_b (cm)	$\overline{\eta} + S$ (cm)	σ_η (cm)
Avg.	0.00	-76.19	9.90	4.63
	0.34	-72.40	9.89	4.65
	0.89	-65.49	9.88	4.70
	4.95	-20.50	9.78	5.00
	7.55	-17.84	10.15	3.96
	8.90	-13.80	NR	NR
	10.00	-1.19	10.51	3.41
	11.10	6.48	11.18	2.64

Table A.7: Free surface measurements for bursts HD1 to HD6, including the average over all the bursts.

Test	x (m)	z_b (cm)	$\overline{\eta}+S$ (cm)	σ_η (cm)
	0.00	-76.42	14.86	5.04
	0.34	-72.69	14.85	5.08
	0.89	-65.86	14.87	5.04
HD1	4.95	-20.68	14.76	5.21
	7.55	-17.38	15.19	4.46
	8.90	-13.30	15.16	4.30
	10.00	-0.07	14.82	4.06
	11.10	5.83	15.56	3.22
	0.00	-76.25	14.92	4.98
	0.34	-72.73	14.90	5.04
	0.89	-65.66	14.89	5.05
HD2	4.95	-20.79	14.75	5.19
	7.55	-17.19	15.18	4.53
	8.90	-13.34	15.16	4.29
	10.00	0.36	14.91	3.93
	11.10	5.90	15.80	3.34
	0.00	-76.09	14.92	4.95
	0.34	-72.76	14.89	4.99
	0.89	-65.46	14.88	5.01
HD3	4.95	-20.90	14.78	5.19
	7.55	-17.00	15.14	4.52
	8.90	-13.39	15.11	4.27
	10.00	0.80	15.04	3.93
	11.10	5.90	15.89	3.26
	0.00	-75.92	14.94	4.92
	0.34	-72.80	14.90	4.95
	0.89	-65.26	14.90	4.97
HD4	4.95	-21.02	14.79	5.16
	7.55	-16.82	15.14	4.52
	8.90	-13.43	15.05	4.19
	10.00	1.23	15.06	3.85
	11.10	5.90	15.94	3.27

Test	x (m)	z_b (cm)	$\overline{\eta}+S$ (cm)	σ_η (cm)
	0.00	-75.76	14.94	4.90
	0.34	-72.84	14.91	4.93
	0.89	-65.07	14.88	4.95
HD5	4.95	-21.13	14.79	5.15
	7.55	-16.63	15.15	4.53
	8.90	-13.48	15.09	4.18
	10.00	1.67	15.21	3.79
	11.10	5.90	16.00	3.18
	0.00	-75.59	14.81	4.93
	0.34	-72.87	14.79	4.95
	0.89	-64.87	14.83	4.99
HD6	4.95	-21.24	14.65	5.17
	7.55	-16.45	15.19	4.52
	8.90	-13.52	15.12	4.23
	10.00	2.10	15.22	3.82
	11.10	5.90	15.93	3.23
	0.00	-76.01	14.90	4.95
	0.34	-72.78	14.87	4.99
	0.89	-65.36	14.88	5.00
Avg	4.95	-20.96	14.75	5.18
	7.55	-16.91	15.17	4.51
	8.90	-13.41	15.12	4.24
	10.00	1.02	15.05	3.90
	11.10	5.89	15.85	3.25

Table A.8: Free surface measurements for bursts HE1 to HE8.

Test	x (m)	z_b (cm)	$\overline{\eta}+S$ (cm)	σ_η (cm)
HE1	0.00	-75.59	4.70	4.69
	0.34	-72.87	4.71	4.72
	0.89	-64.87	4.76	4.71
	4.95	-21.24	4.66	4.98
	7.55	-16.45	5.48	3.48
	8.90	-13.52	5.57	3.27
	10.00	2.10	6.14	2.48
	11.10	5.90	8.77	1.64
HE2	0.00	-75.51	4.82	4.74
	0.34	-72.78	4.80	4.78
	0.89	-64.95	4.81	4.78
	4.95	-21.01	4.72	5.07
	7.55	-16.52	5.52	3.50
	8.90	-13.49	5.58	3.29
	10.00	-1.40	6.02	2.61
	11.10	7.10	8.72	1.55
HE3	0.00	-75.42	4.84	4.73
	0.34	-72.68	4.83	4.77
	0.89	-65.04	4.83	4.77
	4.95	-20.79	4.75	5.11
	7.55	-16.59	5.48	3.50
	8.90	-13.45	5.61	3.35
	10.00	-1.90	5.98	2.71
	11.10	7.10	8.85	1.56
HE4	0.00	-75.34	4.84	4.73
	0.34	-72.58	4.83	4.75
	0.89	-65.12	4.83	4.75
	4.95	-20.56	4.71	5.12
	7.55	-16.66	5.49	3.49
	8.90	-13.42	5.59	3.31
	10.00	-2.15	5.92	2.72
	11.10	7.10	8.73	1.60

Test	x (m)	z_b (cm)	$\overline{\eta}+S$ (cm)	σ_η (cm)
HE5	0.00	-75.25	4.85	4.71
	0.34	-72.49	4.83	4.73
	0.89	-65.21	4.84	4.73
	4.95	-20.33	4.68	5.11
	7.55	-16.74	5.48	3.49
	8.90	-13.39	5.59	3.30
	10.00	-2.40	5.87	2.77
	11.10	7.10	8.85	1.60
HE6	0.00	-75.17	4.85	4.72
	0.34	-72.39	4.83	4.73
	0.89	-65.29	4.84	4.72
	4.95	-20.10	4.71	5.11
	7.55	-16.81	5.49	3.50
	8.90	-13.36	5.57	3.27
	10.00	-2.70	5.82	2.82
	11.10	7.10	8.82	1.58
HE7	0.00	-75.09	4.87	4.71
	0.34	-72.29	4.85	4.72
	0.89	-65.37	4.84	4.70
	4.95	-19.88	4.69	5.11
	7.55	-16.88	5.49	3.51
	8.90	-13.32	5.57	3.29
	10.00	-2.90	5.76	2.88
	11.10	7.10	8.90	1.55
HE8	0.00	-75.00	4.86	4.71
	0.34	-72.20	4.83	4.71
	0.89	-65.46	4.84	4.70
	4.95	-19.65	4.69	5.08
	7.55	-16.95	5.46	3.46
	8.90	-13.29	5.60	3.29
	10.00	-3.00	5.72	2.87
	11.10	7.10	8.81	1.54

Table A.9: Free surface measurements for bursts HE9 to HE11, including the average over all the bursts.

Test	x (m)	z_b (cm)	$\overline{\eta} + S$ (cm)	σ_η (cm)
HE9	0.00	-74.92	4.86	4.72
	0.34	-72.10	4.83	4.73
	0.89	-65.54	4.84	4.73
	4.95	-19.42	4.65	5.07
	7.55	-17.02	5.48	3.48
	8.90	-13.26	5.57	3.25
	10.00	-3.00	5.68	2.87
	11.10	7.10	8.86	1.53
HE10	0.00	-74.83	4.86	4.71
	0.34	-72.00	4.84	4.73
	0.89	-65.62	4.84	4.72
	4.95	-19.19	4.68	5.07
	7.55	-17.09	5.46	3.46
	8.90	-13.22	5.57	3.27
	10.00	-3.00	5.69	2.86
	11.10	7.10	8.84	1.51
HE11	0.00	-74.75	4.86	4.70
	0.34	-71.91	4.86	4.72
	0.89	-65.71	4.85	4.71
	4.95	-18.96	4.70	5.07
	7.55	-17.17	5.46	3.44
	8.90	-13.19	5.58	3.27
	10.00	-3.00	5.61	2.90
	11.10	7.10	8.80	1.47
Avg.	0.00	-75.22	4.84	4.71
	0.34	-72.44	4.82	4.74
	0.89	-65.24	4.83	4.73
	4.95	-20.23	4.69	5.08
	7.55	-16.77	5.48	3.48
	8.90	-13.37	5.58	3.29
	10.00	-1.96	5.84	2.77
	11.10	6.97	8.81	1.56

Table A.10: Free surface measurements for bursts HF1 to HF8.

Test	x (m)	z_b (cm)	$\overline{\eta}+S$ (cm)	σ_η (cm)
HF1	0.00	-74.75	-0.28	4.46
	0.34	-71.91	-0.29	4.51
	0.89	-65.71	-0.24	4.51
	4.95	-18.96	-0.30	4.42
	7.55	-17.17	0.83	2.87
	8.90	-13.19	0.97	2.69
	10.00	-3.00	1.67	2.20
	11.10	7.10	7.89	0.63
HF2	0.00	-74.80	-0.21	4.44
	0.34	-71.88	-0.24	4.47
	0.89	-65.63	-0.22	4.52
	4.95	-19.10	-0.16	4.21
	7.55	-17.14	0.80	2.86
	8.90	-13.24	0.94	2.66
	10.00	-2.70	1.63	2.16
	11.10	7.70	8.06	0.63
HF3	0.00	-74.84	-0.20	4.40
	0.34	-71.86	-0.23	4.44
	0.89	-65.55	-0.21	4.52
	4.95	-19.23	-0.23	4.14
	7.55	-17.11	0.78	2.85
	8.90	-13.28	0.93	2.65
	10.00	-2.70	1.63	2.17
	11.10	7.70	8.04	0.64
HF4	0.00	-74.89	-0.18	4.38
	0.34	-71.83	-0.22	4.42
	0.89	-65.48	-0.19	4.50
	4.95	-19.37	-0.19	4.08
	7.55	-17.08	0.77	2.86
	8.90	-13.33	0.92	2.63
	10.00	-2.70	1.63	2.14
	11.10	7.70	8.05	0.63

Test	x (m)	z_b (cm)	$\overline{\eta}+S$ (cm)	σ_η (cm)
HF5	0.00	-74.94	-0.17	4.37
	0.34	-71.81	-0.20	4.42
	0.89	-65.40	-0.19	4.49
	4.95	-19.50	-0.14	4.07
	7.55	-17.05	0.76	2.87
	8.90	-13.37	0.90	2.63
	10.00	-2.70	1.63	2.11
	11.10	7.70	8.07	0.64
HF6	0.00	-74.99	-0.17	4.38
	0.34	-71.78	-0.21	4.43
	0.89	-65.32	-0.18	4.51
	4.95	-19.64	-0.14	4.04
	7.55	-17.02	0.76	2.86
	8.90	-13.42	0.90	2.63
	10.00	-2.70	1.62	2.14
	11.10	7.70	8.03	0.64
HF7	0.00	-75.03	-0.16	4.38
	0.34	-71.76	-0.21	4.42
	0.89	-65.24	-0.18	4.52
	4.95	-19.77	-0.11	4.03
	7.55	-17.00	0.74	2.86
	8.90	-13.47	0.90	2.62
	10.00	-2.70	1.62	2.14
	11.10	7.70	8.12	0.63
HF8	0.00	-75.08	-0.17	4.40
	0.34	-71.73	-0.20	4.45
	0.89	-65.17	-0.18	4.55
	4.95	-19.90	-0.09	4.03
	7.55	-16.97	0.73	2.86
	8.90	-13.51	0.88	2.63
	10.00	-2.70	1.60	2.16
	11.10	7.70	8.05	0.63

Table A.11: Free surface measurements for bursts HF9 to HF11, including the average over all the bursts.

Test	x (m)	z_b (cm)	$\overline{\eta} + S$ (cm)	σ_η (cm)
HF9	0.00	-75.13	-0.16	4.38
	0.34	-71.71	-0.20	4.42
	0.89	-65.09	-0.18	4.52
	4.95	-20.04	-0.10	4.02
	7.55	-16.94	0.74	2.86
	8.90	-13.56	0.90	2.61
	10.00	-2.70	1.64	2.11
	11.10	7.70	8.11	0.62
HF10	0.00	-75.17	-0.16	4.35
	0.34	-71.68	-0.19	4.40
	0.89	-6 5.01	-0.17	4.49
	4.95	-2 0.17	-0.06	4.00
	7.55	-16.91	0.74	2.88
	8.90	-13.60	0.87	2.60
	10.00	-2.70	1.64	2.11
	11.10	7.70	8.07	0.61
HF11	0.00	-75.22	-0.15	4.33
	0.34	-71.66	-0.19	4.38
	0.89	-64.94	-0.17	4.47
	4.95	-20.31	-0.08	3.96
	7.55	-16.88	0.72	2.86
	8.90	-13.65	0.87	2.61
	10.00	-2.70	1.64	2.10
	11.10	7.70	8.08	0.60
Avg.	0.00	-74.96	-0.19	4.40
	0.34	-71.80	-0.22	4.44
	0.89	-65.36	-0.20	4.51
	4.95	-19.56	-0.15	4.11
	7.55	-17.04	0.77	2.86
	8.90	-13.39	0.91	2.63
	10.00	-2.73	1.63	2.14
	11.10	7.63	8.05	0.63

Table A.12: Velocity measurements for bursts HA1 to HA9, including the average over all the bursts.

Test	ADV	x (m)	z_m (cm)	$\overline{U}$ (cm/s)	σ_u (cm/s)
HA1	3D	7.55	2	-6.21	17.18
	2D	8.90	2	-5.88	17.50
HA2	3D	7.55	2	-6.69	17.03
	2D	8.90	2	-5.26	17.45
HA3	3D	7.55	2	-7.06	16.90
	2D	8.90	2	-5.41	17.44
HA4	3D	7.55	2	-6.97	17.93
	2D	8.90	2	-5.44	17.50
HA5	3D	7.55	2	-7.47	17.40
	2D	8.90	2	-4.45	17.65
HA6	3D	7.55	2	-6.93	17.23
	2D	8.90	2	-5.03	17.54
HA7	3D	7.55	2	-7.45	17.23
	2D	8.90	2	-4.23	17.54
HA8	3D	7.55	2	-5.95	17.55
	2D	8.90	2	-4.31	17.38
HA9	3D	7.55	2	-7.24	16.40
	2D	8.90	2	-3.92	17.41
Avg.	3D	7.55	2	-6.89	17.20
	2D	8.90	2	-4.88	17.49

Table A.13: Velocity measurements for bursts HB1 to HB9, including the average over all the bursts.

Test	ADV	x (m)	z_m (cm)	$\overline{U}$ (cm/s)	σ_u (cm/s)
HB1	3D	7.55	2	-6.49	16.73
	2D	8.90	2	-7.14	18.53
HB2	3D	7.55	2	-7.20	18.03
	2D	8.90	2	-6.99	19.08
HB3	3D	7.55	2	-5.88	18.51
	2D	8.90	2	-5.55	19.08
HB4	3D	7.55	2	-5.59	18.17
	2D	8.90	2	-5.18	19.21
HB5	3D	7.55	2	-6.41	18.79
	2D	8.90	2	-5.49	19.89
HB6	3D	7.55	2	-5.19	18.32
	2D	8.90	2	-4.75	19.77
HB7	3D	7.55	2	-6.62	18.34
	2D	8.90	2	-5.00	19.05
HB8	3D	7.55	2	-6.48	18.50
	2D	8.90	2	-4.78	18.93
HB9	3D	7.55	2	-5.96	19.32
	2D	8.90	2	-4.67	19.10
Avg.	3D	7.55	2	-6.20	18.30
	2D	8.90	2	-5.51	19.18

Table A.14: Velocity measurements for bursts HC1 to HC9, including the average over all the bursts.

Test	ADV	x (m)	z_m (cm)	$\overline{U}$ (cm/s)	σ_u (cm/s)
HC1	3D	7.55	2	-5.48	19.62
	2D	8.90	2	-6.27	20.50
HC2	3D	7.55	2	-4.33	18.66
	2D	8.90	2	-5.33	20.34
HC3	3D	7.55	2	-4.87	18.72
	2D	8.90	2	-5.65	19.96
HC4	3D	7.55	2	-4.96	18.35
	2D	8.90	2	-5.63	20.60
HC5	3D	7.55	2	-6.78	19.05
	2D	8.90	2	-5.32	19.41
HC6	3D	7.55	2	-6.63	19.80
	2D	8.90	2	-6.05	19.11
HC7	3D	7.55	2	-7.29	19.22
	2D	8.90	2	-5.61	20.59
HC8	3D	7.55	2	-5.94	18.90
	2D	8.90	2	-4.95	21.40
HC9	3D	7.55	2	-5.07	18.67
	2D	8.90	2	-5.20	19.14
Avg.	3D	7.55	2	-5.70	19.00
	2D	8.90	2	-5.56	20.12

Table A.15: Velocity measurements for bursts HD1 to HD6, including the average over all the bursts.

Test	ADV	x (m)	z_m (cm)	$\overline{U}$ (cm/s)	σ_u (cm/s)
HD1	3D	7.55	2	-4.20	18.44
	2D	8.90	2	-6.17	20.09
HD2	3D	7.55	2	-5.63	20.52
	2D	8.90	2	-5.50	21.51
HD3	3D	7.55	2	-5.10	20.68
	2D	8.90	2	-4.69	20.11
HD4	3D	7.55	2	-5.13	20.19
	2D	8.90	2	-5.02	20.02
HD5	3D	7.55	2	-4.43	19.60
	2D	8.90	2	-6.26	19.64
HD6	3D	7.55	2	-5.06	19.65
	2D	8.90	2	-5.76	19.82
Avg.	3D	7.55	2	-4.92	19.85
	2D	8.90	2	-5.57	20.20

Table A.16: Velocity measurements for bursts HE1 to HE11, including the average over all the bursts.

Test	ADV	x (m)	z_m (cm)	$\overline{U}$ (cm/s)	σ_u (cm/s)
HE1	3D	7.55	2	-5.73	16.14
	2D	8.90	2	-6.46	17.26
HE2	3D	7.55	2	-7.01	17.70
	2D	8.90	2	-6.51	17.96
HE3	3D	7.55	2	-7.27	17.45
	2D	8.90	2	-5.37	18.33
HE4	3D	7.55	2	-6.80	17.62
	2D	8.90	2	-5.28	18.23
HE5	3D	7.55	2	-7.22	17.71
	2D	8.90	2	-5.12	18.66
HE6	3D	7.55	2	-5.84	17.39
	2D	8.90	2	-5.72	18.61
HE7	3D	7.55	2	-5.51	16.89
	2D	8.90	2	-5.32	18.81
HE8	3D	7.55	2	-4.88	16.77
	2D	8.90	2	-4.78	18.03
HE9	3D	7.55	2	-6.13	16.78
	2D	8.90	2	-5.24	17.82
HE10	3D	7.55	2	-6.47	17.27
	2D	8.90	2	-5.02	17.92
HE11	3D	7.55	2	-6.26	18.62
	2D	8.90	2	-6.07	18.31
Avg.	3D	7.55	2	-6.19	17.26
	2D	8.90	2	-5.58	18.13

Table A.17: Velocity measurements for bursts HF1 to HF11, including the average over all the bursts.

Test	ADV	x (m)	z_m (cm)	$\overline{U}$ (cm/s)	σ_u (cm/s)
HF1	3D	7.55	2	-5.38	15.41
	2D	8.90	2	-4.28	16.73
HF2	3D	7.55	2	-6.70	16.48
	2D	8.90	2	-4.26	17.23
HF3	3D	7.55	2	-6.00	16.79
	2D	8.90	2	-3.53	17.29
HF4	3D	7.55	2	-6.04	16.27
	2D	8.90	2	-3.71	16.51
HF5	3D	7.55	2	-6.29	15.62
	2D	8.90	2	-2.86	16.52
HF6	3D	7.55	2	-6.41	15.99
	2D	8.90	2	-3.38	16.88
HF7	3D	7.55	2	-5.80	15.89
	2D	8.90	2	-3.58	16.45
HF8	3D	7.55	2	-6.42	15.97
	2D	8.90	2	-3.66	17.01
HF9	3D	7.55	2	-7.27	16.22
	2D	8.90	2	-3.93	17.83
HF10	3D	7.55	2	-7.42	16.43
	2D	8.90	2	-4.12	17.43
HF11	3D	7.55	2	-6.61	16.84
	2D	8.90	2	-4.70	17.47
Avg.	3D	7.55	2	-6.39	16.17
	2D	8.90	2	-3.82	17.03

Table A.18: Concentration measurements for bursts HA1 to HA9, including the average over all the bursts.

Test	Sensor	x (cm)	z_m (cm)	$\overline{C}$	σ_c	γ_{uc}
HA1	C1	7.55	2	0.0020	0.0010	0.022
	C2	8.90	2	0.0020	0.0012	0.015
HA2	C1	7.55	2	0.0023	0.0009	0.001
	C2	8.90	2	0.0023	0.0014	0.123
HA3	C1	7.55	2	0.0022	0.0008	0.013
	C2	8.90	2	0.0022	0.0007	0.089
HA4	C1	7.55	2	0.0019	0.0009	0.035
	C2	8.90	2	0.0019	0.0007	0.080
HA5	C1	7.55	2	0.0018	0.0006	0.015
	C2	8.90	2	0.0018	0.0008	0.131
HA6	C1	7.55	2	0.0017	0.0006	0.006
	C2	8.90	2	0.0017	0.0008	0.122
HA7	C1	7.55	2	0.0017	0.0005	0.003
	C2	8.90	2	0.0017	0.0007	0.063
HA8	C1	7.55	2	0.0016	0.0005	0.012
	C2	8.90	2	0.0016	0.0007	0.055
HA9	C1	7.55	2	0.0015	0.0005	0.010
	C2	8.90	2	0.0015	0.0009	0.041
Avg	C1	7.55	2	0.0019	0.0007	0.013
	C2	8.90	2	0.0019	0.0009	0.081

Table A.19: Concentration measurements for bursts HB1 to HB9, including the average over all the bursts.

Test	Sensor	x (cm)	z_m (cm)	$\overline{C}$	σ_c	γ_{uc}
HB1	C1	7.55	2	0.0019	0.0011	0.060
	C2	8.90	2	0.0019	0.0009	0.059
HB2	C1	7.55	2	0.0026	0.0010	0.063
	C2	8.90	2	0.0026	0.0009	0.162
HB3	C1	7.55	2	0.0026	0.0011	0.075
	C2	8.90	2	0.0026	0.0009	0.140
HB4	C1	7.55	2	0.0023	0.0016	0.108
	C2	8.90	2	0.0023	0.0009	0.143
HB5	C1	7.55	2	0.0033	0.0011	0.066
	C2	8.90	2	0.0033	0.0021	0.169
HB6	C1	7.55	2	0.0031	0.0012	0.061
	C2	8.90	2	0.0031	0.0015	0.162
HB7	C1	7.55	2	0.0028	0.0009	0.049
	C2	8.90	2	0.0028	0.0012	0.138
HB8	C1	7.55	2	0.0031	0.0011	0.052
	C2	8.90	2	0.0031	0.0013	0.135
HB9	C1	7.55	2	0.0031	0.0011	0.056
	C2	8.90	2	0.0031	0.0013	0.183
Avg	C1	7.55	2	0.0028	0.0011	0.065
	C2	8.90	2	0.0028	0.0012	0.143

Table A.20: Concentration measurements for bursts HC1 to HC9, including the average over all the bursts.

Test	Sensor	x (cm)	z_m (cm)	$\overline{C}$	σ_c	γ_{uc}
HC1	C1	7.55	2	0.0021	0.0011	0.077
	C2	8.90	2	0.0021	0.0012	0.248
HC2	C1	7.55	2	0.0024	0.0012	0.080
	C2	8.90	2	0.0024	0.0012	0.224
HC3	C1	7.55	2	0.0020	0.0009	0.085
	C2	8.90	2	0.0020	0.0010	0.182
HC4	C1	7.55	2	0.0022	0.0011	0.076
	C2	8.90	2	0.0022	0.0012	0.149
HC5	C1	7.55	2	0.0031	0.0016	0.080
	C2	8.90	2	0.0031	0.0016	0.128
HC6	C1	7.55	2	0.0028	0.0013	0.087
	C2	8.90	2	0.0028	0.0012	0.189
HC7	C1	7.55	2	0.0027	0.0012	0.073
	C2	8.90	2	0.0027	0.0015	0.114
HC8	C1	7.55	2	0.0023	0.0009	0.087
	C2	8.90	2	0.0023	0.0014	0.074
HC9	C1	7.55	2	0.0023	0.0010	0.081
	C2	8.90	2	0.0023	0.0008	0.163
Average	C1	7.55	2	0.0024	0.0011	0.081
	C2	8.90	2	0.0024	0.0012	0.163

Table A.21: Concentration measurements for bursts HD1 to HD6, including the average over all the bursts.

Test	Sensor	x (cm)	z_m (cm)	$\overline{C}$	σ_c	γ_{uc}
HD1	C1	7.55	2	0.0023	0.0013	0.080
	C2	8.90	2	0.0023	0.0013	0.105
HD2	C1	7.55	2	0.0029	0.0015	0.080
	C2	8.90	2	0.0029	0.0012	0.145
HD3	C1	7.55	2	0.0038	0.0019	0.072
	C2	8.90	2	0.0038	0.0011	0.217
HD4	C1	7.55	2	0.0047	0.0016	0.053
	C2	8.90	2	0.0047	0.0015	0.194
HD5	C1	7.55	2	0.0040	0.0013	0.040
	C2	8.90	2	0.0040	0.0014	0.161
HD6	C1	7.55	2	0.0020	0.0013	0.127
	C2	8.90	2	0.0020	0.0012	0.203
Avg	C1	7.55	2	0.0033	0.0015	0.075
	C2	8.90	2	0.0033	0.0013	0.171

Table A.22: Concentration measurements for bursts HE1 to HE11, including the average over all the bursts.

Test	Sensor	x (cm)	z_m (cm)	$\overline{C}$	σ_c	γ_{uc}
HE1	C1	7.55	2	0.0013	0.0007	0.089
	C2	8.90	2	0.0013	0.0009	0.198
HE2	C1	7.55	2	0.0015	0.0009	0.118
	C2	8.90	2	0.0015	0.0010	0.224
HE3	C1	7.55	2	0.0014	0.0010	0.134
	C2	8.90	2	0.0014	0.0011	0.187
HE4	C1	7.55	2	0.0013	0.0008	0.109
	C2	8.90	2	0.0013	0.0010	0.097
HE5	C1	7.55	2	0.0013	0.0006	0.090
	C2	8.90	2	0.0013	0.0009	0.096
HE6	C1	7.55	2	0.0014	0.0009	0.084
	C2	8.90	2	0.0014	0.0009	0.117
HE7	C1	7.55	2	0.0013	0.0009	0.120
	C2	8.90	2	0.0013	0.0011	0.162
HE8	C1	7.55	2	0.0013	0.0010	0.111
	C2	8.90	2	0.0013	0.0011	0.138
HE9	C1	7.55	2	0.0013	0.0009	0.114
	C2	8.90	2	0.0013	0.0010	0.157
HE10	C1	7.55	2	0.0013	0.0009	0.101
	C2	8.90	2	0.0013	0.0011	0.138
HE11	C1	7.55	2	0.0011	0.0006	0.099
	C2	8.90	2	0.0011	0.0010	0.183
Avg	C1	7.55	2	0.0013	0.0008	0.106
	C2	8.90	2	0.0013	0.0010	0.154

Table A.23: Concentration measurements for bursts HF1 to HF11, including the average over all the bursts.

Test	Sensor	x (cm)	z_m (cm)	$\overline{C}$	σ_c	γ_{uc}
HF1	C1	7.55	2	0.0009	0.0006	0.115
	C2	8.90	2	0.0009	0.0008	0.087
HF2	C1	7.55	2	0.0009	0.0006	0.097
	C2	8.90	2	0.0009	0.0008	0.052
HF3	C1	7.55	2	0.0009	0.0005	0.147
	C2	8.90	2	0.0009	0.0006	0.120
HF4	C1	7.55	2	0.0008	0.0005	0.121
	C2	8.90	2	0.0008	0.0005	0.102
HF5	C1	7.55	2	0.0008	0.0005	0.102
	C2	8.90	2	0.0008	0.0005	0.142
HF6	C1	7.55	2	0.0009	0.0006	0.129
	C2	8.90	2	0.0009	0.0006	0.184
HF7	C1	7.55	2	0.0009	0.0006	0.148
	C2	8.90	2	0.0009	0.0006	0.144
HF8	C1	7.55	2	0.0009	0.0007	0.134
	C2	8.90	2	0.0009	0.0006	0.184
HF9	C1	7.55	2	0.0008	0.0004	0.097
	C2	8.90	2	0.0008	0.0006	0.135
HF10	C1	7.55	2	0.0007	0.0004	0.083
	C2	8.90	2	0.0007	0.0005	0.126
HF11	C1	7.55	2	0.0008	0.0005	0.097
	C2	8.90	2	0.0008	0.0006	0.084
Avg	C1	7.55	2	0.0008	0.0005	0.116
	C2	8.90	2	0.0008	0.0006	0.124

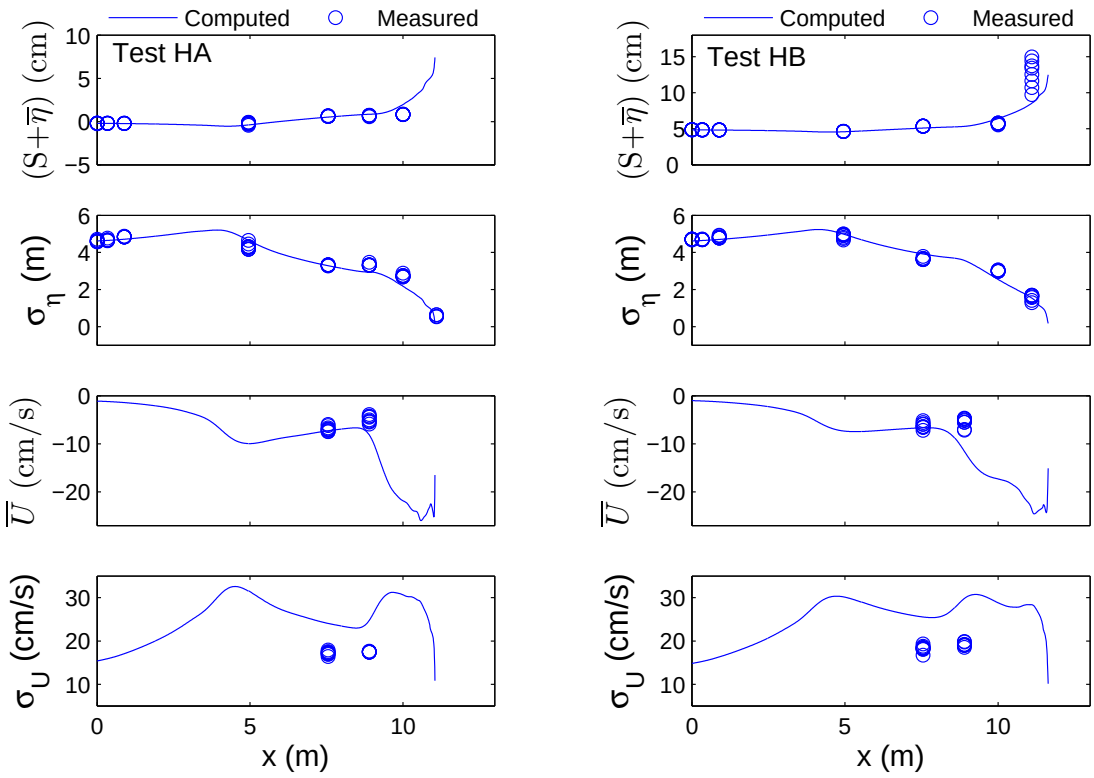

Figure A.1: Cross-shore variations of measured vs. computed $(S + \bar{\eta})$, σ_η, $\bar{U}$ and σ_U for tests HA (left) and HB (right)

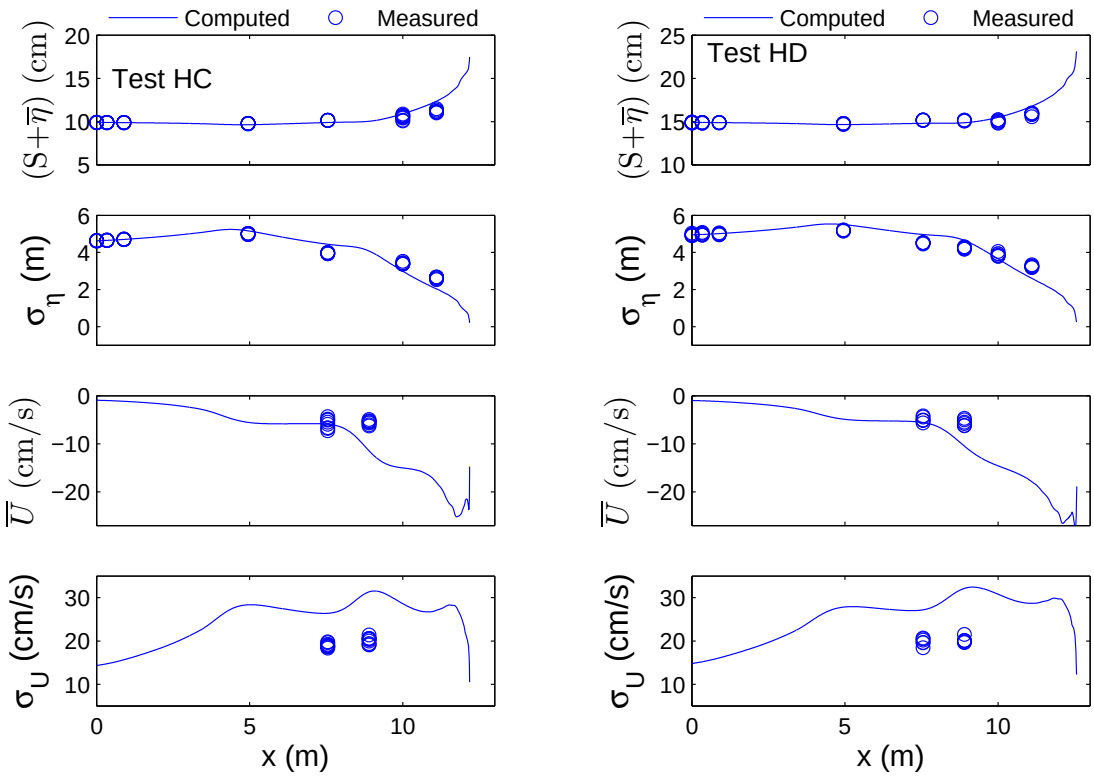

Figure A.2: Cross-shore variations of measured vs. computed $(S + \bar{\eta})$, σ_η, $\bar{U}$ and σ_U for tests HC (left) and HD (right)

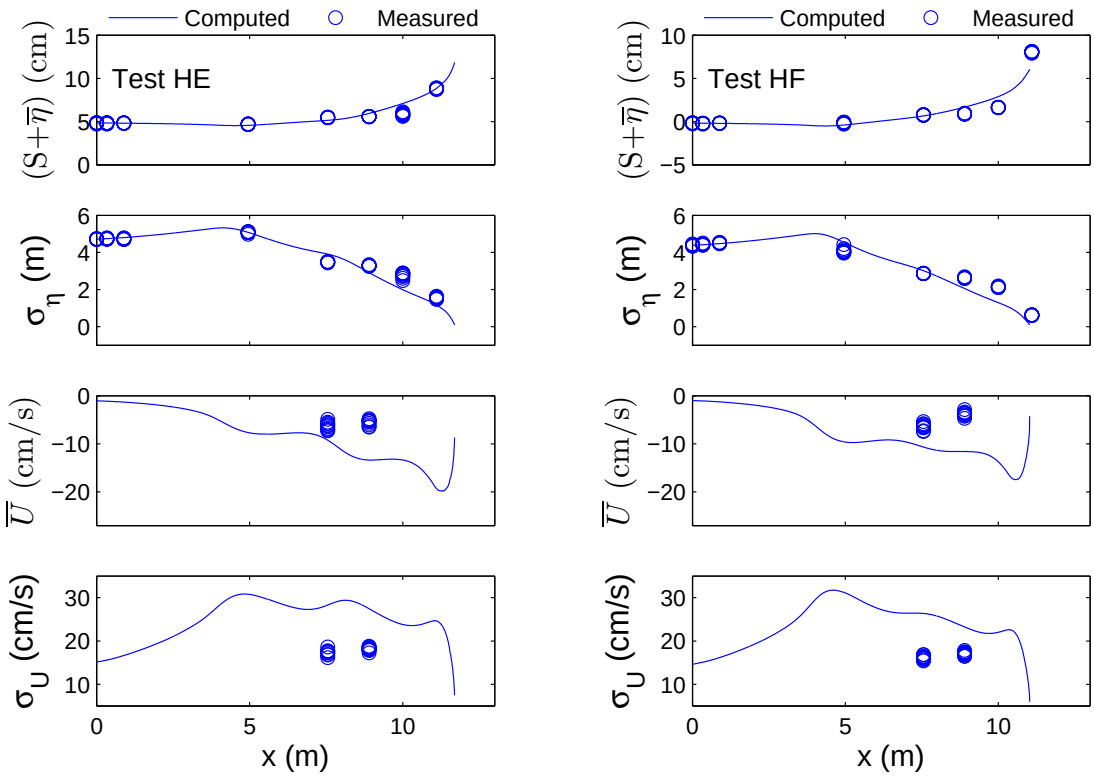

Figure A.3: Cross-shore variations of measured vs. computed $(S + \bar{\eta})$, σ_η, $\bar{U}$ and σ_U for tests HE (left) and HF (right)

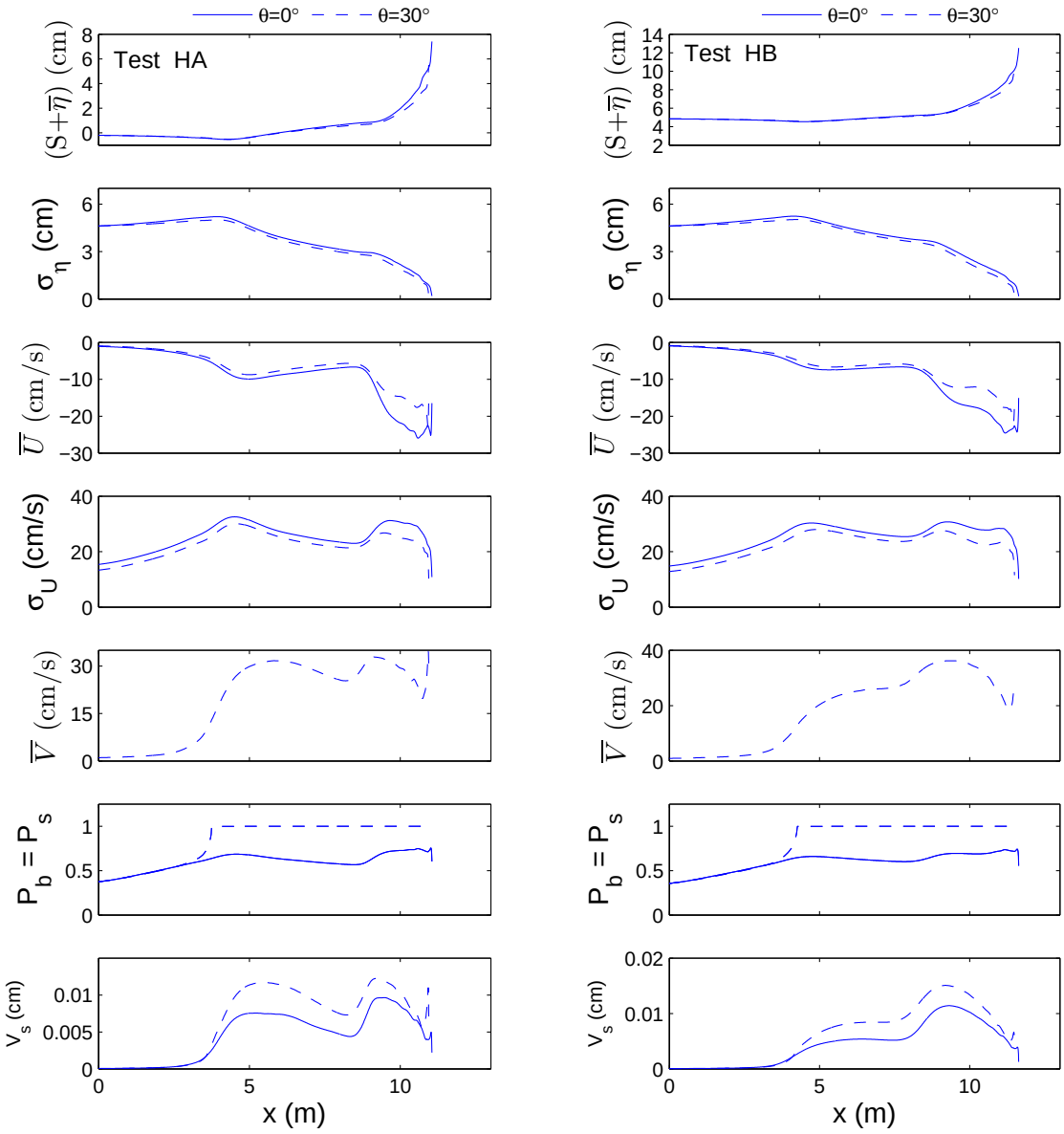

Figure A.4: Cross-shore variations of $(S + \bar{\eta})$, σ_η, $\bar{U}$, σ_U, $\bar{V}$, $P_b = P_s$ and V_s for $\theta = 0°$ and $\theta = 30°$ for tests HA (left) and HB (right)

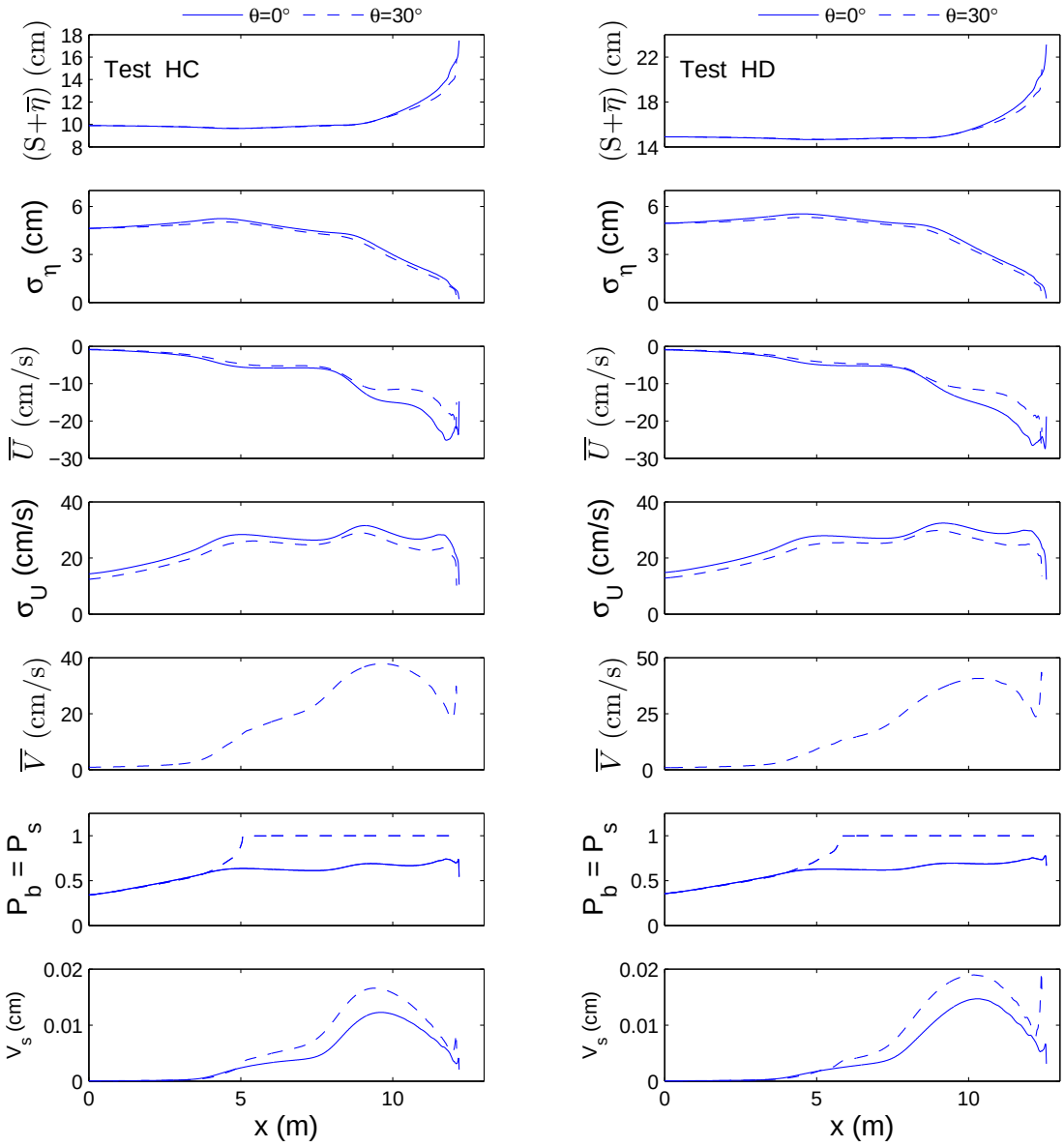

Figure A.5: Cross-shore variations of $(S + \bar{\eta})$, σ_η, $\bar{U}$, σ_U, $\bar{V}$, $P_b = P_s$ and V_s for $\theta = 0°$ and $\theta = 30°$ for tests HC (left) and HD (right)

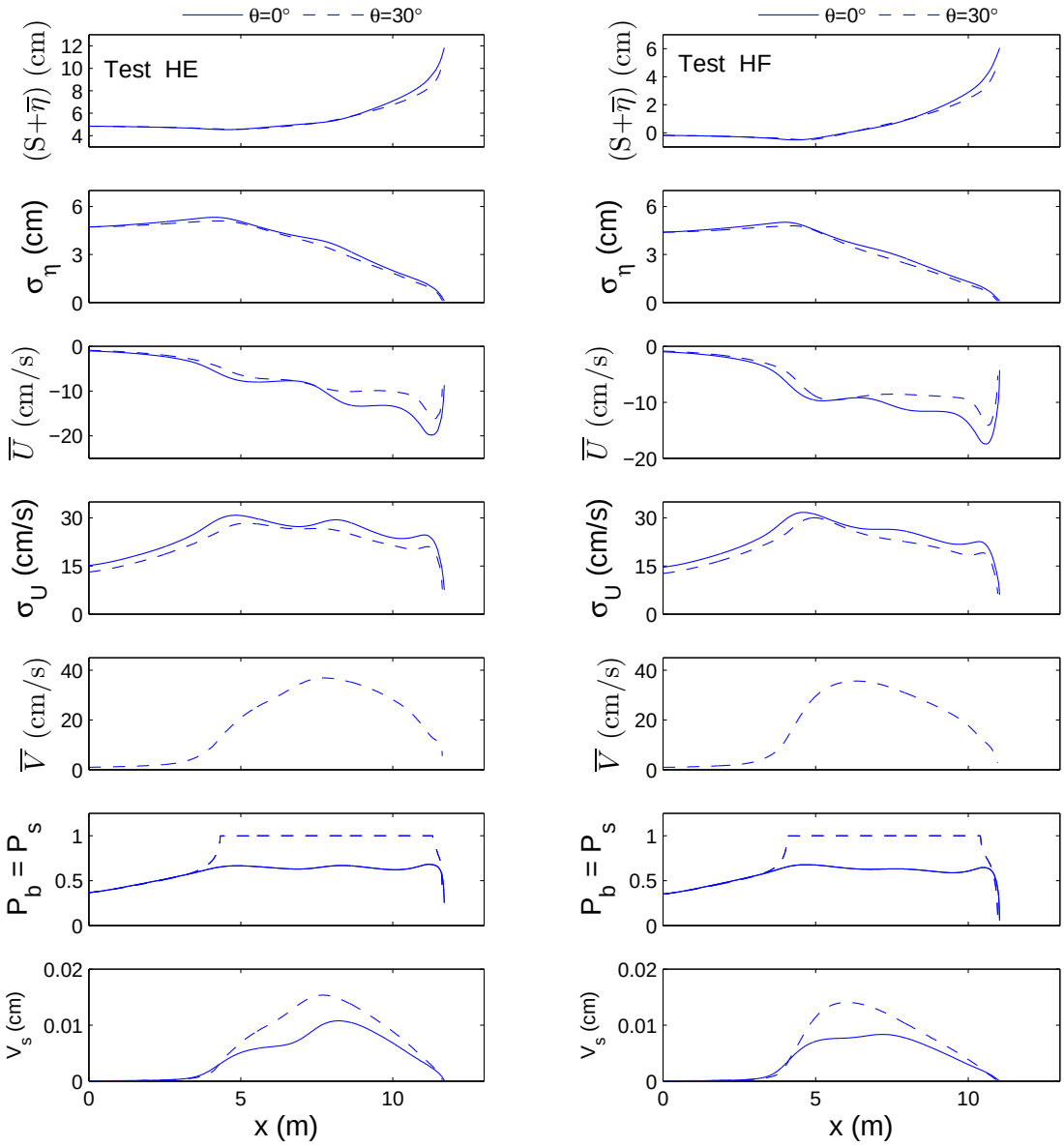

Figure A.6: Cross-shore variations of $(S + \bar{\eta})$, σ_η, $\bar{U}$, σ_U, $\bar{V}$, $P_b = P_s$ and V_s for $\theta = 0°$ and $\theta = 30°$ for tests HE (left) and HF (right)

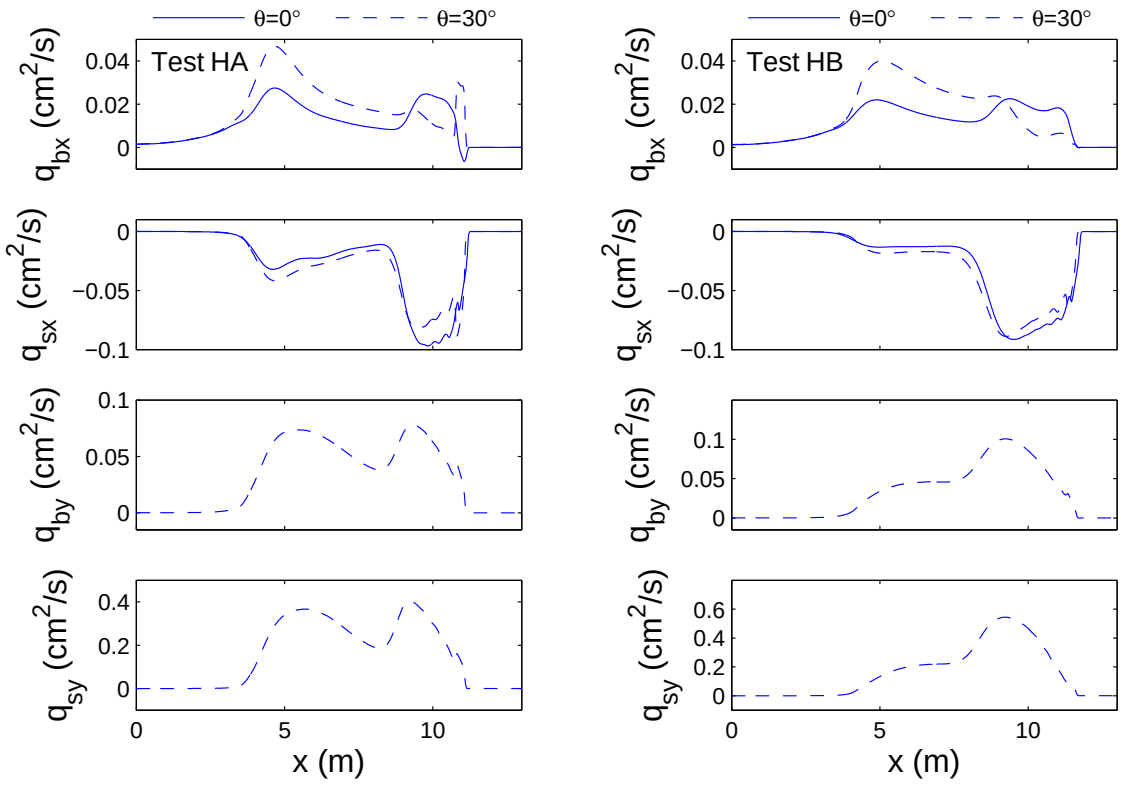

Figure A.7: Cross-shore variations of q_{bx}, q_{sx}, q_{by} and q_{sy} for $\theta = 0°$ and $\theta = 30°$ in tests HA (left) and HB (right).

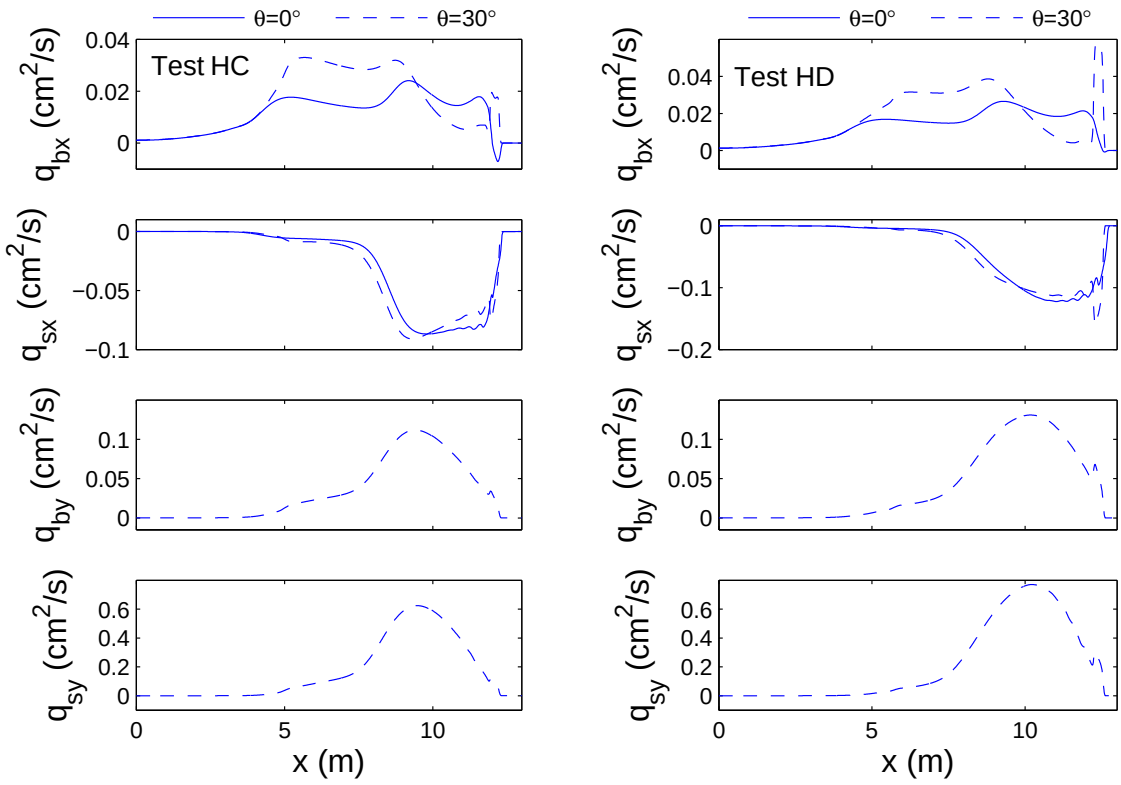

Figure A.8: Cross-shore variations of q_{bx}, q_{sx}, q_{by} and q_{sy} for $\theta = 0°$ and $\theta = 30°$ in tests HC (left) and HD (right).

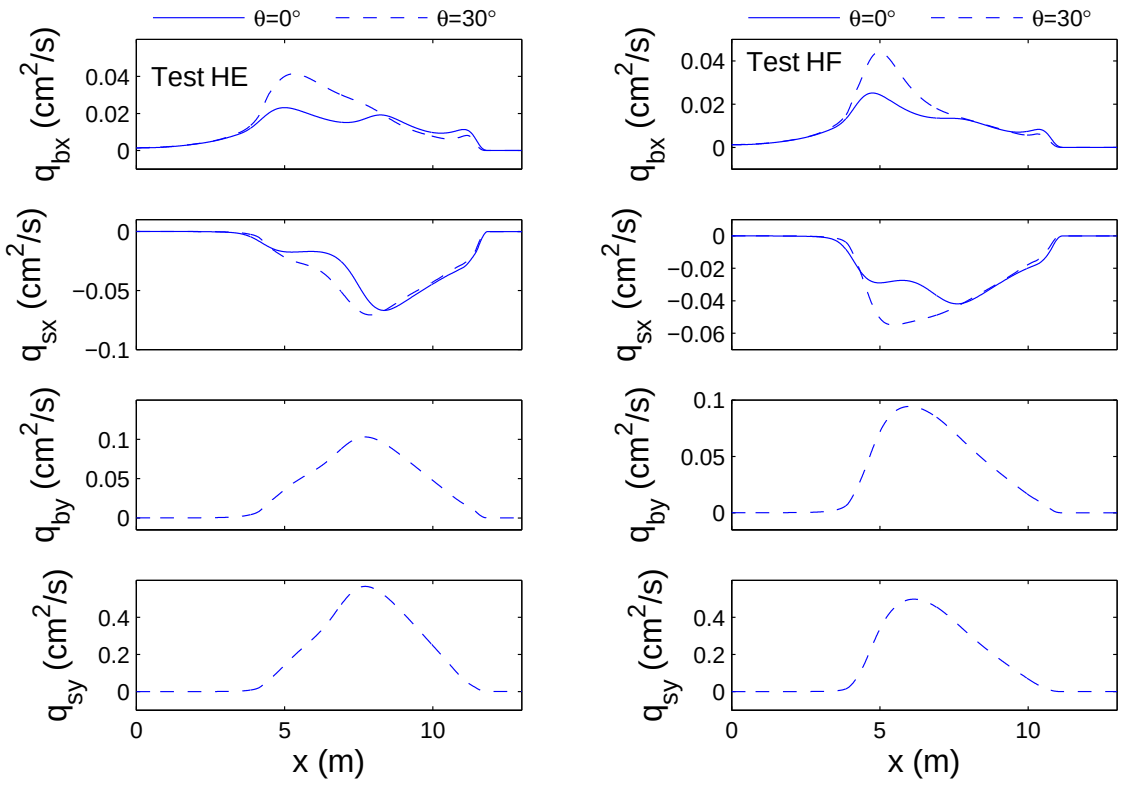

Figure A.9: Cross-shore variations of q_{bx}, q_{sx}, q_{by} and q_{sy} for $\theta = 0°$ and $\theta = 30°$ in tests HE (left) and HF (right).

Appendix B

EXPERIMENT L

Table B.1: Free surface measurements for bursts LA1 to LA8.

Test	x (m)	z_b (cm)	$\overline{\eta}+S$ (cm)	σ_η (cm)
LA1	0.00	-76.00	-0.17	4.63
	0.34	-71.63	-0.18	4.67
	0.89	-65.14	-0.23	4.76
	4.95	-19.53	-0.19	4.49
	7.55	-17.92	0.72	3.00
	8.90	-18.35	0.89	3.13
	10.00	4.10	7.55	1.96
	11.10	10.00	11.78	0.41
LA2	0.00	-75.90	-0.15	4.59
	0.34	-71.64	-0.19	4.62
	0.89	-65.16	-0.18	4.74
	4.95	-19.64	-0.04	4.34
	7.55	-17.98	0.68	2.95
	8.90	-17.98	0.87	2.95
	10.00	3.38	5.74	1.87
	11.10	9.99	10.57	0.27
LA3	0.00	-75.80	-0.12	4.56
	0.34	-71.64	-0.16	4.58
	0.89	-65.17	-0.17	4.70
	4.95	-19.75	NR	NR
	7.55	-18.04	0.69	2.97
	8.90	-17.60	0.81	2.91
	10.00	2.65	5.10	1.92
	11.10	9.98	10.32	0.27
LA4	0.00	-75.70	-0.12	4.56
	0.34	-71.64	-0.16	4.57
	0.89	-65.19	-0.16	4.71
	4.95	-19.87	-0.15	4.23
	7.55	-18.11	0.71	2.98
	8.90	-17.23	0.81	2.87
	10.00	1.93	4.23	2.03
	11.10	9.96	10.08	0.28

Test	x (m)	z_b (cm)	$\overline{\eta}+S$ (cm)	σ_η (cm)
LA5	0.00	-75.60	-0.12	4.54
	0.34	-71.65	-0.14	4.56
	0.89	-65.20	-0.16	4.70
	4.95	-19.98	-0.09	4.21
	7.55	-18.17	0.69	2.99
	8.90	-16.86	0.79	2.83
	10.00	1.20	3.32	2.11
	11.10	9.95	10.19	0.28
LA6	0.00	-75.50	-0.13	4.53
	0.34	-71.65	-0.16	4.55
	0.89	-65.21	-0.16	4.70
	4.95	-20.09	-0.08	4.21
	7.55	-18.24	0.69	3.00
	8.90	-16.49	0.80	2.86
	10.00	0.48	2.49	2.18
	11.10	9.94	10.09	0.29
LA7	0.00	-75.40	-0.12	4.54
	0.34	-71.66	-0.14	4.55
	0.89	-65.23	-0.16	4.70
	4.95	-20.21	-0.12	4.16
	7.55	-18.30	0.66	3.00
	8.90	-16.11	0.80	2.83
	10.00	-0.25	2.00	2.19
	11.10	9.93	10.07	0.32
LA8	0.00	-75.30	-0.11	4.53
	0.34	-71.66	-0.14	4.55
	0.89	-65.24	-0.14	4.72
	4.95	-20.32	-0.07	4.19
	7.55	-18.36	0.70	2.99
	8.90	-15.74	0.79	2.84
	10.00	-0.98	1.92	2.24
	11.10	9.91	10.03	0.34

Table B.2: Free surface measurements for burst LA9 and the average over all the bursts.

Test	x (m)	z_b (cm)	$\overline{\eta} + S$ (cm)	σ_η (cm)
LA9	0.00	-75.20	-0.11	4.52
	0.34	-71.66	-0.13	4.54
	0.89	-65.26	-0.14	4.69
	4.95	-20.43	-0.09	4.17
	7.55	-18.43	0.69	3.02
	8.90	-15.37	0.80	2.82
	10.00	-1.70	1.91	2.23
	11.10	9.90	10.31	0.34

Test	x (m)	z_b (cm)	$\overline{\eta} + S$ (cm)	σ_η (cm)
Avg.	0.00	-75.60	-0.13	4.56
	0.34	-71.65	-0.16	4.58
	0.89	-65.20	-0.17	4.71
	4.95	-19.98	-0.10	4.91
	7.55	-18.17	0.69	2.99
	8.90	-16.86	0.82	2.89
	10.00	1.20	3.81	2.08
	11.10	9.95	10.38	0.31

Table B.3: Free surface measurements for bursts LB1 to LB8.

Test	x (m)	z_b (cm)	$\overline{\eta}+S$ (cm)	σ_η (cm)
LB1	0.00	-75.20	4.80	4.69
	0.34	-71.66	4.78	4.75
	0.89	-65.26	4.80	4.86
	4.95	-20.43	4.70	4.73
	7.55	-18.43	5.33	3.51
	8.90	-15.37	5.49	3.36
	10.00	-1.70	5.86	2.81
	11.10	9.90	10.11	1.44
LB2	0.00	-75.14	4.85	4.73
	0.34	-71.61	4.84	4.77
	0.89	-65.16	4.85	4.86
	4.95	-20.16	NR	NR
	7.55	-18.30	5.40	3.51
	8.90	-15.25	5.47	3.45
	10.00	-1.86	6.00	2.77
	11.10	7.10	8.80	1.64
LB3	0.00	-75.08	4.86	4.74
	0.34	-71.55	4.85	4.77
	0.89	-65.06	4.85	4.83
	4.95	-19.89	NR	NR
	7.55	-18.17	5.40	3.51
	8.90	-15.13	5.47	3.42
	10.00	-2.03	6.01	2.77
	11.10	6.40	8.29	1.69
LB4	0.00	-75.01	4.87	4.76
	0.34	-71.50	4.86	4.78
	0.89	-64.96	4.86	4.83
	4.95	-19.62	NR	NR
	7.55	-18.04	5.40	3.51
	8.90	-15.02	5.47	3.43
	10.00	-2.19	5.92	2.82
	11.10	6.40	8.32	1.73

Test	x (m)	z_b (cm)	$\overline{\eta}+S$ (cm)	σ_η (cm)
LB5	0.00	-74.95	4.86	4.77
	0.34	-71.44	4.87	4.79
	0.89	-64.86	4.85	4.82
	4.95	-19.35	NR	NR
	7.55	-17.92	5.42	3.52
	8.90	-14.90	5.52	3.43
	10.00	-2.35	5.98	2.83
	11.10	6.40	8.40	1.77
LB6	0.00	-74.89	4.87	4.77
	0.34	-71.39	4.86	4.79
	0.89	-64.76	4.84	4.80
	4.95	-19.08	NR	NR
	7.55	-17.79	5.44	3.52
	8.90	-14.78	5.51	3.42
	10.00	-2.51	6.01	2.86
	11.10	6.40	8.37	1.79
LB7	0.00	-74.83	4.88	4.79
	0.34	-71.33	4.86	4.80
	0.89	-64.66	4.86	4.79
	4.95	-18.81	NR	NR
	7.55	-17.66	5.40	3.52
	8.90	-14.67	5.50	3.41
	10.00	-2.68	5.96	2.87
	11.10	6.40	8.33	1.63
LB8	0.00	-74.76	4.86	4.77
	0.34	-71.27	4.85	4.79
	0.89	-64.57	4.86	4.79
	4.95	-18.54	NR	NR
	7.55	-17.54	5.41	3.52
	8.90	-14.55	5.51	3.42
	10.00	-2.84	5.92	2.91
	11.10	6.40	8.45	1.78

Table B.4: Free surface measurements for burst LB9 and the average over all the bursts.

Test	x (m)	z_b (cm)	$\overline{\eta} + S$ (cm)	σ_η (cm)
	0.00	-74.70	4.88	4.77
	0.34	-71.22	4.87	4.78
	0.89	-64.47	4.86	4.78
LB9	4.95	-18.27	NR	NR
	7.55	-17.41	5.43	3.50
	8.90	-14.43	5.52	3.39
	10.00	-3.00	5.90	2.92
	11.10	6.40	8.56	1.80

Test	x (m)	z_b (cm)	$\overline{\eta} + S$ (cm)	σ_η (cm)
	0.00	-74.95	4.86	4.75
	0.34	-71.44	4.85	4.78
	0.89	-64.86	4.85	4.82
Avg.	4.95	-19.35	4.70	4.73
	7.55	-17.92	5.40	3.51
	8.90	-14.90	5.50	3.41
	10.00	-2.35	5.95	2.84
	11.10	6.87	8.62	1.70

Table B.5: Free surface measurements for bursts LC1 to LC8.

Test	x (m)	z_b (cm)	$\overline{\eta}+S$ (cm)	σ_η (cm)
LC1	0.00	-74.70	9.85	4.84
	0.34	-71.22	9.87	4.81
	0.89	-64.47	9.87	4.87
	4.95	-18.27	9.73	5.22
	7.55	-17.41	10.17	3.94
	8.90	-14.43	10.26	3.79
	10.00	-3.00	10.56	3.56
	11.10	6.40	11.15	2.53
LC2	0.00	-74.76	9.89	4.84
	0.34	-71.29	9.89	4.82
	0.89	-64.54	9.88	4.86
	4.95	-18.46	9.72	5.21
	7.55	-17.45	10.18	3.95
	8.90	-14.41	10.30	3.82
	10.00	-2.58	10.55	3.52
	11.10	5.90	11.00	2.63
LC3	0.00	-74.83	9.90	4.84
	0.34	-71.36	9.91	4.80
	0.89	-64.61	9.89	4.86
	4.95	-18.64	9.71	5.21
	7.55	-17.48	10.19	3.94
	8.90	-14.38	10.33	3.81
	10.00	-2.15	10.29	3.46
	11.10	5.50	10.89	2.60
LC4	0.00	-74.89	9.89	4.84
	0.34	-71.44	9.91	4.80
	0.89	-64.68	9.89	4.85
	4.95	-18.83	9.71	5.22
	7.55	-17.52	10.18	3.91
	8.90	-14.35	10.32	3.83
	10.00	-1.73	10.28	3.46
	11.10	5.50	11.03	2.58

Test	x (m)	z_b (cm)	$\overline{\eta}+S$ (cm)	σ_η (cm)
LC5	0.00	-74.95	9.91	4.80
	0.34	-71.51	9.91	4.75
	0.89	-64.75	9.88	4.78
	4.95	-19.01	9.74	5.17
	7.55	-17.56	10.18	3.92
	8.90	-14.33	10.25	3.82
	10.00	-1.30	10.31	3.42
	11.10	5.50	11.00	2.55
LC6	0.00	-75.01	9.91	4.84
	0.34	-71.58	9.92	4.79
	0.89	-64.82	9.90	4.82
	4.95	-20.09	9.71	5.21
	7.55	-19.20	10.19	3.91
	8.90	-14.30	10.29	3.83
	10.00	-0.88	10.27	3.39
	11.10	5.50	11.07	2.54
LC7	0.00	-75.08	9.90	4.82
	0.34	-71.66	9.91	4.79
	0.89	-64.89	9.90	4.81
	4.95	-20.21	9.73	5.20
	7.55	-19.38	10.19	3.91
	8.90	-14.27	10.32	3.82
	10.00	-0.45	10.26	3.39
	11.10	5.50	11.14	2.56
LC8	0.00	-75.14	9.90	4.83
	0.34	-71.73	9.91	4.79
	0.89	-64.95	9.88	4.82
	4.95	-20.32	9.73	5.19
	7.55	-19.57	10.19	3.89
	8.90	-14.24	10.27	3.79
	10.00	-0.02	10.27	3.40
	11.10	5.50	11.16	2.57

Table B.6: Free surface measurements for burst LC9 and the average over all the bursts.

Test	x (m)	z_b (cm)	$\overline{\eta} + S$ (cm)	σ_η (cm)
LC9	0.00	-75.20	9.91	4.83
	0.34	-71.80	9.92	4.79
	0.89	-65.02	9.90	4.81
	4.95	-19.75	9.72	5.18
	7.55	-17.70	10.18	3.89
	8.90	-14.22	10.34	3.83
	10.00	0.40	10.31	3.36
	11.10	5.50	11.18	2.53

Test	x (m)	z_b (cm)	$\overline{\eta} + S$ (cm)	σ_η (cm)
Avg.	0.00	-74.95	9.89	4.83
	0.34	-71.51	9.90	4.79
	0.89	-64.75	9.89	4.83
	4.95	-19.29	9.72	5.20
	7.55	-18.14	10.18	3.92
	8.90	-14.33	10.30	3.81
	10.00	-1.30	10.34	3.44
	11.10	5.64	11.07	2.57

Table B.7: Free surface measurements for bursts LD1 to LD6, including the average over all the bursts.

Test	x (m)	z_b (cm)	$\overline{\eta}+S$ (cm)	σ_η (cm)
	0.00	-75.20	14.91	4.85
	0.34	-71.80	14.92	4.92
	0.89	-65.02	14.94	4.84
LD1	4.95	-19.75	NR	NR
	7.55	-17.70	15.15	4.35
	8.90	-14.22	15.20	4.22
	10.00	0.40	15.40	3.97
	11.10	5.50	15.31	3.24
	0.00	-75.06	14.95	4.92
	0.34	-71.77	14.95	4.98
	0.89	-65.05	14.95	4.91
LD2	4.95	-19.84	NR	NR
	7.55	-17.57	15.13	4.44
	8.90	-14.07	15.22	4.24
	10.00	0.86	15.31	4.00
	11.10	7.20	15.83	3.23
	0.00	-74.91	14.96	4.94
	0.34	-71.74	14.95	4.99
	0.89	-65.08	14.92	4.94
LD3	4.95	-19.94	NR	NR
	7.55	-17.44	15.15	4.45
	8.90	-13.93	15.19	4.19
	10.00	1.32	15.32	4.01
	11.10	7.20	15.79	3.20
	0.00	-74.77	14.94	4.82
	0.34	-71.71	14.94	4.86
	0.89	-65.10	14.93	4.81
LD4	4.95	-20.03	NR	NR
	7.55	-17.30	15.09	4.43
	8.90	-13.79	15.16	4.10
	10.00	1.78	15.32	3.98
	11.10	7.20	15.93	3.17

Test	x (m)	z_b (cm)	$\overline{\eta}+S$ (cm)	σ_η (cm)
	0.00	-74.62	14.95	4.80
	0.34	-71.68	14.95	4.83
	0.89	-65.13	14.92	4.82
LD5	4.95	-20.12	NR	NR
	7.55	-17.17	15.06	4.40
	8.90	-13.64	15.12	4.05
	10.00	2.24	15.27	3.94
	11.10	7.20	15.97	3.18
	0.00	-74.48	14.86	4.92
	0.34	-71.65	14.87	4.96
	0.89	-65.15	14.84	5.04
LD6	4.95	-20.22	14.60	5.38
	7.55	-17.03	15.13	4.46
	8.90	-13.50	15.16	4.21
	10.00	2.70	15.32	3.99
	11.10	7.20	15.96	3.24
	0.00	-74.84	14.93	4.87
	0.34	-71.73	14.93	4.92
	0.89	-65.09	14.92	4.89
Avg.	4.95	-19.98	14.60	5.38
	7.55	-17.37	15.12	4.42
	8.90	-13.86	15.17	4.17
	10.00	1.55	15.32	3.98
	11.10	6.92	15.80	3.21

Table B.8: Free surface measurements for bursts LE1 to LE8.

Test	x (m)	z_b (cm)	$\overline{\eta}+S$ (cm)	σ_η (cm)
LE1	0.00	-74.48	4.84	4.63
	0.34	-71.65	4.83	4.66
	0.89	-65.15	4.84	4.66
	4.95	-20.22	4.49	5.04
	7.55	-17.03	5.49	3.33
	8.90	-13.50	5.69	3.24
	10.00	2.70	6.25	2.54
	11.10	7.20	9.59	1.43
LE2	0.00	-74.46	4.86	4.68
	0.34	-71.65	4.86	4.70
	0.89	-65.14	4.85	4.70
	4.95	-19.92	4.38	5.18
	7.55	-16.95	5.52	3.31
	8.90	-13.44	5.70	3.22
	10.00	2.18	5.89	2.71
	11.10	8.00	9.27	1.44
LE3	0.00	-74.44	4.89	4.70
	0.34	-71.64	4.81	4.73
	0.89	-65.14	4.83	4.70
	4.95	-19.62	4.36	5.22
	7.55	-16.87	5.51	3.36
	8.90	-13.38	5.70	3.26
	10.00	1.66	5.98	2.78
	11.10	8.00	9.58	1.50
LE4	0.00	-74.42	4.89	4.70
	0.34	-71.64	4.87	4.72
	0.89	-65.13	4.87	4.70
	4.95	-19.32	4.37	5.24
	7.55	-16.79	5.52	3.35
	8.90	-13.32	5.67	3.24
	10.00	1.14	6.02	2.79
	11.10	8.00	9.67	1.47

Test	x (m)	z_b (cm)	$\overline{\eta}+S$ (cm)	σ_η (cm)
LE5	0.00	-74.40	4.89	4.67
	0.34	-71.64	4.87	4.69
	0.89	-65.12	4.88	4.66
	4.95	-19.03	4.41	5.14
	7.55	-16.71	5.47	3.34
	8.90	-13.26	5.66	3.25
	10.00	0.62	5.94	2.82
	11.10	8.00	9.52	1.47
LE6	0.00	-74.38	4.89	4.68
	0.34	-71.63	4.87	4.69
	0.89	-65.12	4.86	4.66
	4.95	-18.73	4.40	5.17
	7.55	-16.63	5.51	3.32
	8.90	-13.20	5.67	3.26
	10.00	0.10	5.83	2.88
	11.10	8.00	9.47	1.45
LE7	0.00	-74.36	4.89	4.68
	0.34	-71.63	4.88	4.70
	0.89	-65.11	4.87	4.67
	4.95	-18.43	4.40	5.13
	7.55	-16.55	5.51	3.34
	8.90	-13.14	5.66	3.22
	10.00	-0.42	5.77	2.87
	11.10	8.00	9.56	1.41
LE8	0.00	-74.34	4.90	4.67
	0.34	-71.63	4.87	4.69
	0.89	-65.10	4.87	4.66
	4.95	-18.14	4.37	5.16
	7.55	-16.47	5.45	3.28
	8.90	-13.08	5.65	3.23
	10.00	-0.94	5.73	2.90
	11.10	8.00	9.61	1.38

Table B.9: Free surface measurements for bursts LE9 to LE11, including the average over all the bursts.

Test	x (m)	z_b (cm)	$\overline{\eta} + S$ (cm)	σ_η (cm)
LE9	0.00	-74.32	4.90	4.67
	0.34	-71.63	4.88	4.69
	0.89	-65.09	4.87	4.66
	4.95	-17.84	4.34	5.20
	7.55	-16.39	5.47	3.26
	8.90	-13.01	5.66	3.23
	10.00	-1.46	5.69	2.96
	11.10	8.00	9.51	1.38
LE10	0.00	-74.28	4.89	4.66
	0.34	-71.62	4.88	4.68
	0.89	-65.08	4.87	4.66
	4.95	-17.25	4.37	5.16
	7.55	-16.23	5.53	3.28
	8.90	-12.89	5.66	3.21
	10.00	-2.50	5.69	2.97
	11.10	8.00	9.45	1.37

Test	x (m)	z_b (cm)	$\overline{\eta} + S$ (cm)	σ_η (cm)
LE11	0.00	-74.28	4.89	4.67
	0.34	-71.62	4.88	4.68
	0.89	-65.08	4.88	4.66
	4.95	-17.25	4.35	5.12
	7.55	-16.23	5.47	3.28
	8.90	-12.89	5.67	3.20
	10.00	-2.50	5.70	2.98
	11.10	8.00	9.33	1.34
Avg.	0.00	-74.38	4.89	4.67
	0.34	-71.63	4.86	4.69
	0.89	-65.11	4.86	4.67
	4.95	-18.70	4.38	5.16
	7.55	-16.62	5.50	3.31
	8.90	-13.19	5.67	3.23
	10.00	0.05	5.86	2.84
	11.10	7.93	9.51	1.42

Table B.10: Free surface measurements for bursts LF1 to LF8.

Test	x (m)	z_b (cm)	$\overline{\eta}+S$ (cm)	σ_η (cm)
LF1	0.00	-74.28	-0.18	4.56
	0.34	-71.62	-0.20	4.62
	0.89	-65.08	-0.22	4.63
	4.95	-17.25	-0.49	4.65
	7.55	-16.23	0.83	2.84
	8.90	-12.89	1.05	2.76
	10.00	-2.50	1.61	2.23
	11.10	8.00	8.42	0.50
LF2	0.00	-74.24	-0.17	4.57
	0.34	-71.46	-0.19	4.61
	0.89	-64.95	-0.21	4.67
	4.95	-17.51	-0.41	4.52
	7.55	-16.23	0.86	2.86
	8.90	-13.02	1.00	2.74
	10.00	-2.52	1.73	2.21
	11.10	8.00	8.32	0.52
LF3	0.00	-74.24	-0.15	4.58
	0.34	-71.31	-0.17	4.64
	0.89	-64.83	-0.20	4.73
	4.95	-17.77	-0.33	4.48
	7.55	-16.24	0.84	2.87
	8.90	-13.15	1.02	2.76
	10.00	-2.54	1.70	2.23
	11.10	8.00	8.31	0.53
LF4	0.00	-74.24	-0.15	4.57
	0.34	-71.15	-0.16	4.63
	0.89	-64.71	-0.18	4.74
	4.95	-18.04	-0.38	4.39
	7.55	-16.24	0.82	2.86
	8.90	-13.28	1.00	2.73
	10.00	-2.56	1.65	2.22
	11.10	8.00	8.27	0.56

Test	x (m)	z_b (cm)	$\overline{\eta}+S$ (cm)	σ_η (cm)
LF5	0.00	-74.24	-0.13	4.57
	0.34	-70.99	-0.15	4.63
	0.89	-64.58	-0.16	4.75
	4.95	-18.30	-0.30	4.36
	7.55	-16.24	0.88	2.86
	8.90	-13.41	0.99	2.70
	10.00	-2.58	1.62	2.24
	11.10	8.00	8.33	0.53
LF6	0.00	-74.24	-0.14	4.57
	0.34	-70.84	-0.15	4.64
	0.89	-64.46	-0.16	4.75
	4.95	-18.57	-0.31	4.32
	7.55	-16.25	0.85	2.86
	8.90	-13.54	0.96	2.69
	10.00	-2.60	1.56	2.24
	11.10	8.00	8.30	0.53
LF7	0.00	-74.24	-0.14	4.56
	0.34	-70.68	-0.15	4.61
	0.89	-64.33	-0.18	4.75
	4.95	-18.83	-0.32	4.41
	7.55	-16.25	0.80	2.87
	8.90	-13.67	0.98	2.71
	10.00	-2.62	1.59	2.24
	11.10	8.00	8.22	0.52
LF8	0.00	-74.24	-0.14	4.56
	0.34	-70.52	-0.16	4.62
	0.89	-64.21	-0.18	4.75
	4.95	-19.10	-0.30	4.31
	7.55	-16.25	0.79	2.86
	8.90	-13.79	1.00	2.73
	10.00	-2.64	1.64	2.21
	11.10	8.00	8.33	0.52

Table B.11: Free surface measurements for bursts LF9 to LF11, including the average over all the bursts.

Test	x (m)	z_b (cm)	$\overline{\eta}+S$ (cm)	σ_η (cm)
LF9	0.00	-74.24	-0.14	4.55
	0.34	-70.37	-0.15	4.61
	0.89	-64.09	-0.16	4.73
	4.95	-19.36	-0.34	4.34
	7.55	-16.25	0.77	2.87
	8.90	-13.92	0.96	2.70
	10.00	-2.66	1.57	2.21
	11.10	8.00	8.30	0.51
LF10	0.00	-74.24	-0.13	4.55
	0.34	-70.21	-0.14	4.61
	0.89	-63.96	-0.17	4.73
	4.95	-19.62	-0.34	4.37
	7.55	-16.26	0.78	2.89
	8.90	-14.05	0.95	2.69
	10.00	-2.68	1.64	2.24
	11.10	8.00	8.30	0.52

Test	x (m)	z_b (cm)	$\overline{\eta}+S$ (cm)	σ_η (cm)
LF11	0.00	-74.24	-0.13	4.55
	0.34	-70.06	-0.15	4.62
	0.89	-63.84	-0.17	4.73
	4.95	-19.89	-0.24	4.25
	7.55	-16.26	0.78	2.88
	8.90	-14.18	0.97	2.70
	10.00	-2.70	1.67	2.24
	11.10	8.00	8.34	0.52
Avg.	0.00	-74.24	-0.14	4.56
	0.34	-70.84	-0.16	4.62
	0.89	-64.46	-0.18	4.72
	4.95	-18.57	-0.34	4.40
	7.55	-16.25	0.82	2.86
	8.90	-13.54	0.99	2.72
	10.00	-2.60	1.63	2.23
	11.10	8.00	8.31	0.53

Table B.12: Velocity measurements for bursts LA1 to LA9, including the average over all the bursts.

Test	ADV	x (m)	z_m (cm)	$\overline{U}$ (cm/s)	σ_u (cm/s)
LA1	3D	7.55	2	-8.77	17.32
	2D	8.90	2	-5.83	14.36
LA2	3D	7.55	2	-8.10	15.89
	2D	8.90	2	-3.84	16.25
LA3	3D	7.55	2	-7.87	16.04
	2D	8.90	2	-3.96	16.94
LA4	3D	7.55	2	-7.87	15.67
	2D	8.90	2	-4.23	17.10
LA5	3D	7.55	2	-7.67	15.39
	2D	8.90	2	-5.72	17.36
LA6	3D	7.55	2	-6.76	16.36
	2D	8.90	2	-4.42	17.29
LA7	3D	7.55	2	-7.55	15.68
	2D	8.90	2	-3.83	16.96
LA8	3D	7.55	2	-6.16	15.67
	2D	8.90	2	-4.18	17.00
LA9	3D	7.55	2	-6.38	15.15
	2D	8.90	2	-4.12	16.53
Avg.	3D	7.55	2	-7.46	15.91
	2D	8.90	2	-4.46	16.64

Table B.13: Velocity measurements for bursts LB1 to LB9, including the average over all the bursts.

Test	ADV	x (m)	z_m (cm)	$\overline{U}$ (cm/s)	σ_u (cm/s)
LB1	3D	7.55	2	-6.91	17.95
	2D	8.90	2	-5.78	16.83
LB2	3D	7.55	2	-5.81	17.21
	2D	8.90	2	-5.03	17.18
LB3	3D	7.55	2	-5.11	17.13
	2D	8.90	2	-4.73	17.91
LB4	3D	7.55	2	-6.66	17.52
	2D	8.90	2	-4.91	18.16
LB5	3D	7.55	2	-7.04	18.38
	2D	8.90	2	-5.14	18.15
LB6	3D	7.55	2	-6.87	18.55
	2D	8.90	2	-5.15	18.12
LB7	3D	7.55	2	-6.02	18.00
	2D	8.90	2	-5.13	17.76
LB8	3D	7.55	2	-6.44	18.05
	2D	8.90	2	-4.42	17.63
LB9	3D	7.55	2	-6.18	17.66
	2D	8.90	2	-5.49	17.94
Avg.	3D	7.55	2	-6.34	17.83
	2D	8.90	2	-5.09	17.74

Table B.14: Velocity measurements for bursts LC1 to LC9, including the average over all the bursts.

Test	ADV	x (m)	z_m (cm)	$\overline{U}$ (cm/s)	σ_u (cm/s)
LC1	3D	7.55	2	-4.27	16.85
	2D	8.90	2	-5.61	18.09
LC2	3D	7.55	2	-4.50	18.19
	2D	8.90	2	-5.64	19.13
LC3	3D	7.55	2	-4.86	17.94
	2D	8.90	2	-5.05	18.91
LC4	3D	7.55	2	-4.28	17.84
	2D	8.90	2	-4.63	18.70
LC5	3D	7.55	2	-4.59	18.36
	2D	8.90	2	-5.11	18.53
LC6	3D	7.55	2	-5.86	19.04
	2D	8.90	2	-5.39	18.68
LC7	3D	7.55	2	-5.58	19.82
	2D	8.90	2	-4.84	18.86
LC8	3D	7.55	2	-5.96	19.62
	2D	8.90	2	-4.37	18.51
LC9	3D	7.55	2	-5.15	18.83
	2D	8.90	2	-5.42	18.21
Avg.	3D	7.55	2	-5.00	18.50
	2D	8.90	2	-5.12	18.63

Table B.15: Velocity measurements for bursts LD1 to LD6, including the average over all the bursts.

Test	ADV	x (m)	z_m (cm)	$\overline{U}$ (cm/s)	σ_u (cm/s)
LD1	3D	7.55	2	-5.07	17.90
	2D	8.90	2	-5.24	20.48
LD2	3D	7.55	2	-5.19	19.05
	2D	8.90	2	-6.13	19.52
LD3	3D	7.55	2	-4.62	17.98
	2D	8.90	2	-6.33	19.89
LD4	3D	7.55	2	-5.78	18.71
	2D	8.90	2	-6.07	19.20
LD5	3D	7.55	2	-5.75	19.20
	2D	8.90	2	-5.64	20.85
LD6	3D	7.55	2	-6.00	18.51
	2D	8.90	2	-6.50	19.73
Avg.	3D	7.55	2	-5.40	18.56
	2D	8.90	2	-5.99	19.94

Table B.16: Velocity measurements for bursts LE1 to LE11, including the average over all the bursts.

Test	ADV	x (m)	z_m (cm)	$\overline{U}$ (cm/s)	σ_u (cm/s)
LE1	3D	7.55	2	-6.78	15.70
	2D	8.90	2	-5.32	16.61
LE2	3D	7.55	2	-6.99	17.17
	2D	8.90	2	-4.63	16.42
LE3	3D	7.55	2	-6.06	17.07
	2D	8.90	2	-4.78	16.81
LE4	3D	7.55	2	-6.00	17.18
	2D	8.90	2	-4.71	16.72
LE5	3D	7.55	2	-6.66	16.79
	2D	8.90	2	-5.13	17.24
LE6	3D	7.55	2	-6.55	16.71
	2D	8.90	2	-4.99	17.21
LE7	3D	7.55	2	-6.09	16.84
	2D	8.90	2	-4.71	17.02
LE8	3D	7.55	2	-6.72	17.00
	2D	8.90	2	-5.44	17.08
LE9	3D	7.55	2	-6.84	16.96
	2D	8.90	2	-4.56	17.18
LE10	3D	7.55	2	-6.60	16.76
	2D	8.90	2	-5.04	17.71
LE11	3D	7.55	2	-5.77	16.93
	2D	8.90	2	-5.15	17.97
Avg.	3D	7.55	2	-6.46	16.83
	2D	8.90	2	-4.95	17.09

Table B.17: Velocity measurements for bursts LF1 to LF11, including the average over all the bursts.

Test	ADV	x (m)	z_m (cm)	$\overline{U}$ (cm/s)	σ_u (cm/s)
LF1	3D	7.55	2	-6.06	15.72
	2D	8.90	2	-3.20	18.02
LF2	3D	7.55	2	-6.48	15.87
	2D	8.90	2	-3.83	18.38
LF3	3D	7.55	2	-6.40	15.67
	2D	8.90	2	-3.90	17.59
LF4	3D	7.55	2	-6.93	15.95
	2D	8.90	2	-4.17	17.49
LF5	3D	7.55	2	-6.52	15.92
	2D	8.90	2	-3.53	17.55
LF6	3D	7.55	2	-7.16	16.23
	2D	8.90	2	-4.18	17.68
LF7	3D	7.55	2	-7.04	15.95
	2D	8.90	2	-4.39	17.55
LF8	3D	7.55	2	-7.08	16.19
	2D	8.90	2	-3.85	17.44
LF9	3D	7.55	2	NR	NR
	2D	8.90	2	-3.72	17.08
LF10	3D	7.55	2	-6.26	15.60
	2D	8.90	2	-3.29	17.43
LF11	3D	7.55	2	-5.96	15.57
	2D	8.90	2	-2.90	17.71
Avg.	3D	7.55	2	-6.59	15.87
	2D	8.90	2	-3.72	17.63

Table B.18: Concentration measurements for bursts LA1 to LA9, including the average over all the bursts.

Test	Sensor	x (cm)	z_m (cm)	$\overline{C}$	σ_c	γ_{uc}
LA1	C1	7.55	2	0.0039	0.0015	0.060
	C2	8.90	2	0.0039	0.0013	0.161
LA2	C1	7.55	2	0.0017	0.0024	0.426
	C2	8.90	2	0.0017	0.0012	0.226
LA3	C1	7.55	2	0.0018	0.0022	0.348
	C2	8.90	2	0.0018	0.0003	0.259
LA4	C1	7.55	2	0.0030	0.0016	0.148
	C2	8.90	2	0.0030	0.0008	0.287
LA5	C1	7.55	2	0.0027	0.0017	0.232
	C2	8.90	2	0.0027	0.0012	0.242
LA6	C1	7.55	2	0.0032	0.001	0.071
	C2	8.90	2	0.0032	0.0013	0.272
LA7	C1	7.55	2	0.0024	0.0014	0.183
	C2	8.90	2	0.0024	0.0007	0.213
LA8	C1	7.55	2	0.0025	0.0012	0.132
	C2	8.90	2	0.0025	0.0008	0.154
LA9	C1	7.55	2	0.0022	0.0014	0.188
	C2	8.90	2	0.0022	0.0008	0.215
Avg	C1	7.55	2	0.0026	0.0016	0.198
	C2	8.90	2	0.0026	0.0009	0.225

Table B.19: Concentration measurements for bursts LB1 to LB9, including the average over all the bursts.

Test	Sensor	x (cm)	z_m (cm)	$\overline{C}$	σ_c	γ_{uc}
LB1	C1	7.55	2	0.0016	0.0009	0.094
	C2	8.90	2	0.0016	0.0009	0.193
LB2	C1	7.55	2	0.0020	0.0013	0.133
	C2	8.90	2	0.0020	0.0009	0.211
LB3	C1	7.55	2	0.0024	0.0010	0.088
	C2	8.90	2	0.0024	0.0012	0.215
LB4	C1	7.55	2	0.0021	0.0007	0.072
	C2	8.90	2	0.0021	0.0012	0.148
LB5	C1	7.55	2	0.0019	0.0007	0.072
	C2	8.90	2	0.0019	0.0011	0.135
LB6	C1	7.55	2	0.0022	0.0009	0.086
	C2	8.90	2	0.0022	0.0011	0.169
LB7	C1	7.55	2	0.0022	0.0008	0.086
	C2	8.90	2	0.0022	0.0011	0.163
LB8	C1	7.55	2	0.0022	0.0009	0.099
	C2	8.90	2	0.0022	0.0013	0.133
LB9	C1	7.55	2	0.0021	0.0008	0.065
	C2	8.90	2	0.0021	0.0011	0.167
Avg.	C1	7.55	2	0.0021	0.0009	0.088
	C2	8.90	2	0.0021	0.0011	0.171

Table B.20: Concentration measurements for bursts LC1 to LC9, including the average over all the bursts.

Test	Sensor	x (cm)	z_m (cm)	$\overline{C}$	σ_c	γ_{uc}
LC1	C1	7.55	2	0.0010	0.0006	0.139
	C2	8.90	2	0.0010	0.0008	0.168
LC2	C1	7.55	2	0.0013	0.0007	0.122
	C2	8.90	2	0.0013	0.0009	0.190
LC3	C1	7.55	2	0.0015	0.0008	0.118
	C2	8.90	2	0.0015	0.0009	0.198
LC4	C1	7.55	2	0.0015	0.0007	0.110
	C2	8.90	2	0.0015	0.0009	0.161
LC5	C1	7.55	2	0.0017	0.0008	0.108
	C2	8.90	2	0.0017	0.0010	0.161
LC6	C1	7.55	2	0.0019	0.0010	0.122
	C2	8.90	2	0.0019	0.0011	0.191
LC7	C1	7.55	2	0.0018	0.0008	0.119
	C2	8.90	2	0.0018	0.0011	0.176
LC8	C1	7.55	2	0.0017	0.0006	0.095
	C2	8.90	2	0.0017	0.0013	0.061
LC9	C1	7.55	2	0.0019	0.0009	0.109
	C2	8.90	2	0.0019	0.0012	0.128
Avg.	C1	7.55	2	0.0016	0.0008	0.116
	C2	8.90	2	0.0016	0.0010	0.159

Table B.21: Concentration measurements for bursts LD1 to LD6, including the average over all the bursts.

Test	Sensor	x (cm)	z_m (cm)	$\overline{C}$	σ_c	γ_{uc}
LD1	C1	7.55	2	0.0014	0.0011	0.139
	C2	8.90	2	0.0014	0.0012	0.086
LD2	C1	7.55	2	0.0025	0.0018	0.124
	C2	8.90	2	0.0025	0.0016	0.116
LD3	C1	7.55	2	0.0027	0.0013	0.082
	C2	8.90	2	0.0027	0.0015	0.170
LD4	C1	7.55	2	0.0024	0.0011	0.129
	C2	8.90	2	0.0024	0.0009	0.204
LD5	C1	7.55	2	0.0030	0.0012	0.103
	C2	8.90	2	0.0030	0.0015	0.160
LD6	C1	7.55	2	0.0018	0.0010	0.124
	C2	8.90	2	0.0018	0.0012	0.162
Avg.	C1	7.55	2	0.0023	0.0013	0.117
	C2	8.90	2	0.0023	0.0013	0.150

Table B.22: Concentration measurements for bursts LE1 to LE11, including the average over all the bursts.

Test	Sensor	x (cm)	z_m (cm)	$\overline{C}$	σ_c	γ_{uc}
LE1	C1	7.55	2	0.0010	0.0008	0.118
	C2	8.90	2	0.0010	0.0009	0.053
LE2	C1	7.55	2	0.0009	0.0007	0.098
	C2	8.90	2	0.0009	0.0012	0.092
LE3	C1	7.55	2	0.0008	0.0006	0.141
	C2	8.90	2	0.0008	0.0009	0.081
LE4	C1	7.55	2	0.0009	0.0007	0.141
	C2	8.90	2	0.0009	0.0009	0.106
LE5	C1	7.55	2	0.0008	0.0006	0.150
	C2	8.90	2	0.0008	0.0008	0.108
LE6	C1	7.55	2	0.0008	0.0006	0.147
	C2	8.90	2	0.0008	0.0010	0.113
LE7	C1	7.55	2	0.0007	0.0005	0.151
	C2	8.90	2	0.0007	0.0009	0.110
LE8	C1	7.55	2	0.0007	0.0005	0.154
	C2	8.90	2	0.0007	0.0008	0.095
LE9	C1	7.55	2	0.0008	0.0004	0.115
	C2	8.90	2	0.0008	0.0008	0.121
LE10	C1	7.55	2	0.0009	0.0005	0.102
	C2	8.90	2	0.0009	0.0008	0.158
LE11	C1	7.55	2	0.0009	0.0005	0.077
	C2	8.90	2	0.0009	0.0007	0.162
Avg.	C1	7.55	2	0.0008	0.0006	0.127
	C2	8.90	2	0.0008	0.0009	0.109

Table B.23: Concentration measurements for bursts LF1 to LF11, including the average over all the bursts.

Test	Sensor	x (cm)	z_m (cm)	$\overline{C}$	σ_c	γ_{uc}
LF1	C1	7.55	2	0.0007	0.0004	0.128
	C2	8.90	2	0.0007	0.0005	0.163
LF2	C1	7.55	2	0.0007	0.0004	0.067
	C2	8.90	2	0.0007	0.0006	0.083
LF3	C1	7.55	2	0.0007	0.0005	0.077
	C2	8.90	2	0.0007	0.0007	0.064
LF4	C1	7.55	2	0.0007	0.0003	0.067
	C2	8.90	2	0.0007	0.0006	0.049
LF5	C1	7.55	2	0.0007	0.0004	0.067
	C2	8.90	2	0.0007	0.0007	0.064
LF6	C1	7.55	2	0.0007	0.0003	0.055
	C2	8.90	2	0.0007	0.0006	0.088
LF7	C1	7.55	2	0.0006	0.0002	0.080
	C2	8.90	2	0.0006	0.0003	0.140
LF8	C1	7.55	2	0.0006	0.0003	0.088
	C2	8.90	2	0.0006	0.0003	0.181
LF9	C1	7.55	2	0.0007	0.0004	NR
	C2	8.90	2	0.0007	0.0004	0.140
LF10	C1	7.55	2	0.0008	0.0004	0.101
	C2	8.90	2	0.0008	0.0005	0.172
LF11	C1	7.55	2	0.0008	0.0004	0.107
	C2	8.90	2	0.0008	0.0005	0.157
Avg.	C1	7.55	2	0.0007	0.0004	0.084
	C2	8.90	2	0.0007	0.0005	0.118

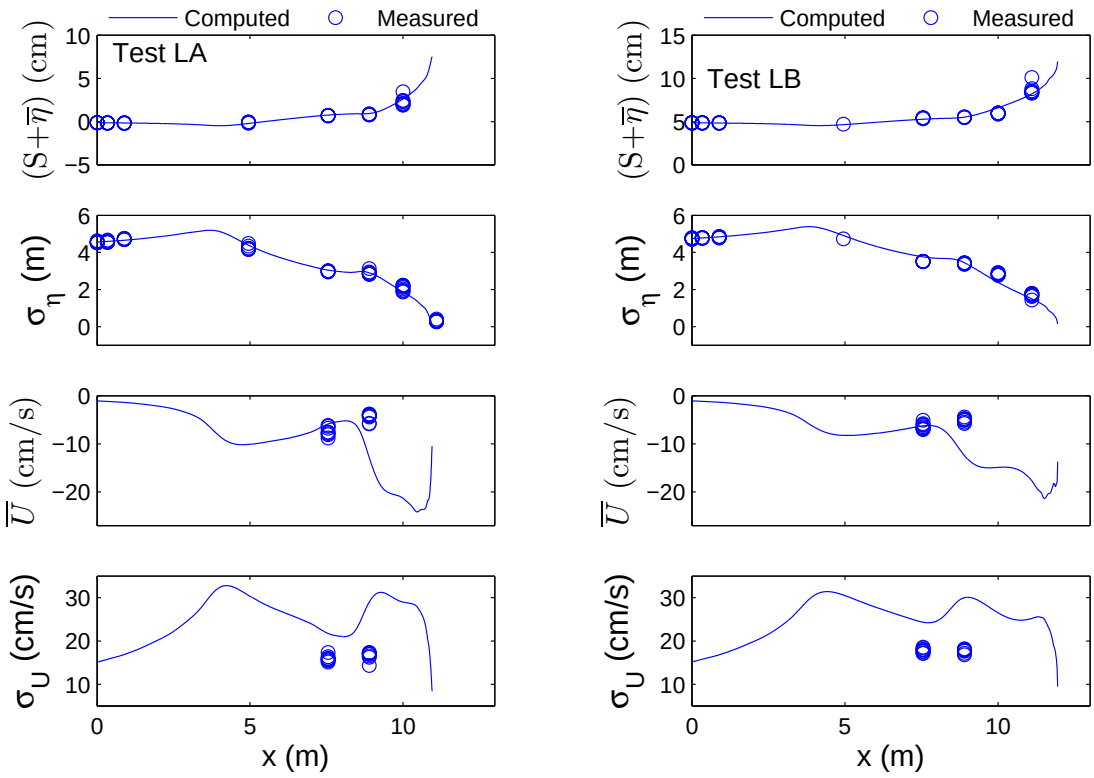

Figure B.1: Cross-shore variations of measured vs. computed $(S + \bar{\eta})$, σ_η, $\bar{U}$ and σ_U for tests LA (left) and LB (right)

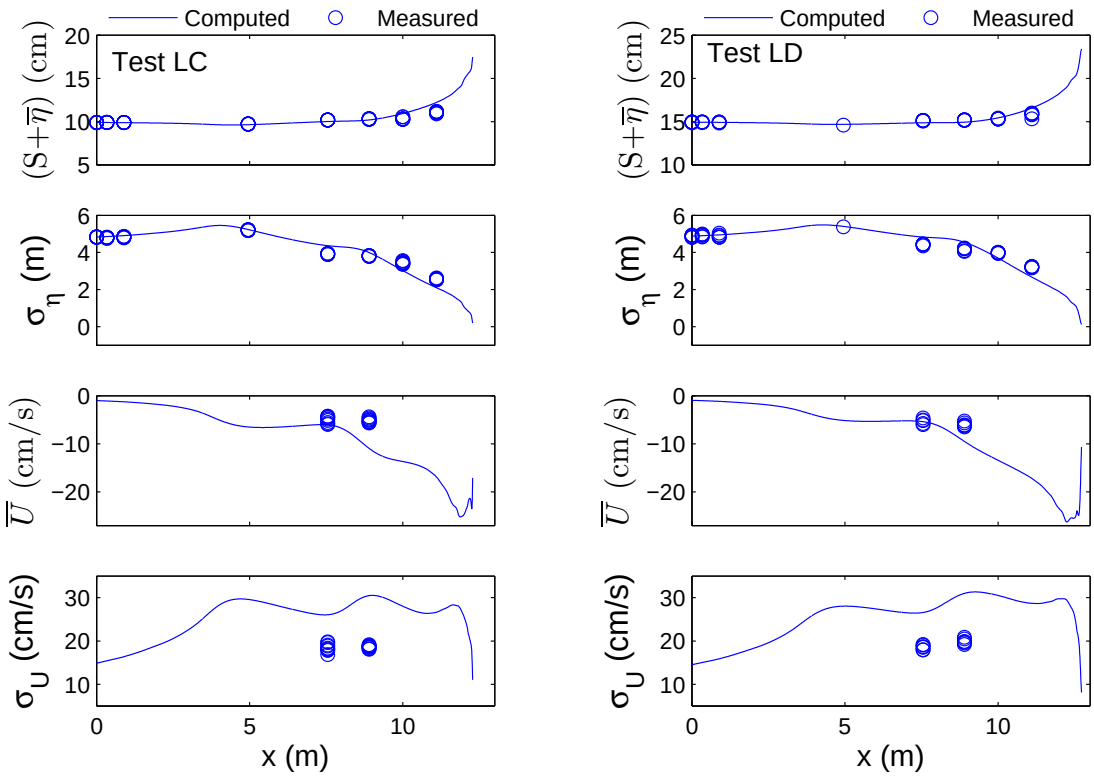

Figure B.2: Cross-shore variations of measured vs. computed $(S + \bar{\eta})$, σ_η, $\bar{U}$ and σ_U for tests LC (left) and LD (right)

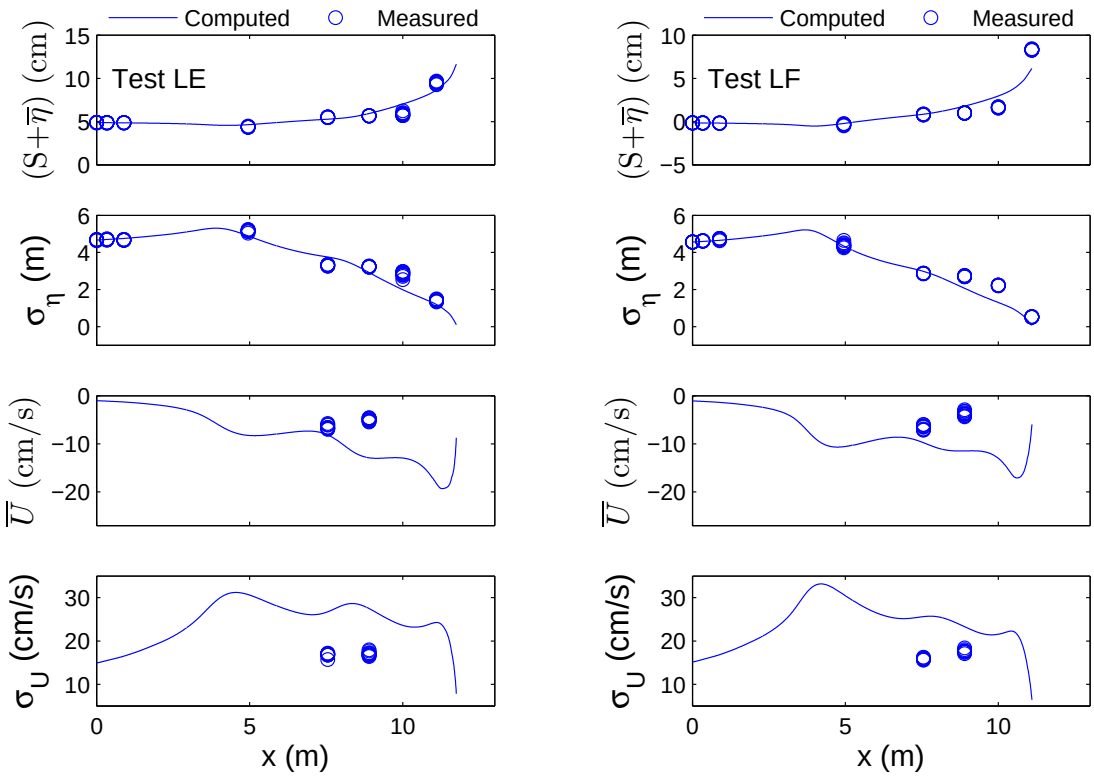

Figure B.3: Cross-shore variations of measured vs. computed $(S + \bar{\eta})$, σ_η, $\bar{U}$ and σ_U for tests LE (left) and LF (right)

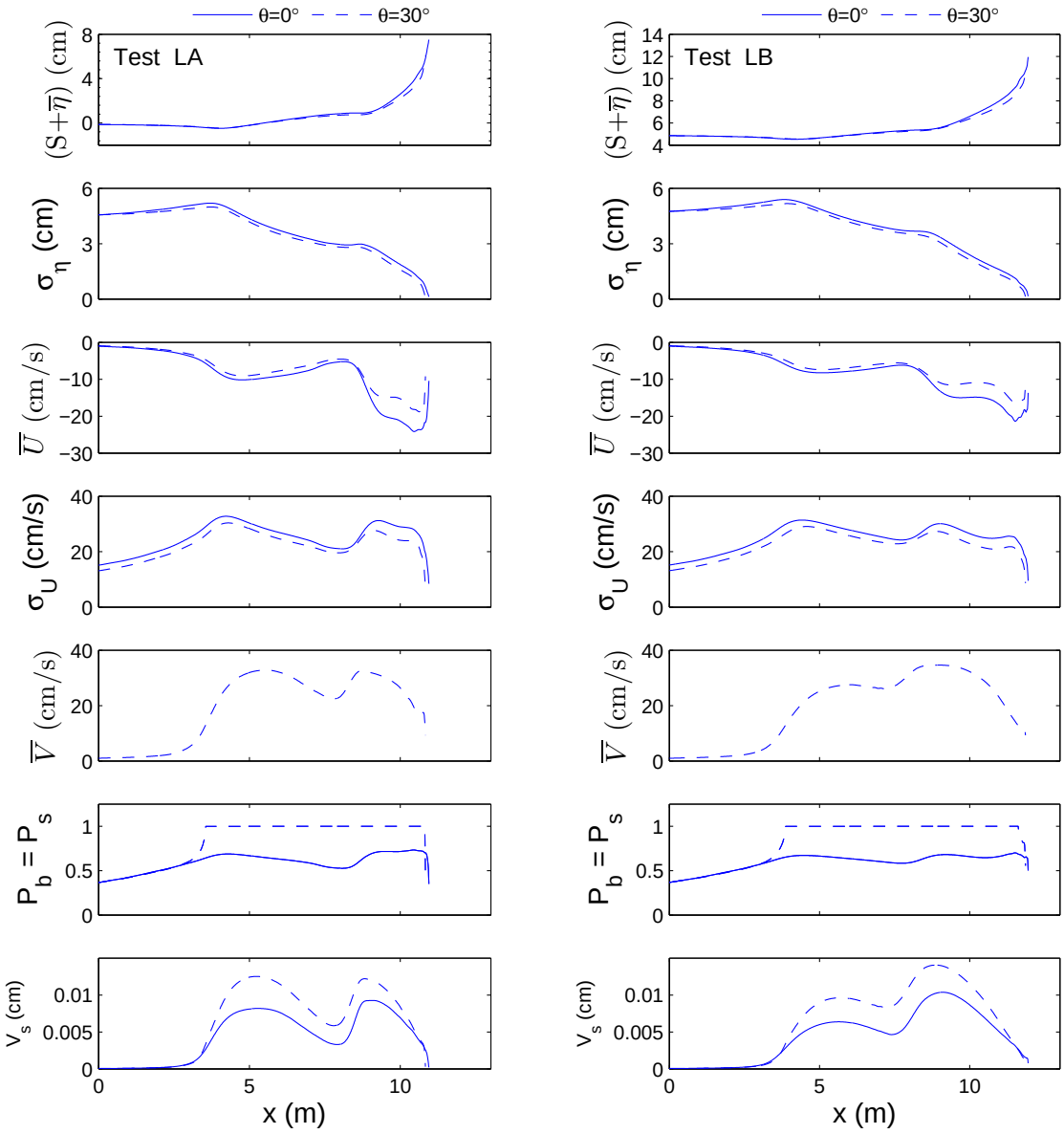

Figure B.4: Cross-shore variations of $(S + \bar{\eta})$, σ_η, $\bar{U}$, σ_U, $\bar{V}$, $P_b = P_s$ and V_s for $\theta = 0°$ and $\theta = 30°$ for tests LA (left) and LB (right)

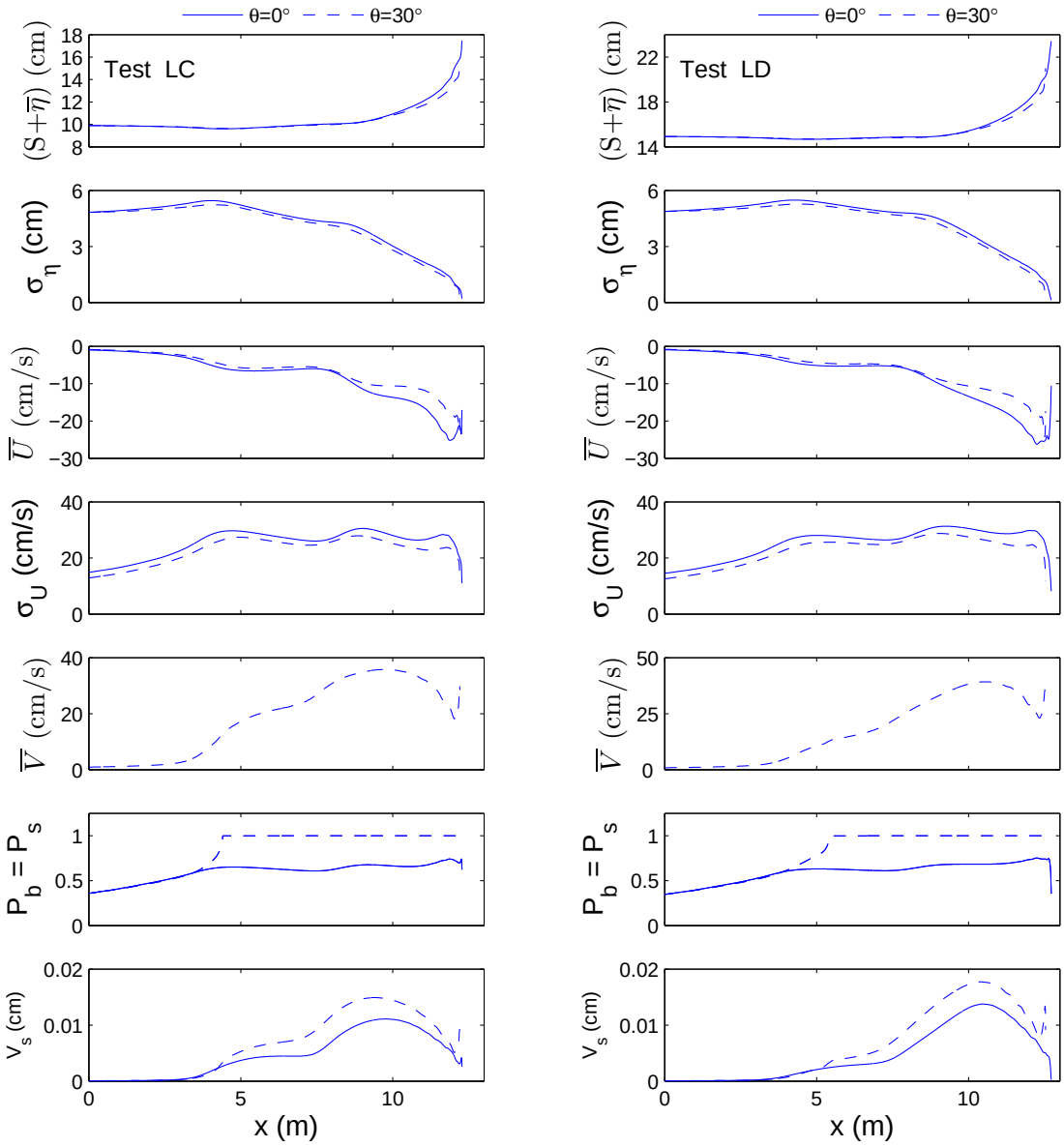

Figure B.5: Cross-shore variations of $(S + \bar{\eta})$, σ_η, $\bar{U}$, σ_U, $\bar{V}$, $P_b = P_s$ and V_s for $\theta = 0°$ and $\theta = 30°$ for tests LC (left) and LD (right)

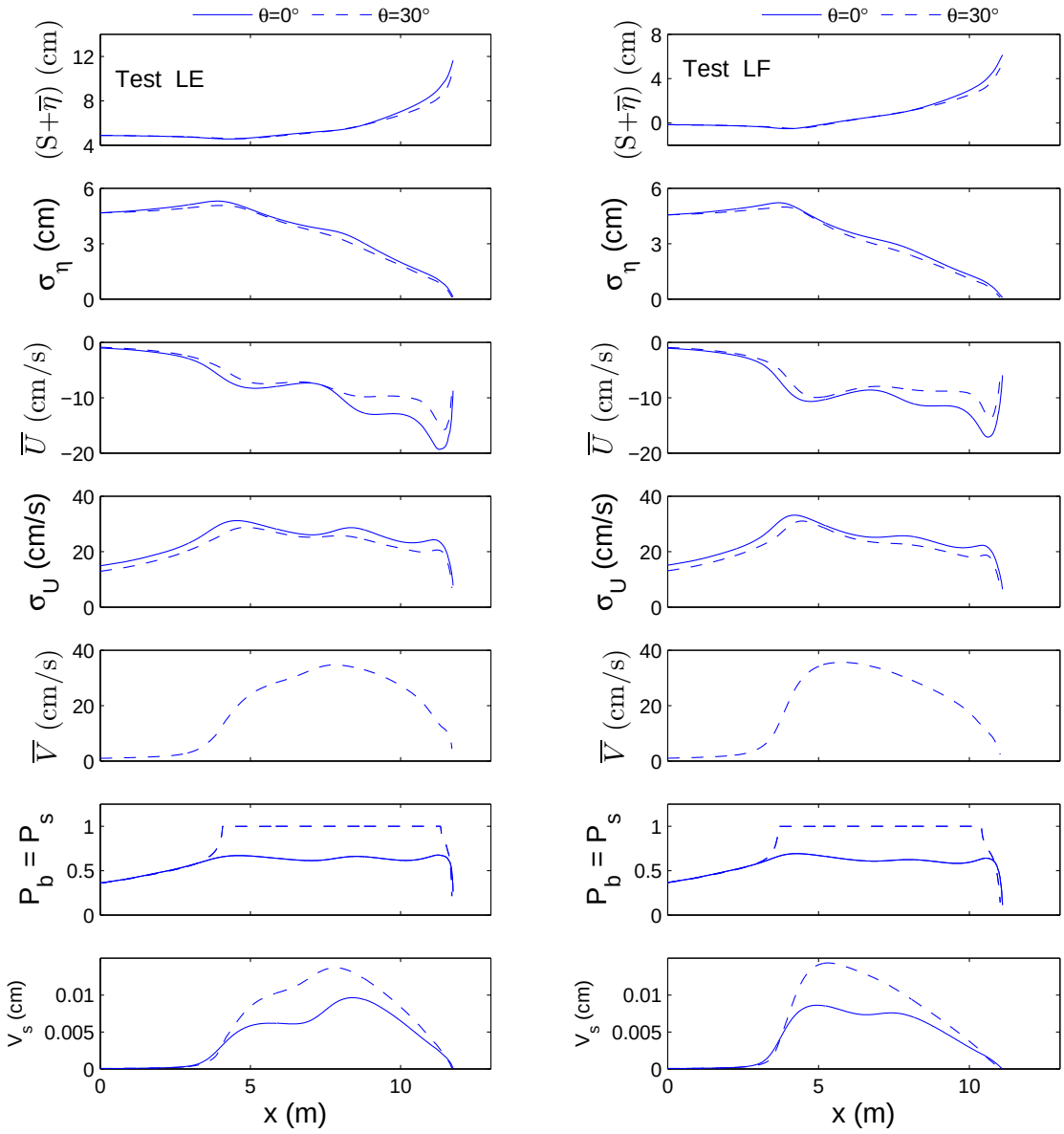

Figure B.6: Cross-shore variations of $(S + \bar{\eta})$, σ_η, $\bar{U}$, σ_U, $\bar{V}$, $P_b = P_s$ and V_s for $\theta = 0°$ and $\theta = 30°$ for tests LE (left) and LF (right)

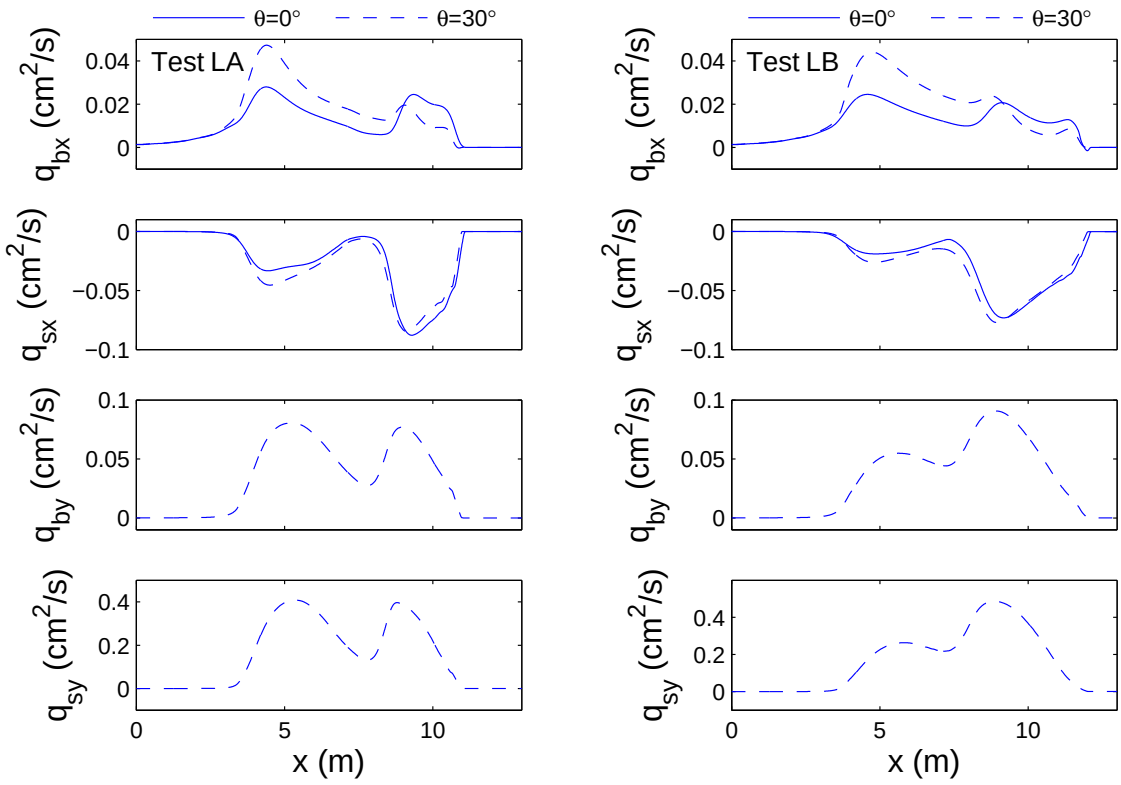

Figure B.7: Cross-shore variations of q_{bx}, q_{sx}, q_{by} and q_{sy} for $\theta = 0°$ and $\theta = 30°$ in tests LA (left) and LB (right).

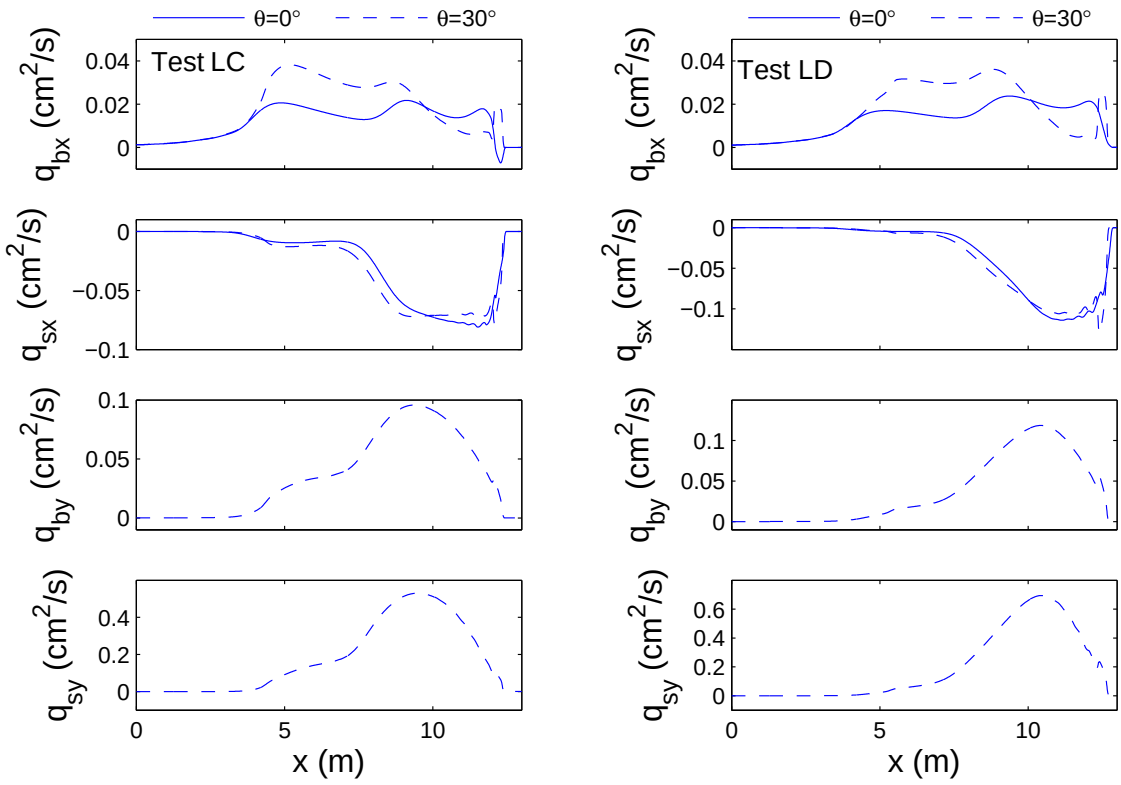

Figure B.8: Cross-shore variations of q_{bx}, q_{sx}, q_{by} and q_{sy} for $\theta = 0°$ and $\theta = 30°$ in tests LC (left) and LD (right).

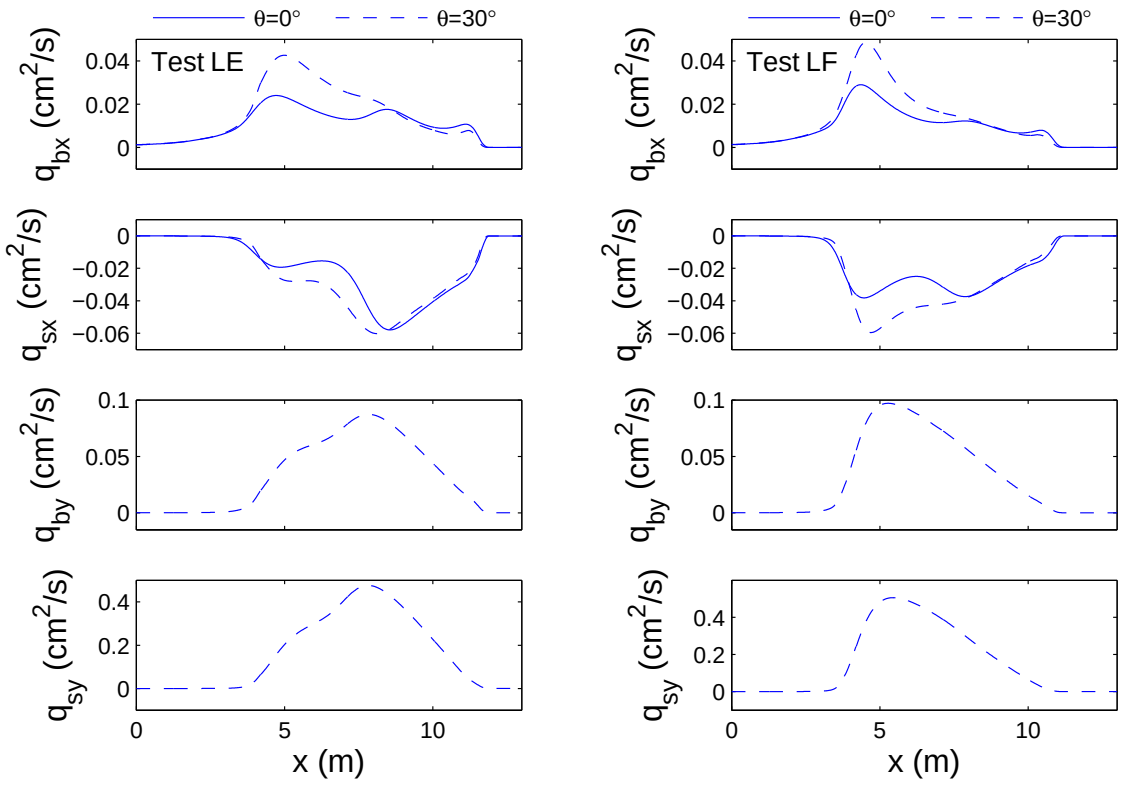

Figure B.9: Cross-shore variations of q_{bx}, q_{sx}, q_{by} and q_{sy} for $\theta = 0°$ and $\theta = 30°$ in tests LE (left) and LF (right).

Appendix C

LARGE SCALE TESTS

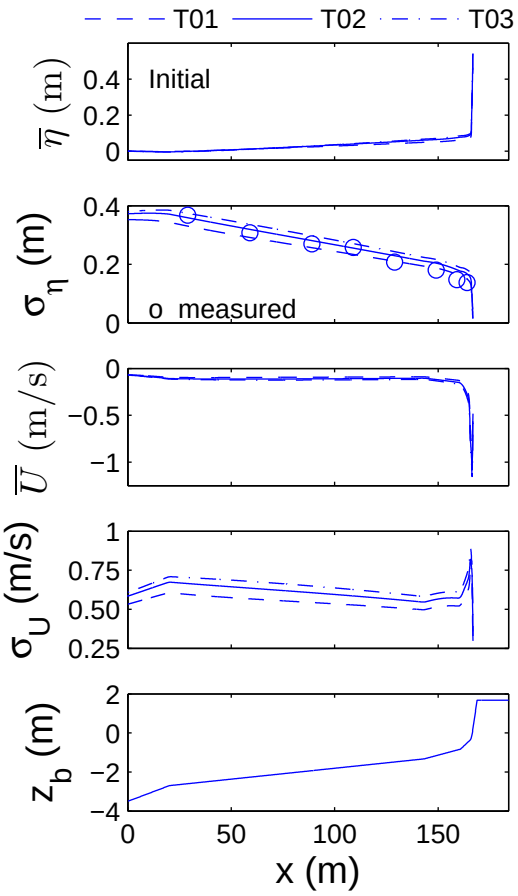

Figure C.1: Cross-shore variations of computed $(S + \bar{\eta})$, σ_η, $\bar{U}$ and σ_U for T01I, T02I and T03I ($t = 0$ s).

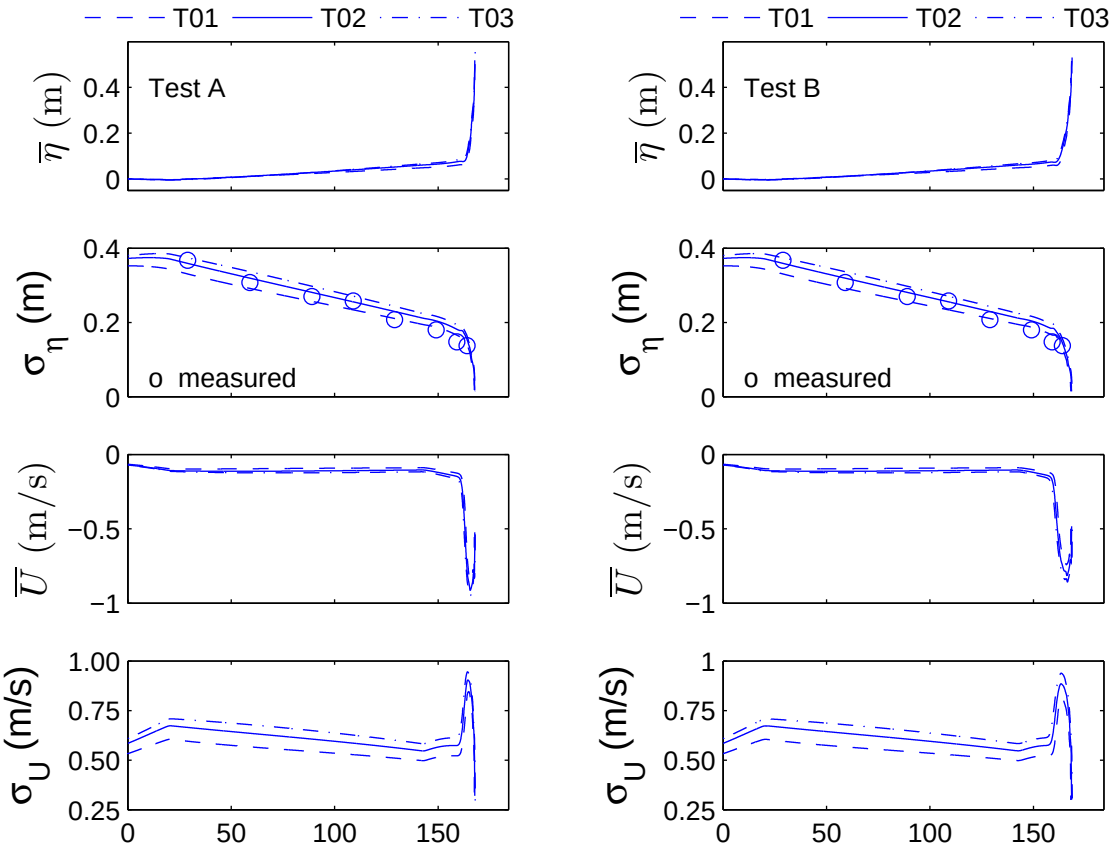

Figure C.2: Cross-shore variations of computed $(S + \bar{\eta})$, σ_η, $\bar{U}$ and σ_U for T01A, T02A and T03A (left) and T01B, T02B and T03B (right).

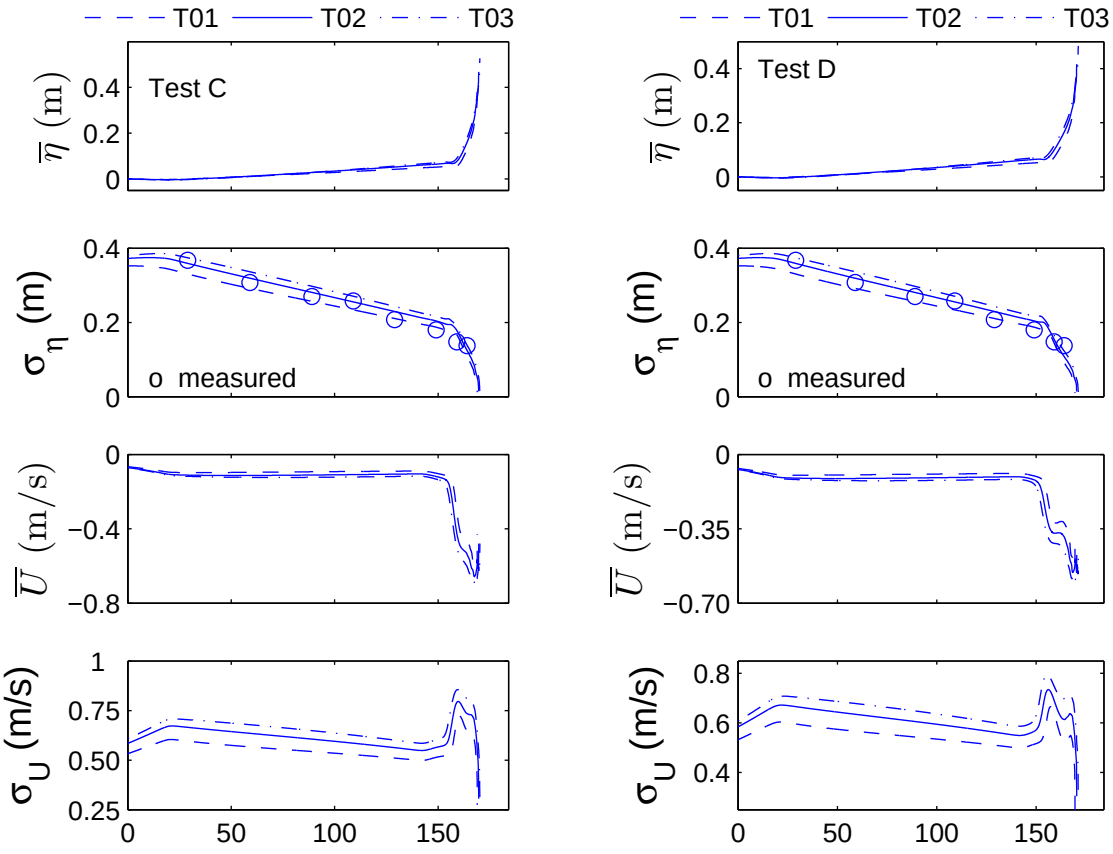

Figure C.3: Cross-shore variations of computed $(S + \bar{\eta})$, σ_η, $\bar{U}$ and σ_U for T01C, T02C and T03C (left) and T01D, T02D and T03D (right).

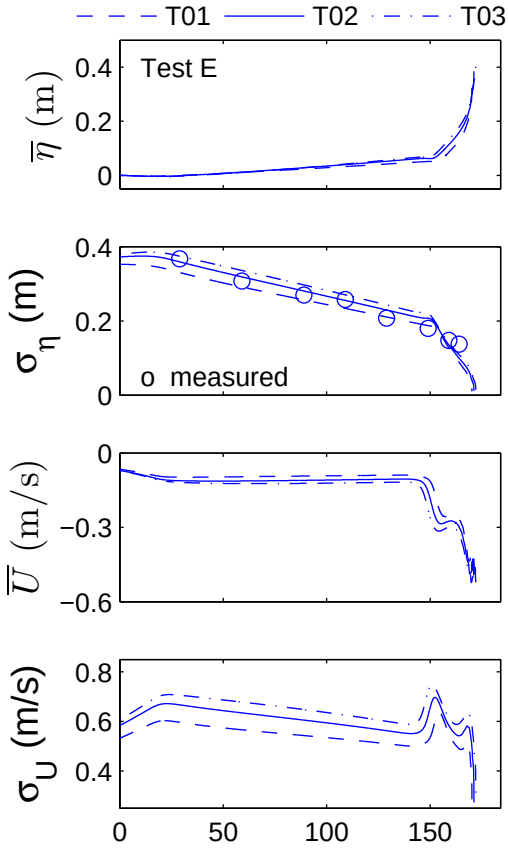

Figure C.4: Cross-shore variations of computed $(S + \bar{\eta})$, σ_η, $\bar{U}$ and σ_U for T01E, T02E and T03E.

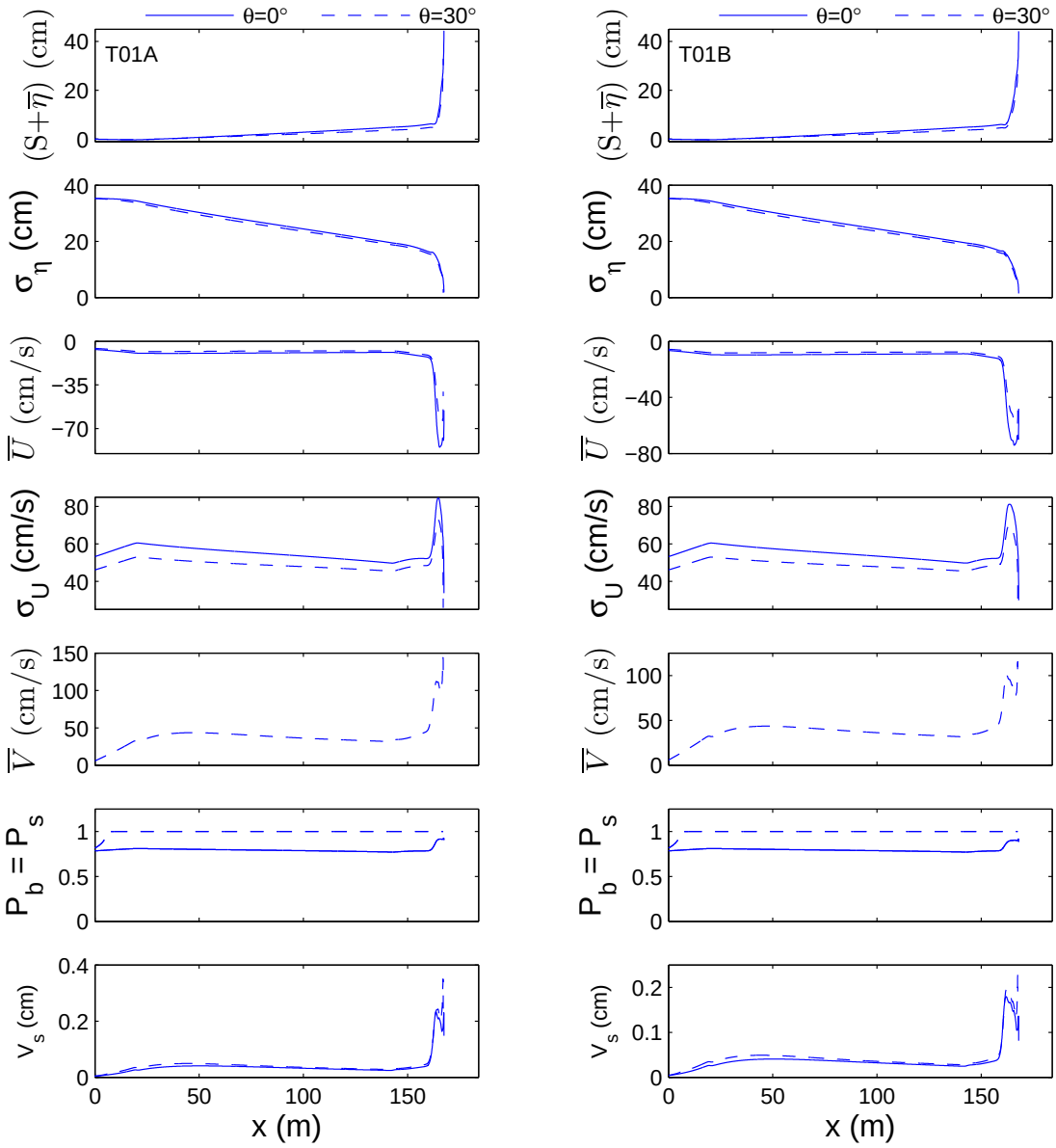

Figure C.5: Cross-shore variations of $(S + \bar{\eta})$, σ_η, $\bar{U}$, σ_U, $\bar{V}$, $P_b = P_s$ and V_s for $\theta = 0°$ and $\theta = 30°$ for tests T01A (left) and T01B (right)

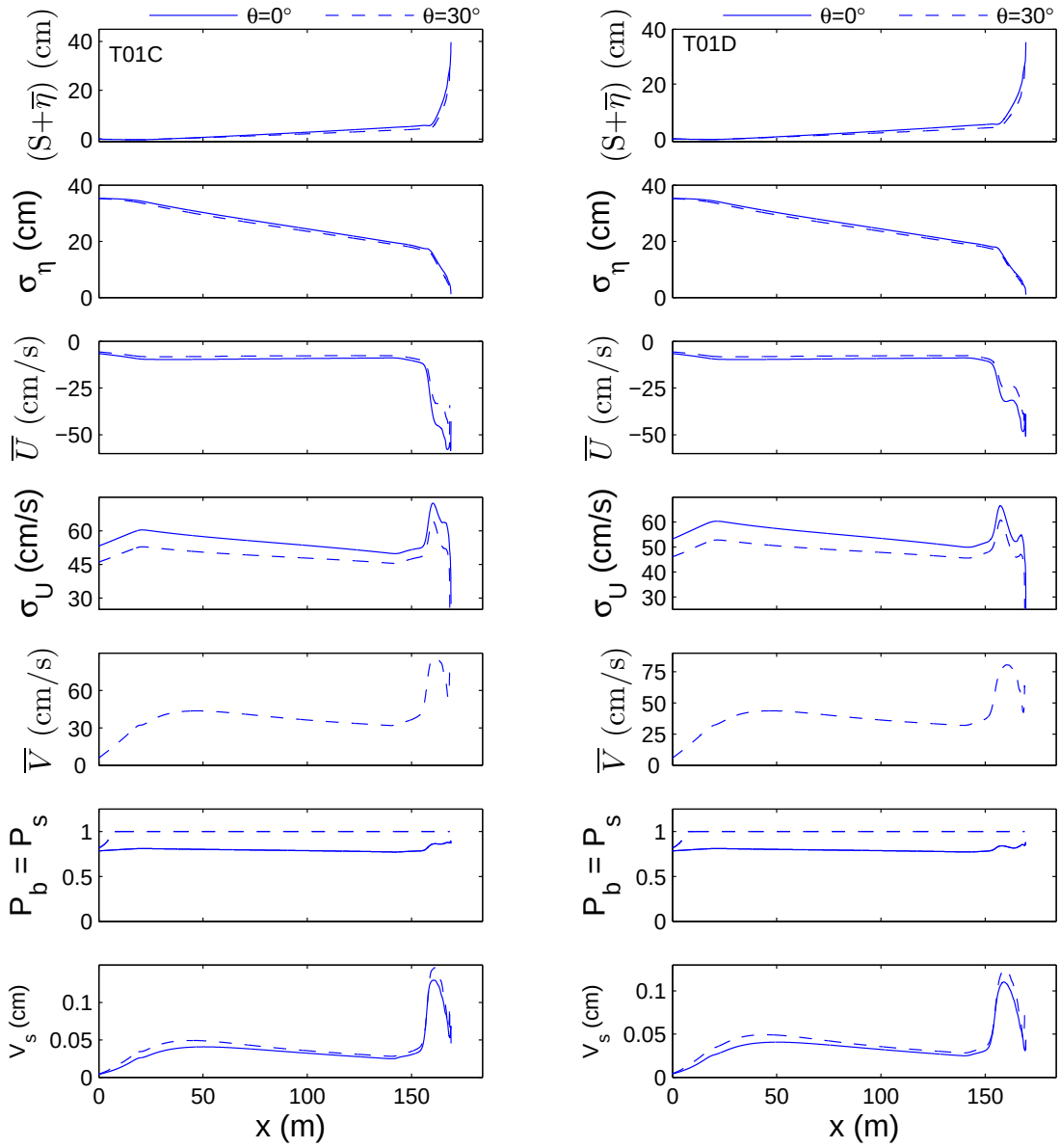

Figure C.6: Cross-shore variations of $(S + \bar{\eta})$, σ_η, $\bar{U}$, σ_U, $\bar{V}$, $P_b = P_s$ and V_s for $\theta = 0°$ and $\theta = 30°$ for tests T01C (left) and T01D (right)

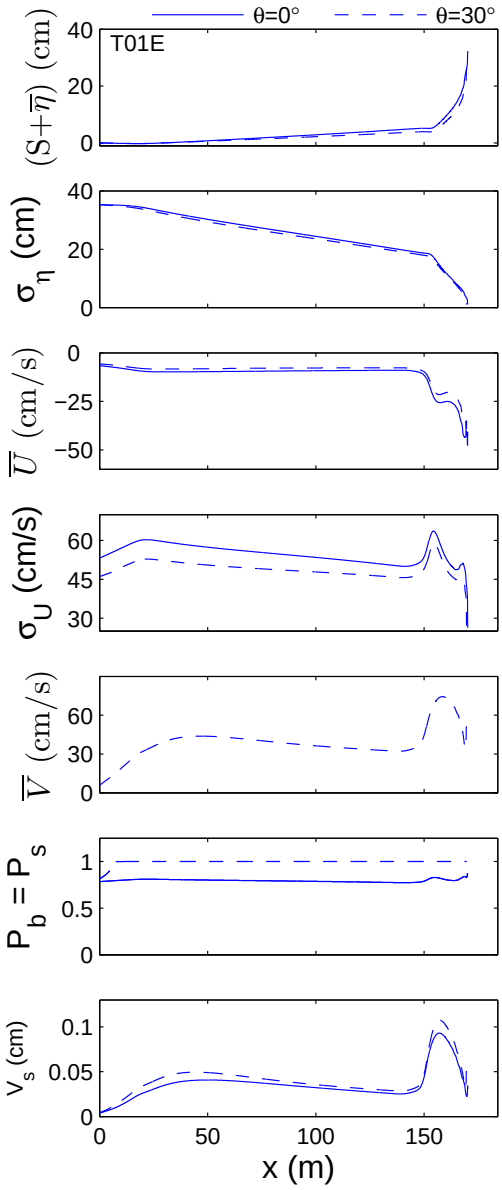

Figure C.7: Cross-shore variations of $(S + \bar{\eta})$, σ_η, $\bar{U}$, σ_U, $\bar{V}$, $P_b = P_s$ and V_s for $\theta = 0^\circ$ and $\theta = 30^\circ$ for test T01E

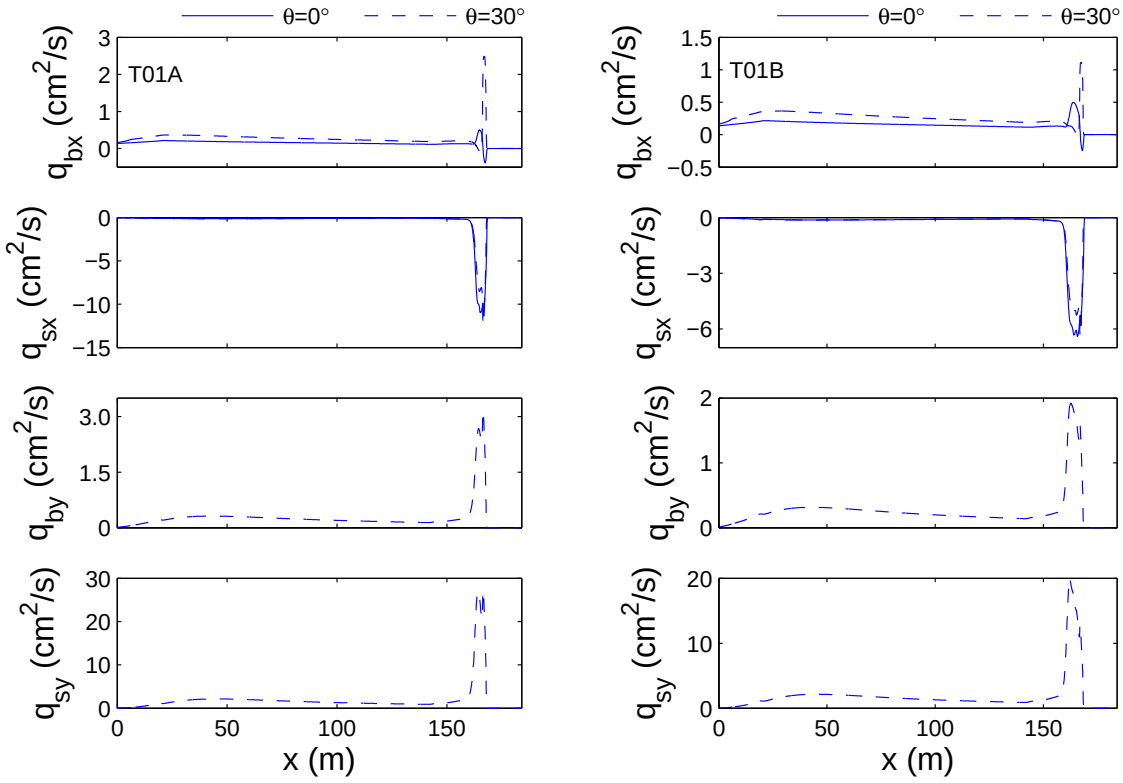

Figure C.8: Cross-shore variations of q_{bx}, q_{sx}, q_{by} and q_{sy} for $\theta = 0°$ and $\theta = 30°$ in tests T01A (left) and T01B (right).

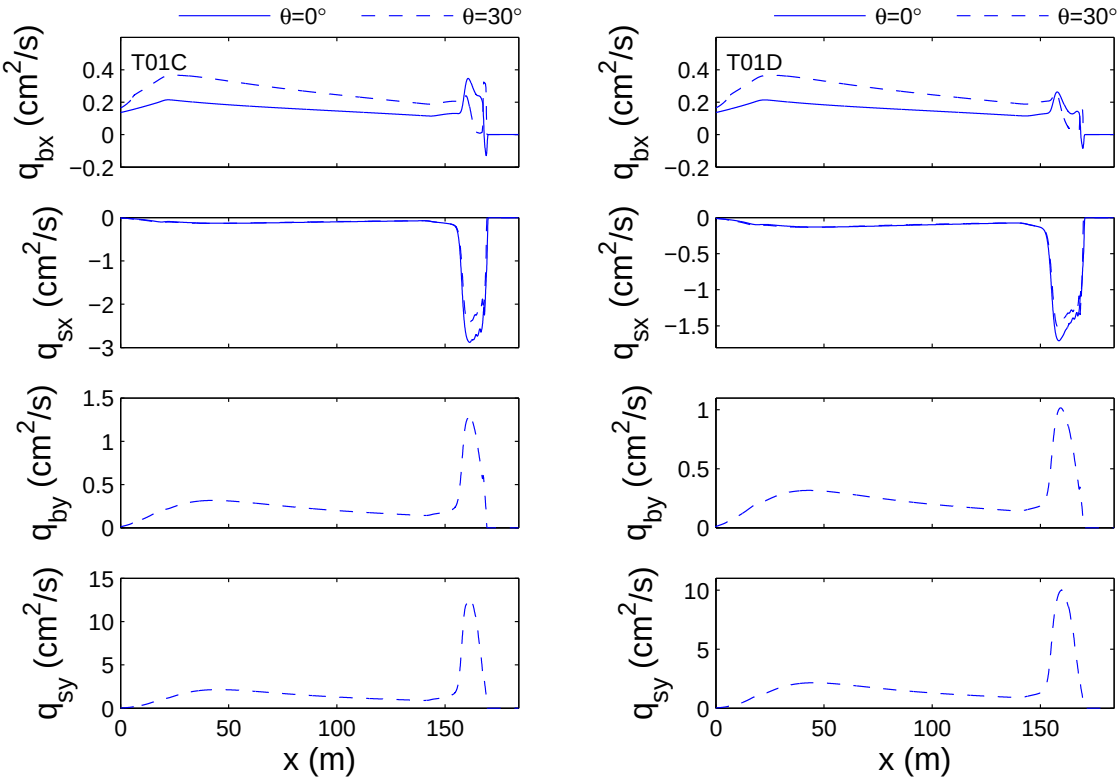

Figure C.9: Cross-shore variations of q_{bx}, q_{sx}, q_{by} and q_{sy} for $\theta = 0°$ and $\theta = 30°$ in tests T01C (left) and T01D (right).

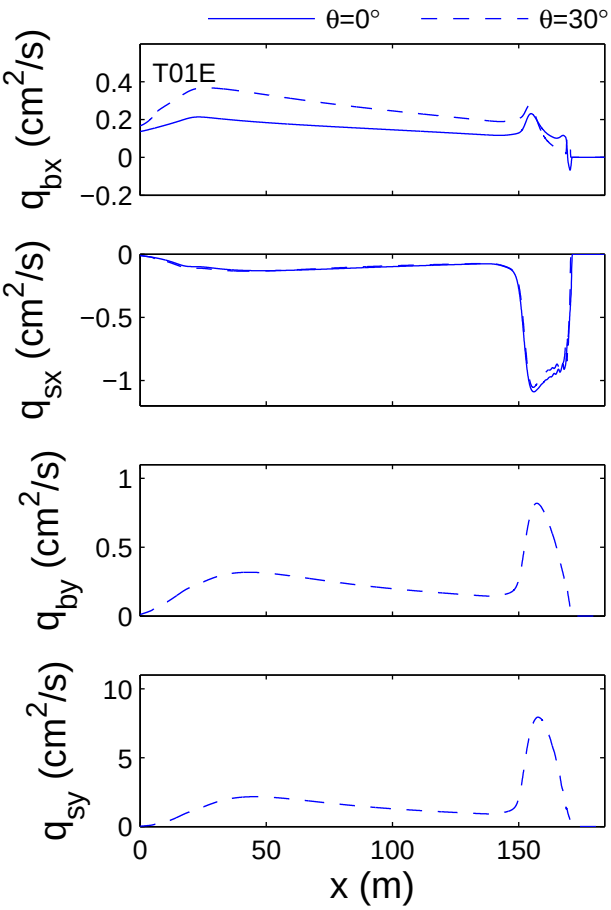

Figure C.10:

Figure C.11: Cross-shore variations of q_{bx}, q_{sx}, q_{by} and q_{sy} for $\theta = 0°$ and $\theta = 30°$ in test T01E.

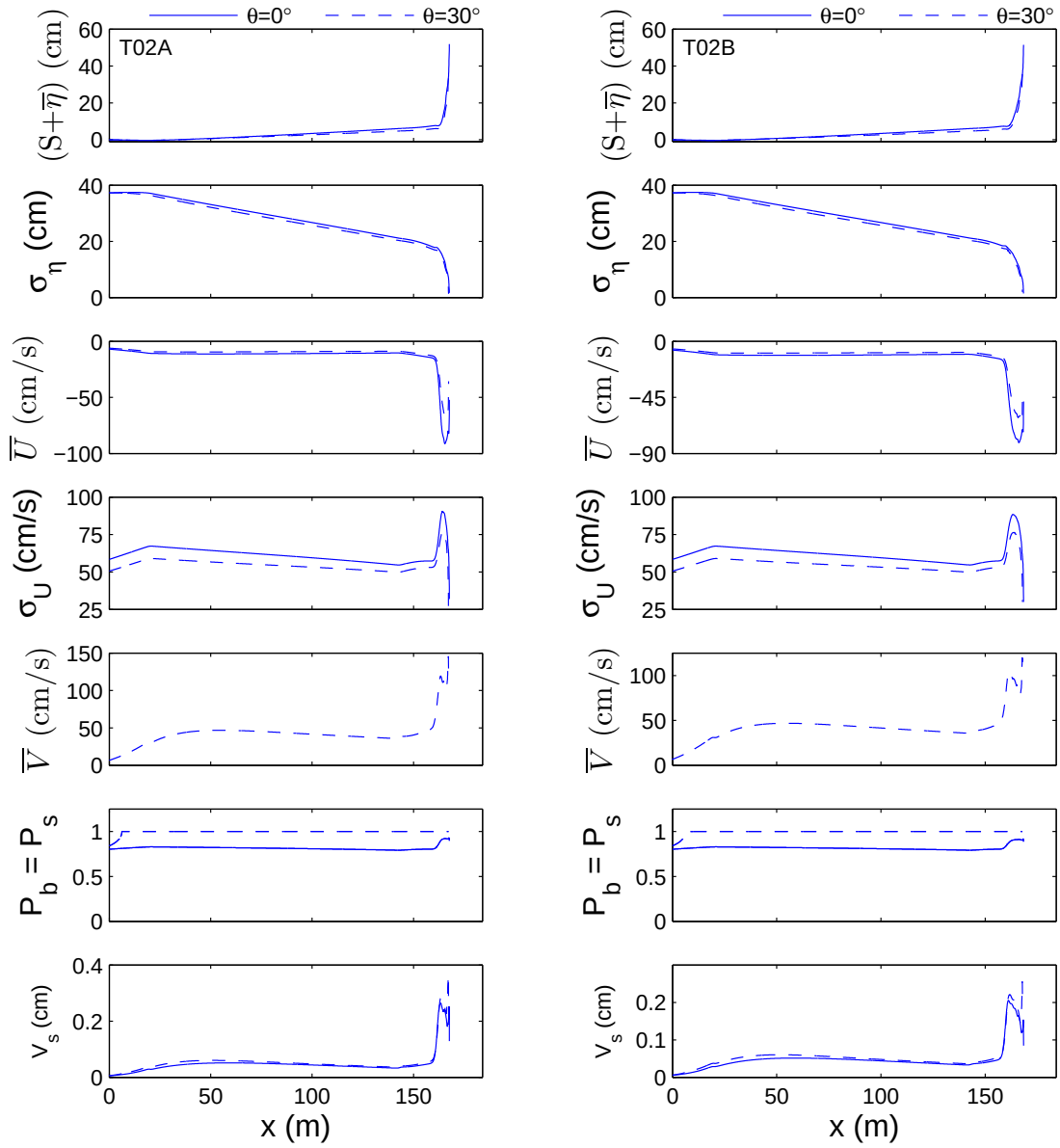

Figure C.12: Cross-shore variations of $(S + \bar{\eta})$, σ_η, $\bar{U}$, σ_U, $\bar{V}$, $P_b = P_s$ and V_s for $\theta = 0°$ and $\theta = 30°$ for tests T02A (left) and T02B (right)

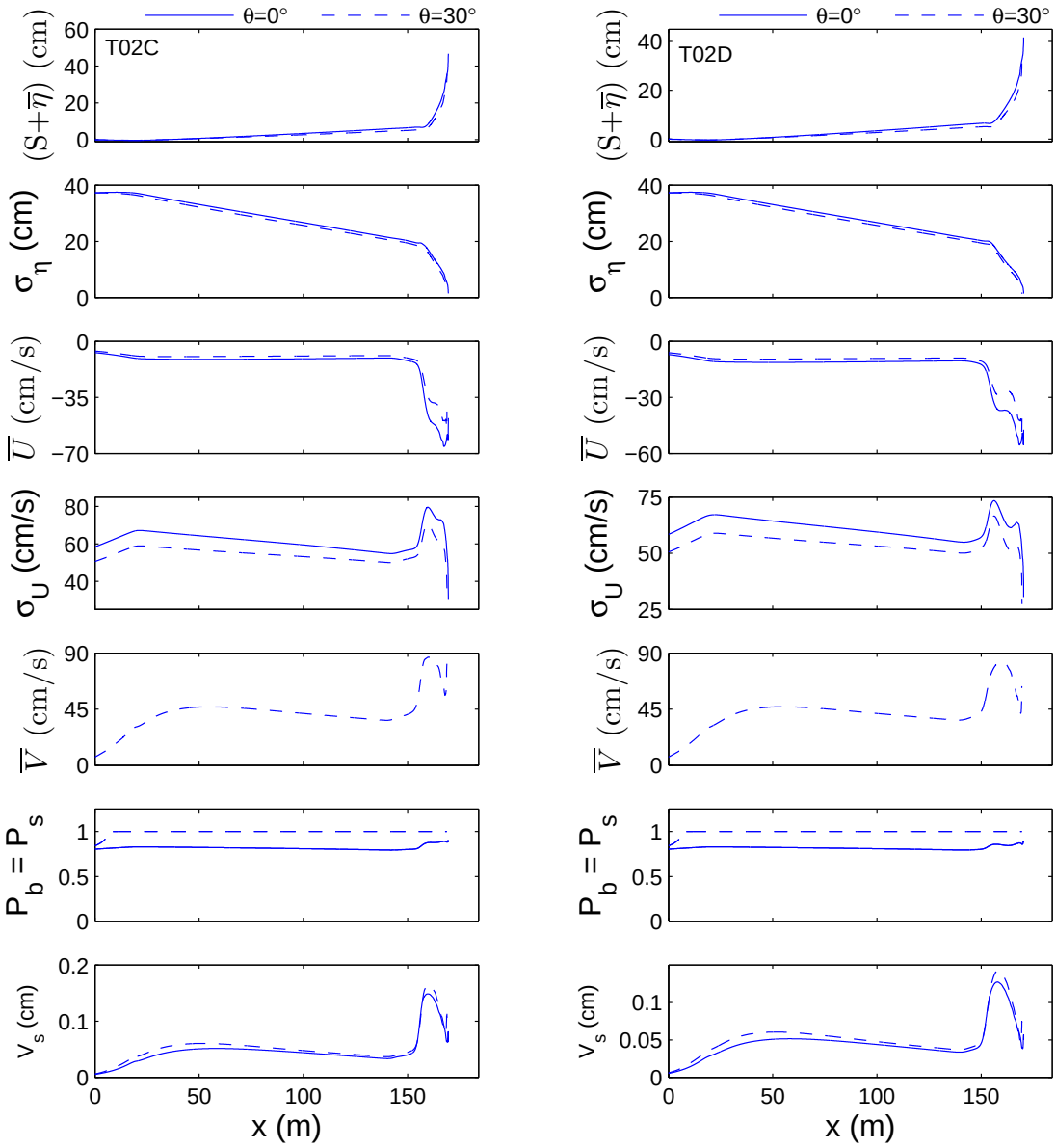

Figure C.13: Cross-shore variations of $(S + \bar{\eta})$, σ_η, $\bar{U}$, σ_U, $\bar{V}$, $P_b = P_s$ and V_s for $\theta = 0°$ and $\theta = 30°$ for tests T02C (left) and T02D (right)

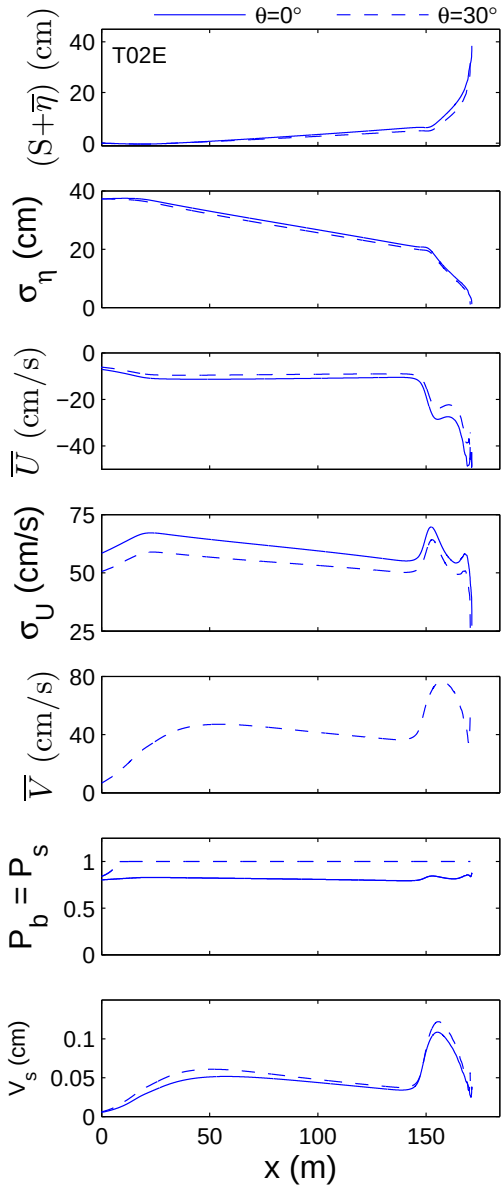

Figure C.14: Cross-shore variations of $(S + \bar{\eta})$, σ_η, $\bar{U}$, σ_U, $\bar{V}$, $P_b = P_s$ and V_s for $\theta = 0°$ and $\theta = 30°$ for test T02E

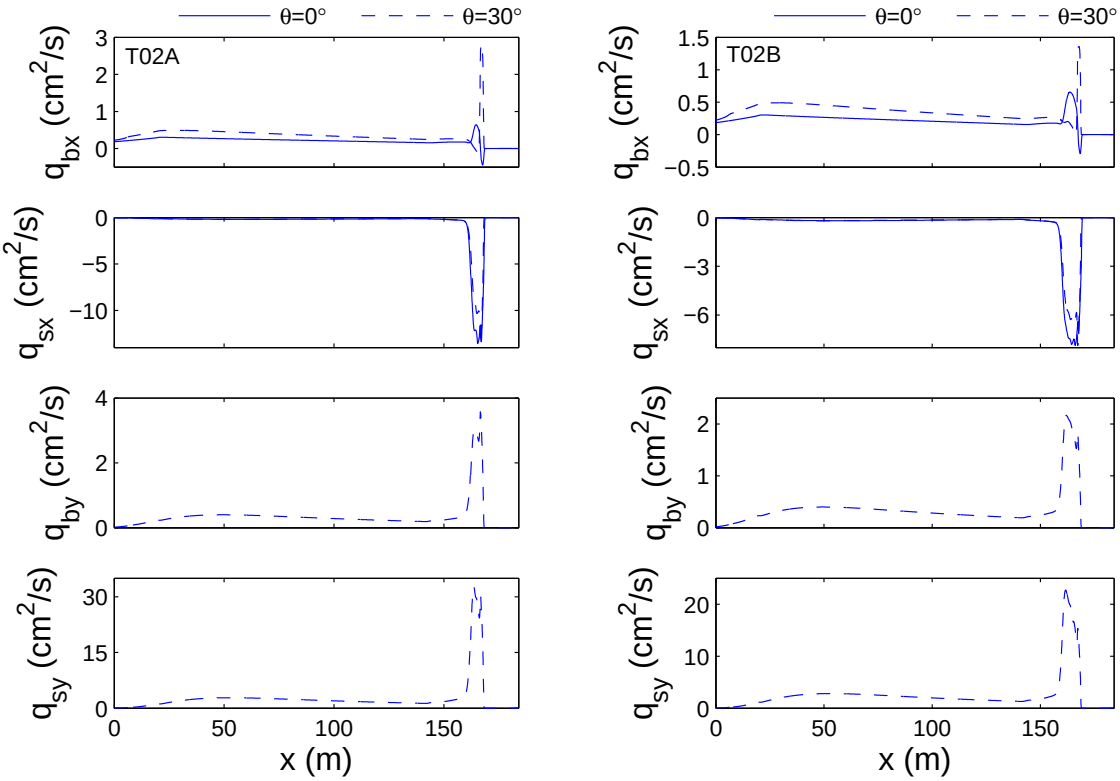

Figure C.15: Cross-shore variations of q_{bx}, q_{sx}, q_{by} and q_{sy} for $\theta = 0°$ and $\theta = 30°$ in tests T02A (left) and T02B (right).

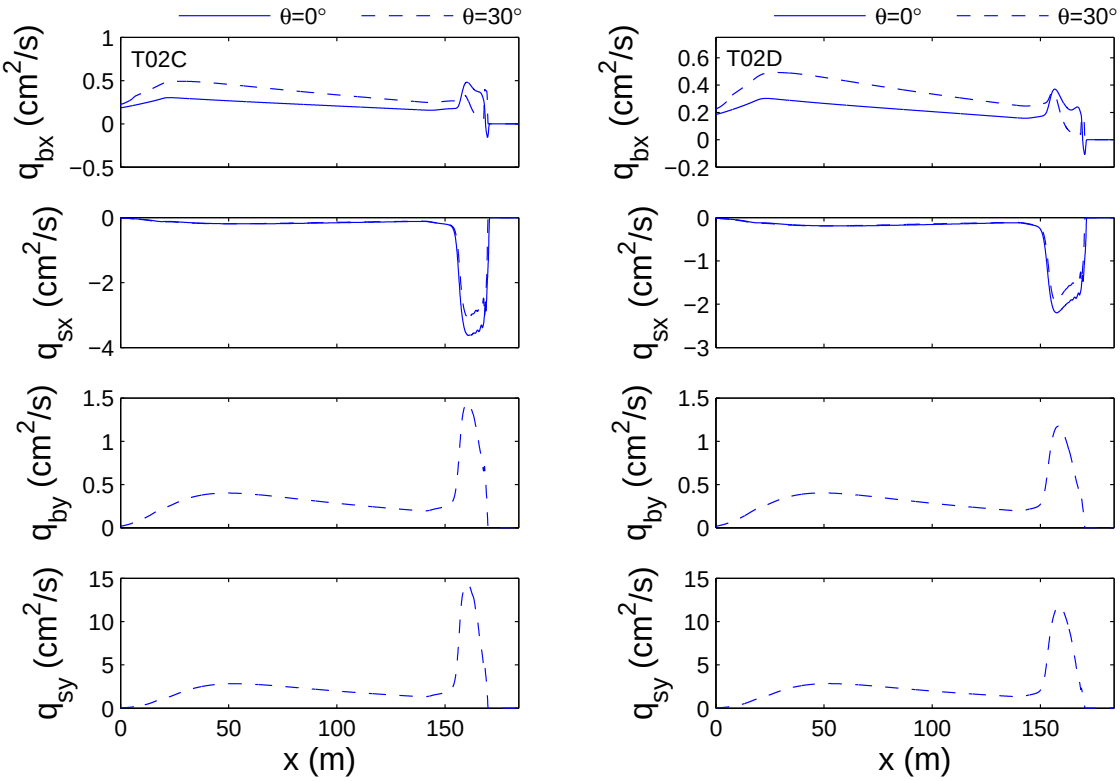

Figure C.16: Cross-shore variations of q_{bx}, q_{sx}, q_{by} and q_{sy} for $\theta = 0°$ and $\theta = 30°$ in tests T02C (left) and T02D (right).

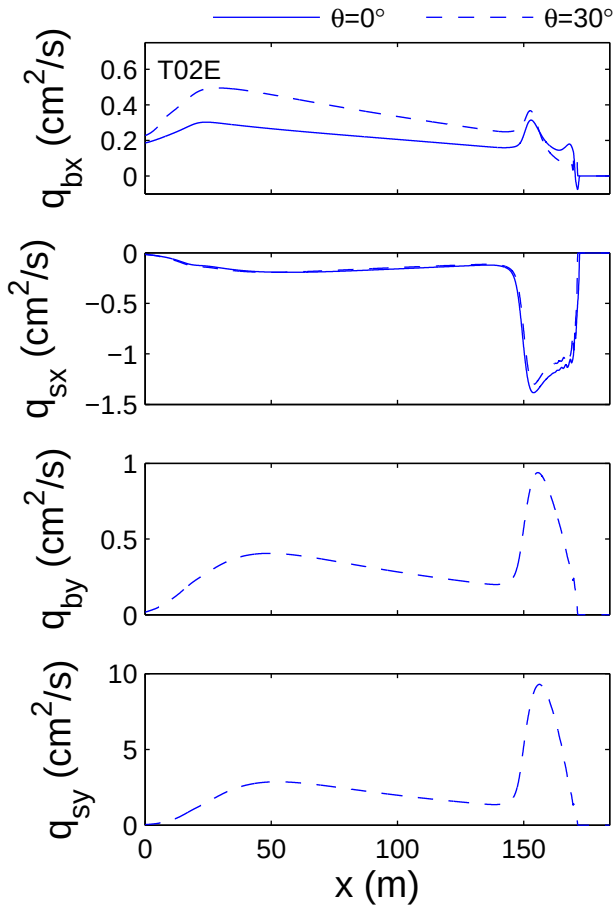

Figure C.17: Cross-shore variations of q_{bx}, q_{sx}, q_{by} and q_{sy} for $\theta = 0°$ and $\theta = 30°$ in tests T02E.

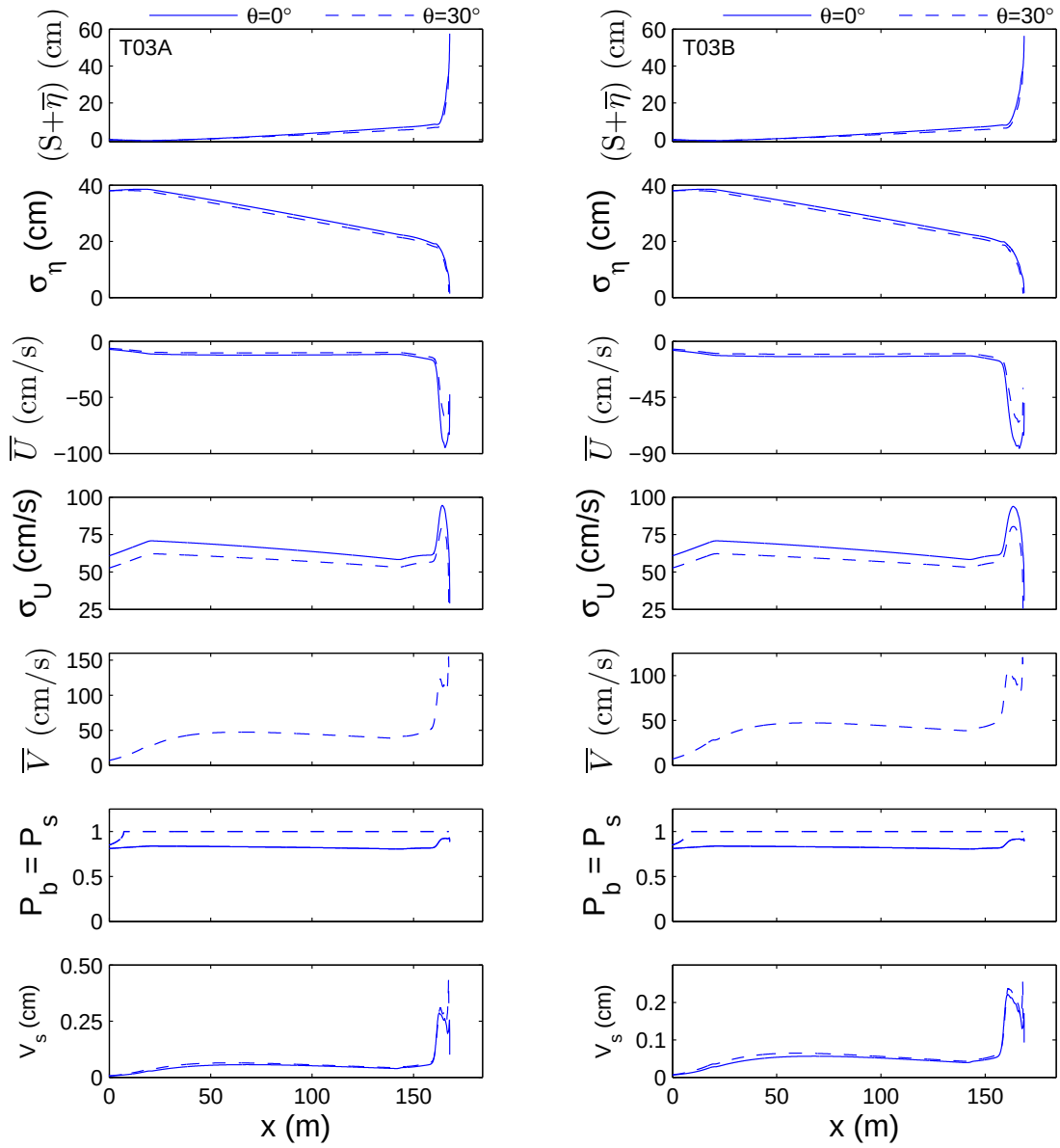

Figure C.18: Cross-shore variations of $(S + \bar{\eta})$, σ_η, $\bar{U}$, σ_U, $\bar{V}$, $P_b = P_s$ and V_s for $\theta = 0°$ and $\theta = 30°$ for tests T03A (left) and T03B (right)

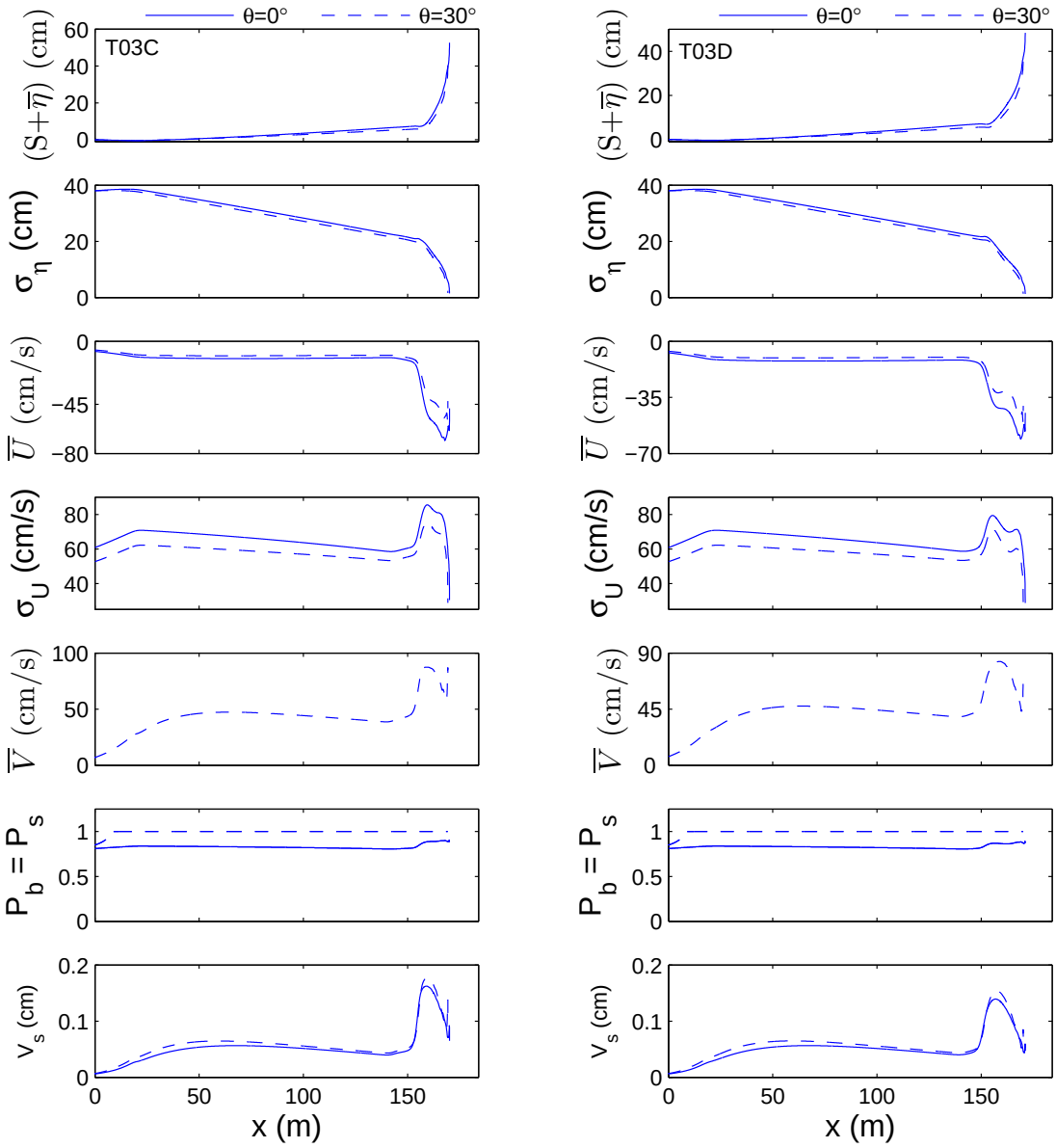

Figure C.19: Cross-shore variations of $(S + \bar{\eta})$, σ_η, $\bar{U}$, σ_U, $\bar{V}$, $P_b = P_s$ and V_s for $\theta = 0°$ and $\theta = 30°$ for tests T03C (left) and T03D (right)

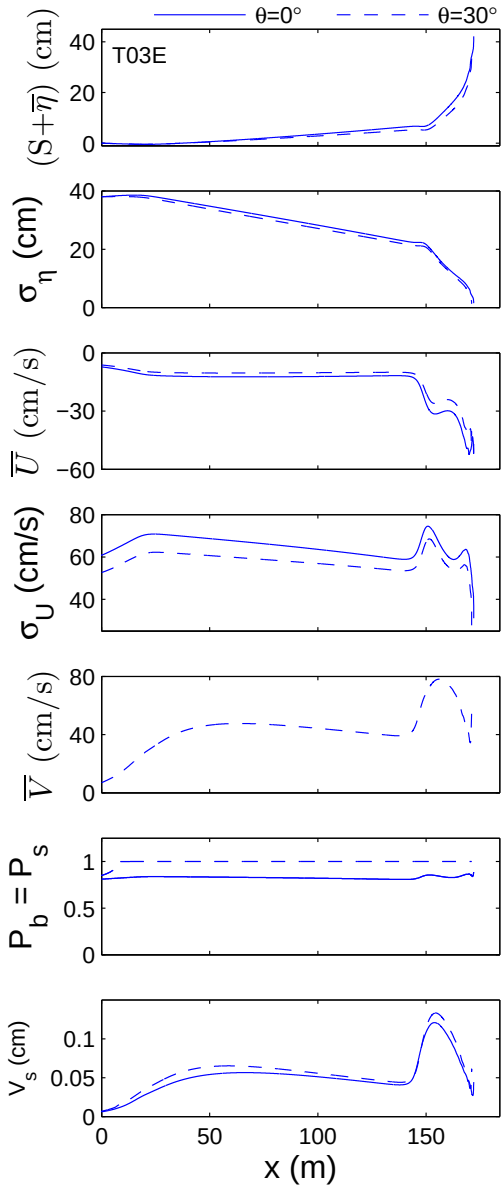

Figure C.20: Cross-shore variations of $(S + \bar{\eta})$, σ_η, $\bar{U}$, σ_U, $\bar{V}$, $P_b = P_s$ and V_s for $\theta = 0°$ and $\theta = 30°$ for test T03E

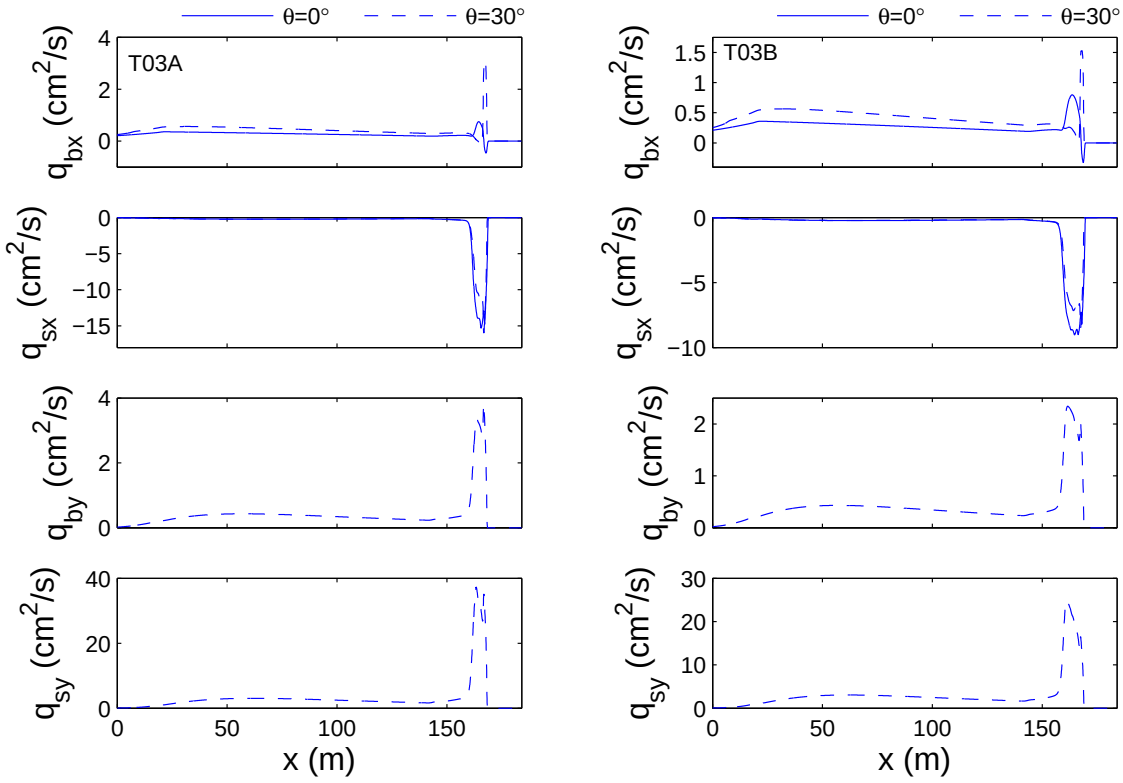

Figure C.21: Cross-shore variations of q_{bx}, q_{sx}, q_{by} and q_{sy} for $\theta = 0°$ and $\theta = 30°$ in tests T03A (left) and T03B (right).

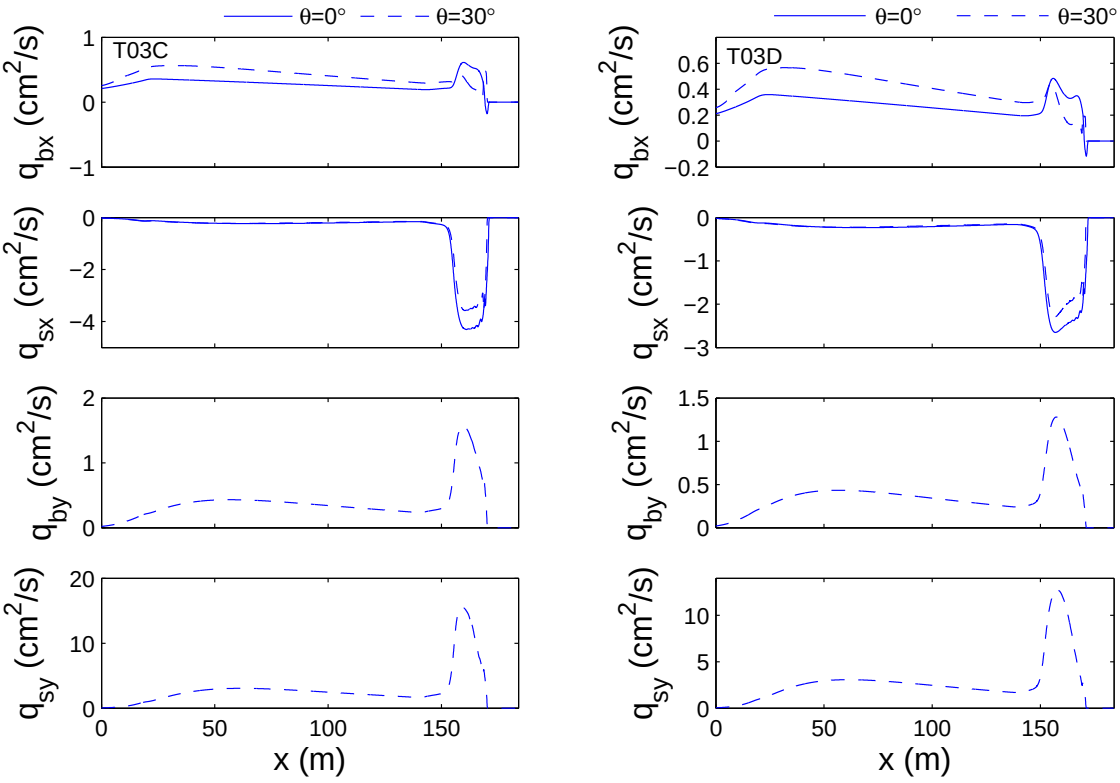

Figure C.22: Cross-shore variations of q_{bx}, q_{sx}, q_{by} and q_{sy} for $\theta = 0°$ and $\theta = 30°$ in tests T03C (left) and T03D (right).

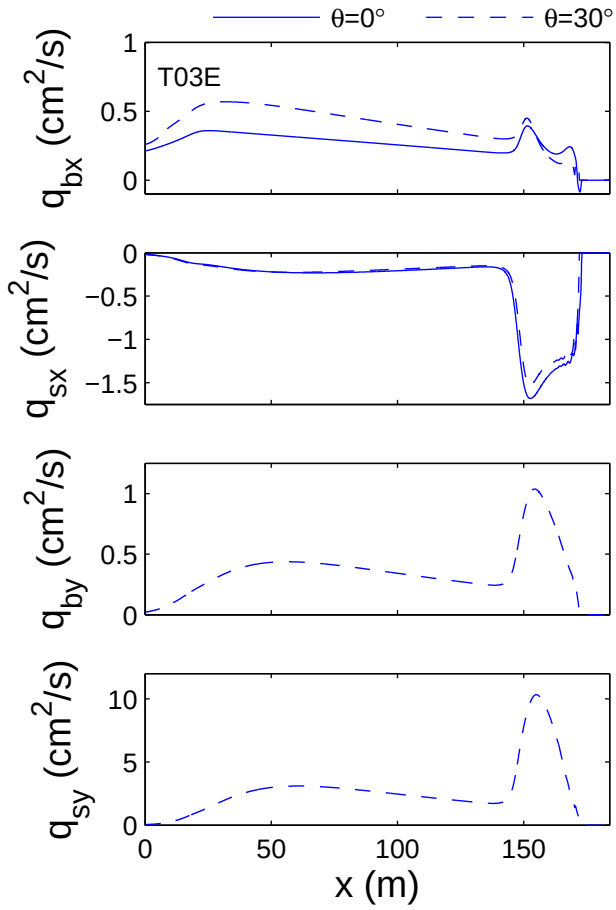

Figure C.23: Cross-shore variations of q_{bx}, q_{sx}, q_{by} and q_{sy} for $\theta = 0°$ and $\theta = 30°$ in test T03E.